Risque de subsidence et de contamination d'aquifère due à la dissolution des evaporites : modélisation d'écoulement et du transport du masse dans les milieux poreux et les milieux non-poreux

Ali Zidane

Angewandte und Umweltgeologie
Departement Umweltwissenschaften

École Doctorale Science de la Terre,
de l'Univers et de l'Environnement

THÈSE

Pour obtenir le grade de

DOCTEUR DE L'UNIVERSITE DE STRASBOURG

Zur Erlangung der Würde eines

DOKTORS DER PHILOSOPHIE DER UNIVERSITAT BASEL

Discipline: Mécanique des Fluides

Présenté par

Ali ZIDANE

Risk of subsidence and aquifer contamination due to evaporite dissolution: Modelization of flow and mass transport in porous and free flow domains

Soutenue le 13 Décembre 2012

Members of the jury

Supervisor (Basel)	:	M. P. HUGGENBERGER
Supervisor (Strasbourg)	:	M. A. YOUNES
Internal rapporteur	:	M. P. ACKERER
External rapporteur	:	M. G. KAUFFMAN
External rapporteur	:	M. B. AMAZIANE
Examiner	:	M. E. ZECHNER

Laboratoire d'Hydrologie et de Géochimie de Strasbourg

Qualifications of the Jury members:

- Prof. Dr. Peter HUGGENBERGER
  Head of the ‘‘Angewandte und Umweltgeologie, Dp. Umweltwissenschaften‘‘
  Basel, Switzerland

- Dr. Anis YOUNES
  ‘’Chargé de recherches au Laboratoire d’Hydrologie et de Géochimie de Strasbourg’’,
  Strasbourg, France

- Dr. Philippe ACKERER
  ‘’Directeur de recherches au Laboratoire d’Hydrologie et de Géochimie de Strasbourg’’
  Strasbourg, France

- Prof. Dr. Georg KAUFMANN
  Head of the research unit ‘’Arbeitsgruppe Dynamik der Erde, Fachrichtung Geophysik, Institut für geologische Wissenschaften‘‘
  Berlin, Germany

- Dr. Brahim AMAZIANE
  ‘’Maître de conférences HC au Laboratoire de Mathématiques et de leurs Application de Pau (LMAP)’’
  Pau, France

- Dr. Eric. ZECHNER
  Hydrogeologist, Research Associate ‘‘Angewandte und Umweltgeologie, Dp. Umweltwissenschaften‘‘
  Basel, Switzerland

Acknowledgements

The work presented in this thesis was carried out in the Applied and Environmental Geology Group (AUG), Institute of Geology and Paleontology, Department of Environmental Sciences of the University of Basel. And in part within the “Laboratoire d’Hydrologie et de Géochimie de Strasbourg (LHyGeS)”, in Strasbourg, France.

Many people have supported this project. First of all I wish to thank my supervisor in Basel Prof. Peter Huggenberger for providing this chance to me and for his support and encouragement during all this time. I also thank my supervisor in Strasbourg Prof. Anis Younes for the knowledge, the advice and the great support he has passed on and the freedom granted throughout my dissertation.

I am grateful to the jury members for their important critics, professors: Philippe Ackerer, *’’Directeur de recherches au LHyGeS’’*, Georg Kaufmann *’’Head of a research unit at Institut für geologische Wissenschaften Fachrichtung Geophysik Arbeitsgruppe Dynamik der Erde’’*, Brahim Amaziane *’’Maître de conférences au LMAP’’* and Eric Zechner “*Hydrogeologist Research Associate, Angewandte und Umweltgeologie, Dp. Umweltwissenschaften‘‘*

Lastly, I also wish to thank the members of the AUG and LHyGes for providing an enjoyable and productive atmosphere and for their great support. In particular I thank Jannis Epting, Stefan Scheidler, Rebecca Page, Stefan Wiesmeier, Silvia Leupin, Emanuel Huber, Eva Vojtech, and Horst Dresmann. In Strasbourg I thank Fanilo Ramasomanana, Noura Fajraoui, Salsabil Marzougi, Sana Ounaies and a very special thanks to Marwan Fahs.

Financial support for this project was provided by the Swiss National Science Foundation (SNSF).

Table of contents

Introduction

Purpose

The importance of groundwater for the existence of human society cannot be overemphasized. Indeed, groundwater is the major source of drinking water in both urban and rural areas. Understanding the different mechanisms and phenomena that occur within the groundwater level is essential for better management of a resource that has social and economic interests. On the other hand the complexity and the cost to access the underground environment make it difficult and sometimes impossible to study these mechanisms in-situ. Therefore, numerical modeling appears as a useful tool to reproduce some observed phenomena and to predict others in order to prevent as much as possible their negative effects on the environment.

A contribution to numerical methods has been made in this manuscript to simulate density driven flow problems in porous and free flow domains. The validity of the numerical codes was proven when compared against well-developed semi-analytical solutions for density driven flow in porous media and in free flow media. When validated, the numerical models are used to study the salt dissolution process. An adaptive mesh routine is developed and coupled to the density driven flow code in free flow media in order to study the salt dissolution process in a fracture. Finally, the density driven flow code in porous media is used to run a set of numerical simulations on a 2D cross section based on field measurements.

Regional subrosion

Groundwater circulation in evaporite bearing horizons and resulting dissolution (subrosion) of salt frequently causes geomechanical problems such as land subsidence or collapses. Moreover, the groundwater salt dissolution affects also the water quality, such as salinization and high mineralization. A significant potential hazard arises if radioactive waste repositories are situated in salt rock units. Salt deposits (e.g. rock salt), are largely widespread in a lot of continental regions. The subrosion process is considered as a major concern in construction projects and infrastructure planning (e.g. highways, railway connections). Moreover, the land subsidence phenomenon can be detected in areas with densely populated residential wich causes important infrastructural damages. The studied subrosion process studied in this thesis takes place in the region of Muttenz-Pratteln area (Figure 1). The subrosion process within the study area was also recorded in a 160 m of depth at the Adlertunnel, Basel, Switzerland which is part of a new European North-South railway connection The study areas are located in the east of the city of

Basel. These areas lie within the tectonic unit of the Tabular Jura, and they have been excessively used for subsurface operations (e.g. groundwater pumping, water withdrawal for drinking water supply, solution mining of halite). Further more, the studied areas are subdivided by a series of NNE-SSW Horst and Graben structures.

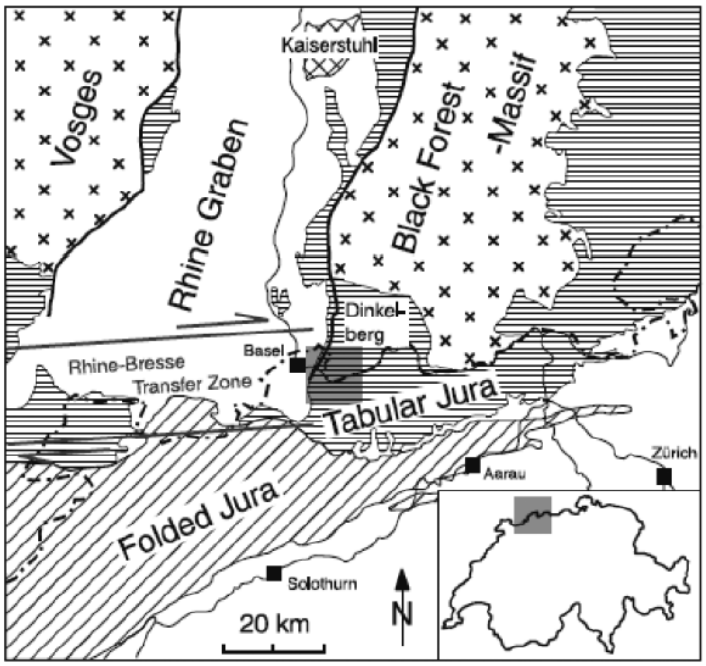

Figure 1: Regional overview with working area [Spottke et al., 2005]

The Horst and Graben structure of the Tabular Jura in the area of Muttenz-Pratteln and the Adlerhof-Anticline are explained in details in [Laubscher, 1982]. During an observation period of 78 days in 1997, land subsidence occurred in a section of the open-mined Adlertunnel at rates of 6 to 10 mm/month [Aegerter & Bosshardt, 1999].

Commonly the subrosion phenomenon is due to the extensive use of natural resources (e.g. groundwater withdrawal for drinking water, solution mining of halite). Large scale groundwater extraction and recharge may significantly increase the hydraulic gradients on large parts of the aquifer which in turn would accelerate the karst evolution.

The first investigations on the relationship between solution mining and land subsidence were made by [Trefzger 1925, 1950]. He compared subsidence and salt production rates for different exploration wells in the Rheinfelden solution-mining district. And later the study continued with [Hauber 1971] and recently with [Zechner et al. 2011].

General overview

In order to develop and to validate the numerical codes required to simulate dissolution and density driven transport, the thesis starts with the developed and the adopted mathematical and numerical models (chapters 1-2).

In this work, we focus on the development of numerical models to simulate density flow in porous and free flow free domains. The dissolution phenomenon and evolution of fractures over time has been studied in this thesis as well. The developed models take into account the physical processes (advection, dispersion, molecular diffusion) and chemical processes (dissolution) using the equations of conservation of mass (PDEs) and the equation of dissolution. Efficient numerical methods are used to solve these equations. The mixed finite element method (MFE) is used to solve the flow in porous media and the nonconforming finite element method Crouzeix-Raviart (CR) is used to solve the flow within fractures (non-porous media). The mass transport equation is solved using the Multi-Point Flux Approximation method (MPFA) for the dispersion part and the Discontinuous Galerkin method (DG) for the advection part. The simulation of the fractures evolution is based on the development of a dynamic mesh method that adapts depending on the amount of dissolved salt at the boundaries. The dissolution model is combined with the flow-transport models in order to simulate density driven flow with fracture evolution.

In order to reach this goal, we needed first to validate the developed numerical codes. The first part of the thesis addresses the validation of the numerical model to simulate density driven flow in porous media. The simplified problem of saltwater intrusion in a coastal aquifer, known as the Henry problem [Henry 1964], is widely used for the validation of numerical models. In fact, this problem has a semi-analytical solution that was developed by Henry [Henry 1964] and corrected by Ségol [1994]. However, this solution can only simulate saltwater intrusion with unrealistic large amount of dispersion. The procedure developed by Henry is based on two steps: (i) an approximation of the solution by using a Fourier series representation with a certain truncation order of the coefficients and (ii) resolution of a strongly non-linear algebraic system to calculate these coefficients. Since 1964 all the authors (Henry [1964] Ségol [1994], Simpson and Clement [2004]) who worked on the Henry problem used the same iterative technique for solving the obtained algebraic system. This iterative technique is based on a sequential resolution of nonlinear systems of flow and mass transport. With this technique, convergence problems are encountered when decreasing the value of molecular diffusion. In addition, the number of Fourier

coefficients needed to calculate (and therefore the size of the nonlinear system to solve) increases significantly when the diffusion decreases. To overcome these difficulties, a new procedure for calculating the semi-analytical solution of the Henry problem is developed in this thesis. This procedure consists of solving simultaneously the two systems of flow and transport by using the Levenberg-Marquardt algorithm [Levenberg 1944, Marquardt 1963]. The use of this technique allowed to develop, for the first time, semi-analytical solutions of saltwater intrusion in the case of small diffusion and in the case of a large density contrast. These semi-analytical solutions were compared to the numerical solutions and are therefore suited for density driven model validation (chapter 3).

In the second part of this work, we studied the flow in fractured evaporitic rocks. The Stokes equation that governs the flow is coupled to the advection dispersion equation via the state equation relating the variation of the density to mass fraction. A numerical code was developed to solve the nonlinear system using advanced numerical methods (MPFA-CR-DG). In order to validate this new model a semi-analytical solution for a density Stokes flow is developed in this thesis. This solution uses the same technique used for the Henry problem. Substituting Darcy's equation by the Stokes equation in the Fourier-Galerkin method, we built a new nonlinear algebraic system of equations. This system is more difficult to solve than the previous one because of the high magnitude of the free flow velocities. Again, the Levenberg-Marquardt algorithm is used to calculate the coefficients of the Fourier series of the semi-analytical solution. This new semi-analytical solution could then be used to validate density driven flow for free fluids (chapter 4).

The final part of this work is devoted to the transport problem with dissolution of rock salt.

In a first step of the dissolution study, we are interested in simulating salt dissolution within fractures. The numerical model takes into account the density driven Stokes flow and the dissolution of the fracture walls. A dynamic mesh algorithm is developed to track the evolution of these walls over the time. A consistent dissolution profile is obtained when comparing the numerical results with the experimental results for a simple fracture with reactive dissolution walls (chapter 5).

Finally, and going to field scale, several observations and studies have been conducted on the salt dissolution study and the rate of subsidence [Aegerter & Bosshardt, 1999, Laubscher, 1982 Spottke et al. 2005, Zechner et al. 2011]. The starting point was the results of Zechner et al.

[2011] on a 2D cross section within the Muttenz-Pratteln area. These authors revealed that the dissolution rate is very sensitive to the structure or dip of the halite formation. Therefore, more concern was given in this thesis to the structure and tectonics of the aquifers and the fault zones among other parameters to study their influence on the salt dissolution process and therefore on the subsidence phenomenon. The boundary conditions used in these simulations are estimated based on field measurements. The effect of several parameters was studied. The study showed, however, that some parameters (well depth, hydraulic charge at the inlet of the aquifer) have negligible effects on the dissolution. Other parameters (permeability, thickness of the lower aquifer, fault geometry) have a considerable effect on the dissolution process (chapter 6).

Chapter 1

Mathematical models for density driven flow in porous and free flow domains

Contents

1.1 The mathematical flow model

1.1.1 The flow model in Porous media

Definition

A porous medium is a solid containing void spaces (pores), connected or unconnected, dispersed within it in either a regular or random manner. These so called pores may contain a variety of fluids such as air, water, oil etc. If the pores represent a certain portion of the bulk volume, a complex network can be formed which is able to carry fluids. Only these permeable and porous media are taken into consideration in this volume.

Porosity

The porosity ε [-] of a material is determined by measuring the amount of void space inside, and determining what percentage of the total volume of the material is made up of void space. Porosity measurements can vary considerably, depending on the material. High or low porosity will impact the way in which the material performs. For a material with a total volume V_t the porosity ε is given by:

$$\varepsilon = \frac{V_p}{V_t} = \frac{V_t - V_s}{V_t} \tag{1.1}$$

where

V_p is the void volume (pore volume) and

V_s is the volume of the solid material.

Permeability and intrinsic permeability

The intrinsic permeability k [L^2] is the pertaining to the relative ease with which a porous medium can transmit a liquid under a hydraulic or potential gradient. It is a property of the porous medium and is independent of the nature of the liquid or the potential field.

The permeability K [$L.T^{-1}$] is the rate at which liquids pass through a porous medium in a specified direction. It is therefore the capacity for transmitting a fluid, measured by the rate at which a fluid of standard viscosity can move a given distance through a given interval of time. The permeability is a function of the intrinsic permeability k, the dynamic viscosity μ [$M.L^{-1}.T^{-1}$] and the density of the circulating fluid ρ [$M.L^{-3}$]. The permeability K and the

intrinsic permeability k are scalar coefficients if the porous medium is isotropic, or if the flow occurs only in one direction. Otherwise, the hydraulic conductivity matrix is given as follows:

$$\boldsymbol{K} = \begin{bmatrix} K_{xx} & K_{xy} & K_{xz} \\ K_{yx} & K_{yy} & K_{yz} \\ K_{zx} & K_{zy} & K_{zz} \end{bmatrix} \tag{1.2}$$

with $K_{ij} = \dfrac{k_{ij}\rho g}{\mu}$, where g [L.T^{-2}] is the gravity acceleration.

Governing equations

The flow equation in a saturated porous media is described by a system of equations based on Darcy's law and the mass conservation equation or the continuity equation. In porous media, Darcy's law is considered as the analogous of the momentum conservation equation of the classic fluid dynamics.

Darcy's law

In 1856, Darcy established empirically that the flux of water Q [L^3.T^{-1}] through a permeable formation with a section A [L^2] and conductivity K [L.T^{-1}] is proportional to the charge difference $\Delta H = H_1 - H_2$ [L], and is inversely proportional to the distance L [L] separating two points of charge $H_1 and\ H_2$. Darcy's law could be then written in the following form:

$$\frac{Q}{A} = K\frac{H_1 - H_2}{L} \tag{1.3}$$

Following [Bear 1979], the filtration velocity or Darcy's velocity could be written in terms of pressure gradient and gravity acceleration as follows:

$$\boldsymbol{q} = -\frac{\boldsymbol{k}}{\mu}\left(\nabla p + \rho g \nabla z\right) \tag{1.4}$$

where

$\boldsymbol{q}$: Darcy's velocity [L.T^{-1}];

$\boldsymbol{k}$: The intrinsic permeability tensor of the medium [L^2];

p : The pressure [M.L^{-1}.T^{-2}];

z : The depth [L].

The fluid velocity $\boldsymbol{V}$ [L.T^{-1}] could be deduced from the Darcy's velocity using the following equation:

$$\boldsymbol{V} = \frac{\boldsymbol{q}}{\varepsilon} \tag{1.5}$$

The equivalent freshwater head h [L] is given in the following form:

$$h = \frac{p}{\rho_0 g} + z \tag{1.6}$$

Using (1.6) and (1.4) the Darcy's equation could be written in function of the freshwater head as follows:

$$\boldsymbol{q} = -\boldsymbol{K}\left(\nabla h + \frac{\rho - \rho_0}{\rho_0}\nabla z\right) \tag{1.7}$$

where $\boldsymbol{K}$ [L.T^{-1}] is the hydraulic conductivity tensor, and ρ_0 [M.L^{-3}] is the freshwater density.

If the density is considered as constant, equation (1.7) reduces to:

$$\boldsymbol{q} = -\boldsymbol{K}\nabla h \tag{1.8}$$

Continuity equation

The continuity equation or the mass balance equation shows the principle of mass conservation of the fluid. In a finite elementary volume (FEV), the amount of injected (or displaced) fluid should be equal to the sum of the mass variation within an interval of time and the mass flux passing through the volume. This could be given by the following equation [Bear 1979]:

$$\frac{\partial(\varepsilon\rho)}{\partial t} + \nabla.(\rho\boldsymbol{q}) = \rho_{ps} f_{ps} \tag{1.9}$$

Assuming that the porosity is a function of the pressure, and the density is a function of the pressure and the solute mass fraction (at a constant temperature), the first term in equation (1.9) could be written in the following form:

$$\frac{\partial(\varepsilon\rho)}{\partial t} = \rho\frac{\partial\varepsilon}{\partial t} + \varepsilon\frac{\partial\rho}{\partial t} = \left(\rho\frac{\partial\varepsilon}{\partial p} + \varepsilon\frac{\partial\rho}{\partial p}\right)\frac{\partial p}{\partial t} + \varepsilon\frac{\partial\rho}{\partial C}\frac{\partial C}{\partial t} \tag{1.10}$$

Using the definitions of the porous matrix compressibility coefficient τ and the fluid compressibility coefficient β as given by Bear [Bear 1979]:

$$\tau = \frac{1}{1-\varepsilon}\frac{\partial\varepsilon}{\partial p}, \quad \beta = \frac{1}{\rho}\frac{\partial\rho}{\partial p} \tag{1.11}$$

Equation (1.10) becomes:

$$\frac{\partial(\varepsilon\rho)}{\partial t} = \rho S \frac{\partial p}{\partial t} + \varepsilon \frac{\partial \rho}{\partial C}\frac{\partial C}{\partial t} \tag{1.12}$$

with

f_{ps} [$L^3.T^{-1}$] is the sink/source term;

ρ_{ps} [$M.L^{-3}$] is the sink/source density;

C [Mass solute/Mass fluid] is the solute mass fraction;

S [$M^{-1}.L.T^2$] is the specific pressure storativity for a rigid solid matrix and it's given as follows:

$$S = \tau(1-\varepsilon) + \varepsilon\beta \tag{1.13}$$

The continuity equation (1.9) could be then written in the following form:

$$\rho S \frac{\partial p}{\partial t} + \varepsilon \frac{\partial \rho}{\partial C}\frac{\partial C}{\partial t} + \nabla.(\rho \boldsymbol{q}) = \rho_{ps} f_{ps} \tag{1.14}$$

Approximations

Referring to [Ackerer and Younes 2008], two approximations could be used with the mass balance equation.

- The Oberbeck–Boussinesq approximation: where density variations are neglected in the fluid mass balance:

$$\frac{\partial \varepsilon}{\partial t} + \nabla.\boldsymbol{q} = f_{ps} \tag{1.15}$$

- The density variation in the fluid flow direction is neglected, and the fluid mass conservation equation (1.9) becomes:

$$\frac{\partial(\varepsilon\rho)}{\partial t} + \rho\nabla.\boldsymbol{q} = \rho_{ps} f_{ps} \tag{1.16}$$

As stated by [Kolditz et al 1998, Johannsen et al 2002, Ackerer and Younes 2008] Boussinesq assumption may introduce errors and should be avoided. The assumption stated by Bear [Bear 1979] consists in neglecting $\nabla\rho.\boldsymbol{q}$, which represents the density variations in the flow direction. This approximation has been found efficient without particular loss of accuracy. Hence, the continuity equation could be written in the following form:

$$\rho S \frac{\partial p}{\partial t} + \varepsilon \frac{\partial \rho}{\partial C}\frac{\partial C}{\partial t} + \rho\nabla.\boldsymbol{q} = \rho_{ps} f_{ps} \tag{1.17}$$

Using (1.6) we get:

$$\rho S_s \frac{\partial h}{\partial t} + \varepsilon \frac{\partial \rho}{\partial C}\frac{\partial C}{\partial t} + \rho \nabla . \boldsymbol{q} = \rho_{ps} f_{ps} \tag{1.18}$$

where $S_s = \rho g S$ is the specific mass storativity related to head changes [L^{-1}].

Boundary conditions

Three main types of boundary conditions are used when studying the fluid flow in porous media, and they are stated as follows:

Dirichlet conditions

In this case the hydraulic charge is imposed at one or different sides of the domain.

$$h(x,t) = h^D(x,t) \tag{1.19}$$

where $h^D(x,t)$ is a known function.

Neumann conditions

This type of boundary conditions consists of imposing a normal flux on one or different sides of the domain.

$$\boldsymbol{q}.\boldsymbol{\eta} = -\boldsymbol{K}\frac{\partial h}{\partial \boldsymbol{\eta}} = q^N(x,t) \tag{1.20}$$

where $\boldsymbol{\eta}$ is the unit normal vector, and $q^N(x,t)$ is a known flux value.

Cauchy or Fourier conditions

These are mixed conditions of charge and flow. In certain cases, the flux is described as a function of the charge, as follows:

$$\boldsymbol{q}.\boldsymbol{\eta} = -\boldsymbol{K}\frac{\partial h}{\partial \boldsymbol{\eta}} = g^F(x,t)h + f^F(x,t) \tag{1.21}$$

where $g^F(x,t)$ and $f^F(x,t)$ are known quantities.

1.1.2 The free flow model

Definition

Fluid flow through channels, cavities and fractures are referred to free fluid or free flow. Single-phase steady incompressible flow through a free flow media is governed by the Navier-Stokes equation:

$$\rho(\boldsymbol{u}.\nabla)\boldsymbol{u} + \nabla p - \mu\nabla^2\boldsymbol{u} = \rho\boldsymbol{g} \tag{1.22}$$

and the continuity equation:

$$\nabla.\boldsymbol{u} = 0 \tag{1.23}$$

where $\boldsymbol{u}$ [$L.T^{-1}$] is the velocity vector, and μ [$M.L^{-1}.T^{-1}$] is the dynamic viscosity.

Governing equations

In the treated cases within this thesis, we assume that the flow is sufficiently slow to consider the inertial forces in the flow field (the first nonlinear term in equation (1.22)) negligibly small compared with the viscous and pressure forces. Therefore, in this case, the free-flow is governed by the following Stokes equations [Happel and Brenner 1965]:

$$\nabla p - \mu\nabla^2\boldsymbol{u} = \rho\boldsymbol{g} \tag{1.24}$$

$$\nabla.\boldsymbol{u} = 0 \tag{1.25}$$

Boundary conditions

Referring to [Gresho and Sani 1987, Conca et al. 1994, 1995, Jäger and Mikelić 2001] three types of boundary conditions are used in Stokes flow:

Imposed velocity

In this type, the vertical and/or the horizontal velocities are imposed at one or different sides of the domain.

$$\boldsymbol{u}=\boldsymbol{u}^{imp} \tag{1.26}$$

where $\boldsymbol{u}^{imp}$ is a known velocity vector.

Free boundary

Known as free outflow boundary condition, and is given by the following equation:

$$\mu(\nabla\boldsymbol{u})\boldsymbol{\eta} - p\boldsymbol{\eta} = 0 \tag{1.27}$$

Imposed pressure

The pressure p is prescribed at the boundary. Note that in this case, we set also the velocity components in the tangential direction to zero on the same boundary. This condition is named Normal flow/Pressure or straight-out boundary condition.

$$p = p^{imp}$$
$$\boldsymbol{u}.\boldsymbol{\eta}_t = 0 \tag{1.28}$$

where $\boldsymbol{\eta}_t$ is the unit tangential vector along the side where the pressure is imposed.

1.2 The transport model

Definition

When water flows, it could transport different kinds of species or solutes, in a dissolute form. At this end, different physical and chemical phenomena could occur in the transport process of these solutes. The physical mechanisms within the transport are the advection, the molecular diffusion and the kinematic dispersion. For the moment, we consider that there's no reaction in the transport process, and therefore we show at first the transport equation with no chemical reactions.

Governing equations

Advection

The advection (or convection) corresponds to the migration of solutes during displacement of water. This is the phenomenon by which the contaminant moves with the movement of the water which could be governed by Darcy or Stokes law. The average displacement of the contaminant by advection is directly proportional to the average flow velocity of the water. When the solute does not react with the environment, the transfer rate of the solute is that of the fluid that moves. The advection is described by the following hyperbolic equation:

$$\frac{\partial(\varepsilon C)}{\partial t} + \nabla.(\boldsymbol{q}C) = 0 \tag{1.29}$$

where

C [ML^{-3}] is the solute concentration;

$\boldsymbol{q}$ [$L.T^{-1}$] is the Darcy's velocity.

In the case of free flows, the Darcy's velocity is simply replaced by $\boldsymbol{u}$, and the porosity ε by one. This is also applicable for the rest of the transport equations within this section.

Molecular diffusion

The molecular diffusion is a phenomenon which is independent of the velocity of the fluid as it occurs even in the absence of flow (velocity). It is related to the existence of a concentration

gradient in the fluid and is derived from the agitation of the molecules that tends to homogenize the solute concentration within the medium (migration of molecules from high concentration areas to those with low concentrations). The solute mass flow transported by molecular diffusion is calculated according to Fick's law:

$$\frac{\partial(\varepsilon C)}{\partial t} - \nabla.(\boldsymbol{D_m}\nabla C) = 0 \tag{1.30}$$

where $\boldsymbol{D_m}$ [$L^2.T^{-1}$] is the molecular diffusion diagonal tensor.

Dispersion

Dispersion is the transport phenomenon resulting from the combined action of these two processes: Kinematic dispersion and molecular diffusion. The dispersion-diffusion transport approaches a parabolic equation type and is given by:

$$\frac{\partial(\varepsilon C)}{\partial t} - \nabla.(\boldsymbol{D}\nabla C) = 0 \tag{1.31}$$

where

$\boldsymbol{D} = \boldsymbol{D}_k + \boldsymbol{D_m}$ is the dispersion tensor, given as follows :

$$D_{M,ij} = (D_L - D_T)\frac{q_i q_j}{|\boldsymbol{q}|^2} + D_T\delta_{ij} \tag{1.32}$$

with

$\boldsymbol{D}_k$ is the kinematic dispersion tensor;

D_L the longitudinal dispersion coefficient, $D_L = \alpha_L|\boldsymbol{q}|, with|\boldsymbol{q}| = \left(q_i^2 + q_j^2\right)^{0.5}$;

D_T the transverse dispersion coefficient, $D_T = \alpha_T|\boldsymbol{q}|$;

α_L the longitudinal dispersivity in the direction of flow;

α_T the transverse dispersivity normal to the direction of flow;

δ_{ij} the Kronecker delta.

Advection-dispersion equation

The mathematical model that describes the transport of a solute with no interaction with the solid matrix is given by the advection-dispersion equation as follows:

$$\frac{\partial(\varepsilon\rho C)}{\partial t} + \nabla.(\rho\boldsymbol{q}C) - \nabla.(\rho\boldsymbol{D}\nabla C) = 0 \tag{1.33}$$

For free flows, the transport equation becomes:

$$\frac{\partial(\rho C)}{\partial t} + \nabla.(\rho \boldsymbol{u} C) - \nabla.(\rho D \nabla C) = 0 \tag{1.34}$$

where $\boldsymbol{u}$ is the flow velocity, and D is the diffusion coefficient.

Boundary conditions

The associated boundary conditions could be:

- Dirichlet type (imposed concentration);
- Neumann type (imposed concentration gradient);
- Cauchy type (flux related to concentration).

1.3 Dissolution

In case of dissolution, the transport equation is written in the following form:

$$\frac{\partial(\varepsilon \rho C)}{\partial t} + \nabla.(\rho \boldsymbol{q} C) - \nabla.(\rho \boldsymbol{D} \nabla C) = Q_s \tag{1.35}$$

For free flows, the transport equation becomes:

$$\frac{\partial(\rho C)}{\partial t} + \nabla.(\rho \boldsymbol{u} C) - \nabla.(\rho D \nabla C) = Q_s \tag{1.36}$$

where Q_s is the dissolution flux, given as follows:

$$Q_s = \lambda(C_{sat} - C) \tag{1.37}$$

where λ [mol.L^{-2}.T^{-1}] is the mass transfer coefficient, and C_{sat} is the saturation concentration.

1.4 Coupling flow and transport models

Flow and transport equations are coupled by state equations linking density and viscosity to mass fraction. We use a linear model for density and a power formulation for viscosity:

$$\rho = \rho_0 + (\rho_1 - \rho_0)C, \text{ and } \mu = \mu_0 \left(\frac{\mu_1}{\mu_0} \right)^C \tag{1.38}$$

where ρ_1 and μ_1 are respectively the density and viscosity of the saturated (high density) fluid, ρ_0 and μ_0 are the density and viscosity of the displaced (less dense) fluid. Note that different state equations may be used for density and viscosity [Dierch and Kolditz 2002].

The following diagram shows the coupling between the transport and the flow equations:

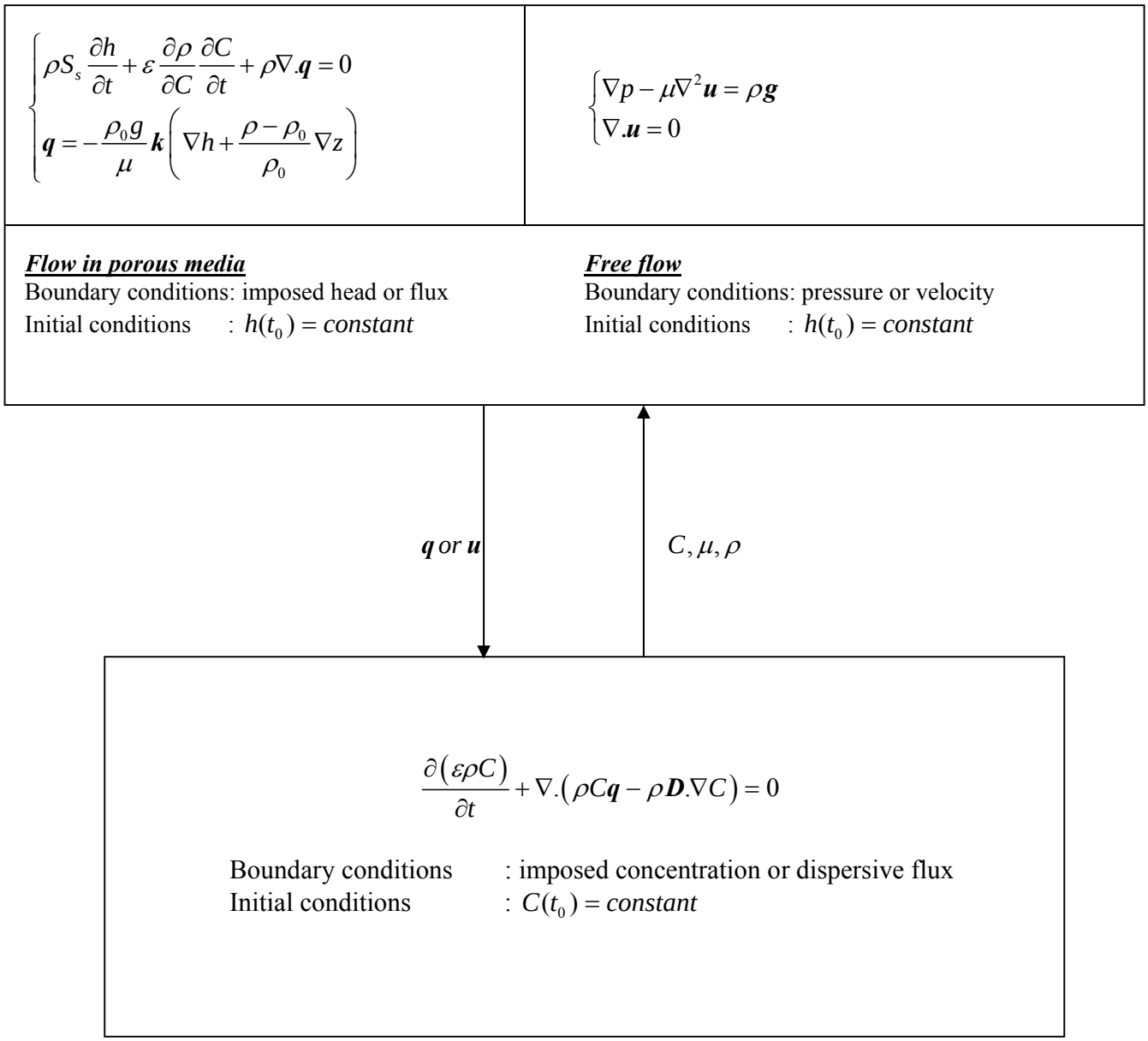

Chapter 2

Numerical models for density driven flow in porous and free flow domains

Contents

2.1 Flow discretization

2.1.1 Flow in porous media

Introduction

Different methods are used to solve the flow problem. Among them we cite the most used which are: Finite Volumes (FV), Finite Differences (FD) and Finite Elements (FE). Detailed studies on the application of conventional techniques for solving problems of hydrogeology are presented by Remson et al. [1971] and Wang and Anderson [1982]. Each of these methods has its own advantages and disadvantages. Since the flow equation should be coupled with the transport equation (See Chapters 3, 4) the numerical flow model should provide accurate velocity field with continuous fluxes between adjacent elements even for highly heterogeneous domains with unstructured meshes.

The FD and FV Methods allow the calculation of an average head per element. They give an exact mass balance at each element. The discretization of the flow equation with FDs is easy to develop but it can only be applied on rectangular (2D) or cubic (3D) meshes. Similarly, the FV method on triangular meshes requires triangles satisfying the Delaunay criterion (no point of a triangle is inside the circumcircle of any other triangle of the domain). This criterion cannot be easily applied on tetrahedrons. In addition, FV and FD approaches are not suitable for solving problems where the hydraulic conductivity $\boldsymbol{K}$ is represented by a full discontinuous tensor.

Unlike FD and FV, the FE method allows the discretization of domains with complex geometry and full parameter tensor. However, continuity of the normal component of the velocity between adjacent elements in not guaranteed with the standard FE method. To overcome these difficulties, we use the mixed finite element method for the discretization of flow in porous media.

The mixed finite element method

The basic idea of the mixed finite element method is to approach simultaneously the hydraulic head H and the flow velocity $\boldsymbol{q}$. This approach has been used for the first time by Meissner [1973], and later by Raviart and Thomass [1977]. The MFE method provides exact mass balance for each element and preserves the same order of convergence for the hydraulic head H and the flow velocity $\boldsymbol{q}$. On the other side, it's a well-adapted method for heterogeneous domains, discretized with irregular meshes. In the following, we recall the main stages for the discretization of the flow equation using the MFE method.

The mixed finite element approach consists in writing the mass balance equation and Darcy's law separately in a variational form but with different basis functions. The mass balance equation in (1.18) is discretized in a finite volume way and a fully implicit scheme which leads to [Ackerer and Younes 2008, Younes et al. 2009]:

$$S_s |E| \frac{h^{n+1} - h^n}{\Delta t} + \sum_i Q_i^{n+1} = |E| \frac{\rho_{ps}}{\rho} f_{ps} - \varepsilon |E| \frac{1}{\rho} \frac{\partial \rho}{\partial C} \frac{\partial C}{\partial t} \tag{2.1}$$

where $|E|$ is the area of element *E*. With MFEs, the velocity inside each triangle E is approximated with linear vectorial basis functions:

$$\boldsymbol{q} = \sum_{j=1}^{3} Q_j^E \boldsymbol{w}_j^E \tag{2.2}$$

where Q_j^E is the flux across the edge j of the element E and $\boldsymbol{w}_j^E$ are the Raviart-Thomas basis functions given by

$$\boldsymbol{w}_j^E = \frac{1}{2|E|} \begin{pmatrix} x - x_{E,i} \\ z - z_{E,i} \end{pmatrix} \tag{2.3}$$

and verify

$$\int_{E_j} \boldsymbol{w}_i \cdot \boldsymbol{n}_j = \begin{cases} 1 & if \quad i = j \\ 0 & if \quad j \neq i \end{cases} \tag{2.4}$$

where $x_{E,i}$ and $z_{E,i}$ are the coordinates of the vertex *i* of E (opposed to the edge *i*), $\boldsymbol{n}_j$ is the unit normal outwardly oriented vector and E_j the edge j of E.

Darcy's law (1.7) could be written in the following form:

$$\boldsymbol{k}^{-1} \boldsymbol{q} = -\frac{\rho_0 g}{\mu} \left(\nabla h + \frac{(\rho - \rho_0)}{\rho_0} \nabla z \right) \tag{2.5}$$

where $\boldsymbol{k}$ is the matrix of the intrinsic permeabilities with $\det(\boldsymbol{k}) = k_x k_z - \left(k_{xz}\right)^2 > 0$.

Equation (2.5) is written in a variational form which leads to:

$$\begin{aligned} \int_E (\boldsymbol{k}^{-1} \boldsymbol{q}) . \boldsymbol{w}_i &= -\rho_0 g \int_E \frac{1}{\mu} \nabla h . \boldsymbol{w}_i - \rho_0 g \int_E \frac{\rho - \rho_0}{\rho_0 \mu} \nabla z . \boldsymbol{w}_i \\ &\approx -\frac{\rho_0 g}{\mu_E} \int_E \nabla h . \boldsymbol{w}_i - g \frac{\rho_E - \rho_0}{\mu_E} \int_E \nabla z . \boldsymbol{w}_i \end{aligned} \tag{2.6}$$

Using Green's formula and (2.4), we obtain,

$$\begin{aligned}\int_E (\boldsymbol{k}^{-1}\boldsymbol{q}\ ).\boldsymbol{w}_i &= \frac{\rho_0 g}{\mu_E}\left(\int_E h\nabla \boldsymbol{w}_i - \int_{\partial E} h\boldsymbol{w}_i.\boldsymbol{n}_{\partial E}\right) + g\frac{\rho_E-\rho_0}{\mu_E}\left(\int_E z\nabla \boldsymbol{w}_i - \int_{\partial E} z\boldsymbol{w}_i.\boldsymbol{n}_{\partial E}\right)\\ &= \frac{\rho_0 g}{\mu_E}\left(h_E - Th_{Ei}\right) + g\frac{\rho_E-\rho_0}{\mu_E}\left(z_E - z_{Ei}\right)\end{aligned} \tag{2.7}$$

where h_E is the average head in element *E*, z_E the z-coordinate of the centre of *E* , Th_{Ei} the average head on edge *i* of element *E*, z_{Ei} the z-coordinate of the midpoint of edge *i* and ∂E represents the three element edges.

Combining (2.2) and (2.7) leads to the following matrix form:

$$\sum_{j=1}^{3} B_{ij}^E Q_j^E = \frac{\rho_0 g}{\mu_E}\left[\left(h_E + \frac{\left(\rho_E-\rho_0\right)}{\rho_0} z_E\right) - \left(Th_i^E + \frac{\left(\rho_E-\rho_0\right)}{\rho_0} z_i^E\right)\right] \tag{2.8}$$

where:

$$B_{ij} = \int_E \boldsymbol{w}_i^T \left(\boldsymbol{k}\right)^{-1} \boldsymbol{w}_j \tag{2.9}$$

If we define $\boldsymbol{r}_{ij}$ as the edge vector from node i toward node j, and l_{ij} by :

$$l_{ij} = \boldsymbol{r}_{ij}^T \left(\boldsymbol{k}\right)^{-1} \boldsymbol{r}_{ij} \tag{2.10}$$

l_{ij} verify the following properties:

$$l_{ij} - l_{jk} - l_{ik} = 2\boldsymbol{r}_{jk}^T \boldsymbol{k}^{-1} \boldsymbol{r}_{ki}\ ,\ \ i,j,k\ all\ different \tag{2.11}$$

which leads to:

$$\mathbf{B} = \frac{1}{48|E|}\begin{pmatrix} 3l_{12}+3l_{13}-l_{23} & -3l_{12}+l_{13}+l_{23} & l_{12}-3l_{13}+l_{23} \\ -3l_{12}+l_{13}+l_{23} & 3l_{12}-l_{13}+3l_{23} & l_{12}+l_{13}-3l_{23} \\ l_{12}-3l_{13}+l_{23} & l_{12}+l_{13}-3l_{23} & -l_{12}+3l_{13}+3l_{23} \end{pmatrix} \tag{2.12}$$

One notices that,

$$\sum_{j=1}^{3} B_{ij} = \frac{1}{48|E|}\left(l_{12}+l_{13}+l_{23}\right) = L \tag{2.13}$$

Despite the advantages of MFEs, the solution obtained is not unconditionally stable when using small time steps. To overcome this problem, Younes et al. [2006] developed a mass lumping procedure for the MFEs. The objective of this procedure is to avoid over and undershoots of the standard MFE method when the time step is too small. Small time steps may be necessary to

reach convergence for highly nonlinear problems. The main idea of the approach is to distribute sink/source term and accumulation term for each element over its edges. Due to this re-distribution, the new fluxes $\bar{Q}_i^E$ at the element level are defined by:

$$\sum_i \bar{Q}_i^E = 0 \tag{2.14}$$

Using (2.8) and $z_E = \frac{1}{3}\sum_{j=1}^{3} z_{Ej}$, leads to

$$h_E = \frac{1}{3}\sum_{j=1}^{3} Th_{Ej} \tag{2.15}$$

Inserting (2.15) into (2.8) the new flux through edge *i* is then:

$$\bar{Q}_i^E = \frac{\rho_0 g}{\mu_E}\left[\sum_j N_{ij} Th_j + \frac{\rho_E - \rho_0}{\rho_0}\sum_j N_{ij} z_{Ej}\right] \tag{2.16}$$

with

$$\boldsymbol{N} = -\frac{\det(\boldsymbol{k})}{|E|}\begin{bmatrix} \boldsymbol{r}_{23}^{\mathrm{T}}\boldsymbol{k}^{-1}\boldsymbol{r}_{23} & \boldsymbol{r}_{23}^{\mathrm{T}}\boldsymbol{k}^{-1}\boldsymbol{r}_{31} & \boldsymbol{r}_{23}^{\mathrm{T}}\boldsymbol{k}^{-1}\boldsymbol{r}_{12} \\ \boldsymbol{r}_{31}^{\mathrm{T}}\boldsymbol{k}^{-1}\boldsymbol{r}_{23} & \boldsymbol{r}_{31}^{\mathrm{T}}\boldsymbol{k}^{-1}\boldsymbol{r}_{31} & \boldsymbol{r}_{31}^{\mathrm{T}}\boldsymbol{k}^{-1}\boldsymbol{r}_{12} \\ \boldsymbol{r}_{12}^{\mathrm{T}}\boldsymbol{k}^{-1}\boldsymbol{r}_{23} & \boldsymbol{r}_{12}^{\mathrm{T}}\boldsymbol{k}^{-1}\boldsymbol{r}_{31} & \boldsymbol{r}_{12}^{\mathrm{T}}\boldsymbol{k}^{-1}\boldsymbol{r}_{12} \end{bmatrix} \tag{2.17}$$

The new flux $\bar{Q}_i^E$ corresponds to the actual flux under steady state conditions and without sink/source terms. The second step in the mass lumping procedure consists in writing continuity between elements *E* and *E'* having common edge *i*. The continuity is written including the 'equivalent steady state' new fluxes $\bar{Q}_i^E$, the storage and sink/source terms distributed over each element edge, which leads to:

$$\begin{aligned}\left[\bar{Q}_i + \frac{|E|}{3}\left(\frac{\rho_{ps}}{\rho} f_{ps} - \frac{\varepsilon}{\rho}\frac{\partial\rho}{\partial C}\frac{\partial C}{\partial t} - S\frac{Th_i^{n+1} - Th_i^n}{\Delta t}\right)\right]_E + \\ \left[\bar{Q}_i + \frac{|E'|}{3}\left(\frac{\rho_{ps}}{\rho} f_{ps} - \frac{\varepsilon}{\rho}\frac{\partial\rho}{\partial C}\frac{\partial C}{\partial t} - S_s\frac{Th_i^{n+1} - Th_i^n}{\Delta t}\right)\right]_{E'} = 0\end{aligned} \tag{2.18}$$

where the first and the second terms in (2.18) represent the characteristics restricted to element *E* (resp. *E'*). The fluxes $\bar{Q}_i^E$ are estimated at time *n+1*, which leads to the following system equation:

$$\left[\frac{\rho_0 g}{\mu}\sum_j N_{i,j}Th_j^{n+1}-\frac{1}{3}S_s|E|\frac{Th_i^{n+1}}{\Delta t}\right]_E+\left[\frac{\rho_0 g}{\mu}\sum_j N_{i,j}Th_j^{n+1}-\frac{1}{3}S_s|E'|\frac{Th_i^{n+1}}{\Delta t}\right]_{E'}=\left[-g\frac{\rho-\rho_0}{\mu}\sum_j N_{i,j}z_{Ej}-\frac{|E|}{3}\left(\frac{\rho_{ps}}{\rho}f_{ps}-\frac{\varepsilon}{\rho}\frac{\partial\rho}{\partial C}\frac{\partial C}{\partial t}+S_s\frac{Th_i^n}{\Delta t}\right)\right]_E+\left[-\frac{g\rho-\rho_0}{\mu}\sum_j N_{i,j}z_{Ej}-\frac{|E|}{3}\left(\frac{\rho_{ps}}{\rho}f_{ps}-\frac{\varepsilon}{\rho}\frac{\partial\rho}{\partial C}\frac{\partial C}{\partial t}+S_s\frac{Th_i^n}{\Delta t}\right)\right]_{E'} \quad (2.19)$$

Equation (2.19) represents the discretized flow equations (1.7) and (1.18). Because the simplified fluid mass balance (1.16) is used, the only time varying coefficients in the flow system matrix are the viscosity and the time step length. If it can be assumed that the viscosity remains constant and as long as the time step length is not modified, the system matrix does not change. In the standard approach, the fluid mass balance equation (1.9) is used and the flow matrix has to be built for each iteration. When the flow matrix is not re-build, direct solvers are very appropriate and the system matrix has to be factorized once.

2.1.2 Discretization of free flow

Introduction

Different methods can be used for the discretization of the Stokes equation [Langtangen and Mardal 2002]. Boffi et al. [2008] detailed the properties of the finite elements used for the Stokes problem, going from the cheapest element (Mini element, Me) to the most expensive one (Taylor-Hood, TH). Some of the presented elements do not satisfy the mass conservation properties. On the other side and due to stability conditions the system (1.24)-(1.25) cannot be discretized with the same order for pressure and velocity approximations. Otherwise some sort of stabilization is added to the mixed formulation [Li and Chen 2008]. To avoid these difficulties, we use the non-conforming Crouzeix-Raviart (CR) elements for the velocity approximation in combination with constant pressure per element, since they satisfy the Babuska-Brezzi condition [Brezzi and Fortin 1991, Girault and Raviart 1986, Gresho and Sani 1998]. This condition is central for ensuring that the final linear system to solve is non-singular [Langtangen 2002]. Moreover, the non-conforming Crouzeix-Raviart (CR) element has local mass conservation properties [Bruman and Hansbo 2004] and leads to a relatively small number of unknowns due to the low-order shape functions. The CR element is used in many problems such as the Darcy-

Stokes problem [Bruman and Hansbo 2005], the Stokes problem [Crouzeix and Raviart 1973] and the elasticity problem [Hansbo and Larson 2002, 2003]. The CR element gives a simple stable optimal order approximation of the Stokes equations [Arnold 1993]. In the next section, we recall the main stages for the discretization of the Stokes equation with the CR triangular element.

The non-conforming Crouzeix-Raviart element

With the non-conforming finite element method, the degrees of freedom for the velocity vector $\boldsymbol{u}$ are the two component (u_i, v_i) of $\boldsymbol{u}$ at the midedge i facing the node i (Figure 2). Inside the element E, we assume a linear variation of the velocity components (u_E, v_E)

$$u_E = u_i\varphi_i^E + u_j\varphi_j^E + u_k\varphi_k^E \quad , \quad v_E = v_i\varphi_i^E + v_j\varphi_j^E + v_k\varphi_k^E \qquad (2.20)$$

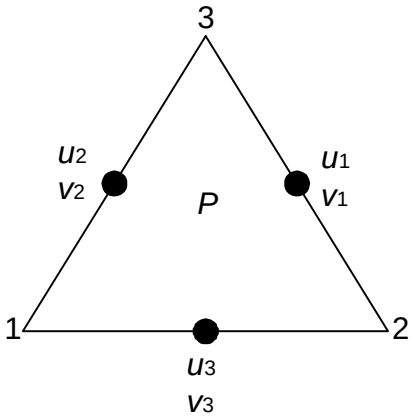

Figure 2: Crouziex-Raviart Finite element.

For an interior edge, the linear interpolation function φ_i for the velocity is nonzero only on the two adjacent elements E and E' (see Figure 3) with

$$\varphi_i^E = \frac{1}{|E|}\left[x(z_k - z_j) + y(x_j - x_k) + \frac{1}{2}(z_j x_k + z_j x_i - z_k x_i - z_k x_j - z_i x_j + z_i x_k) \right] \qquad (2.21)$$

where $|E|$ is the area of the element E, x_i and z_i are the coordinates of the vertex i of E. The interpolation function φ_i^E equals 1 on the midedge i and zero on the midedges j and k of E (Figure 3).

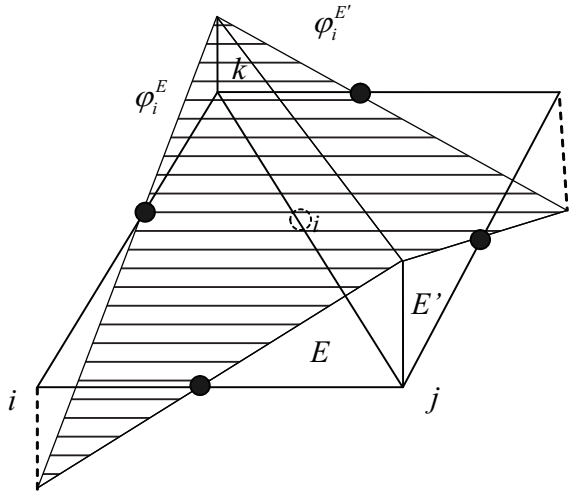

Figure 3: the linear interpolation function for the velocity field.

The variational formulation of the Stokes equation (1.24) using the test function φ_i over the domain Ω writes:

$$\int_{\Omega} \nabla.\left(\mu \nabla \boldsymbol{u} - p\boldsymbol{I}\right)\varphi_i = \int_{\Omega} \rho g \nabla z \varphi_i \tag{2.22}$$

where $\nabla \boldsymbol{u}$ is the gradient of the velocity vector $\boldsymbol{u}$ and $\boldsymbol{I}$ the 2×2 identity matrix.

Using Green's formula, we get

$$\int_{\partial\Omega} \varphi_i \left(\mu \nabla \boldsymbol{u} - p\boldsymbol{I}\right)\boldsymbol{\eta}_{\partial\Omega} - \int_{\Omega} \nabla.\left(\mu \nabla \boldsymbol{u} - p\boldsymbol{I}\right)\varphi_i = \int_{\Omega} \rho g \nabla z \varphi_i \tag{2.23}$$

The first integral contains boundary conditions. It vanishes in case of free-flow boundary or in case of an interior edge i. In this last case, equation (2.23) becomes

$$-\int_{E} \nabla.\left(\mu \nabla \boldsymbol{u}_E - p_E \boldsymbol{I}\right)\varphi_i^E - \int_{E'} \nabla.\left(\mu \nabla \boldsymbol{u}_{E'} - p_{E'} \boldsymbol{I}\right)\varphi_i^{E'} = \int_{E} \rho g \nabla z \varphi_i^E + \int_{E'} \rho g \nabla z \varphi_i^{E'} \tag{2.24}$$

Using (2.20) and (2.21), we obtain

$$-\int_{E} \nabla.\left(\mu \nabla \boldsymbol{u}_E - p_E \boldsymbol{I}\right)\varphi_i^E = \begin{pmatrix} \Delta z^i \\ \Delta x^i \end{pmatrix} P_E - \frac{\mu}{|E|} \begin{pmatrix} \sum_{j=1}^{3} \left(\Delta x^i \Delta x^j + \Delta z^i \Delta z^j\right) u_j \\ \sum_{j=1}^{3} \left(\Delta x^i \Delta x^j + \Delta z^i \Delta z^j\right) v_j \end{pmatrix} \tag{2.25}$$

and

$$\int_{E} \rho g \nabla z \varphi_i^E = \rho_E g \left(\overline{z}_i - z_E\right) \begin{pmatrix} \Delta z^i \\ \Delta x^i \end{pmatrix} \tag{2.26}$$

where $\Delta x^i = x_j - x_k$ and $\Delta z^i = z_k - z_j$, z_E and $\overline{z}_i$ are respectively the z-coordinate of the centre of E and of the midpoint of edge i, ρ_E and p_E are respectively the mean density and pressure over E. The finite volume formulation of the continuity equation (1.25) over the element E writes:

$$\int_E \nabla . \boldsymbol{u} = 0 \tag{2.27}$$

using (2.20), it becomes

$$\sum_{j=1}^{3} \left(\Delta z^j u_j + \Delta x^j v_j \right) = 0 \tag{2.28}$$

The final system to solve for the flow is obtained by writing equation (2.25) for each edge (two equations per edge) and equation (2.28) for each element.

2.2 Transport discretization

Introduction

For the transport equation, standard numerical methods, such as standard finite elements or finite volumes, are known to generate solution with numerical diffusion and/or non-physical oscillations when advection is dominant. These problems can be avoided with the discontinuous Galerkin method (DG) [Siegel et al. 1997]. Indeed, DG leads to a high-resolution scheme for advection that has been proven to be clearly superior to the already existing finite element methods [Arnold et al. 2002].

In this manuscript, the explicit DG method, where fluxes are upwinded using a Riemann solver is used to solve the advection equation and combined with the symmetric Multipoint Flux Approximation (MPFA) method for the diffusion equation. In the next section we show the discretization of the transport equation in free flow media. The discretization is quite the same in porous media, with some minor modifications (Darcy's velocity, porosity, dispersion tensor).

The DG-MPFA discretization

The transport equation (1.35) with no sink/source terms is written in the following mixed form [Younes et al. 2009, 2011]:

$$\begin{cases} \dfrac{\partial C}{\partial t} + \boldsymbol{u} . \nabla C + \nabla . \left(\boldsymbol{u}_D \right) = 0 \\ \boldsymbol{u}_D = -D \nabla C \end{cases} \tag{2.29}$$

The dispersive flux $\boldsymbol{u}_D$ is assumed to vary linearly inside the element E, therefore,

$$\nabla.\boldsymbol{u}_D = \frac{1}{|E|}\sum_i Q^E_{D,\partial Ei} \tag{2.30}$$

where $Q^E_{D,\partial Ei} = \int_{\partial Ei} \boldsymbol{u}_D.\boldsymbol{\eta}_{\partial Ei}$ is the dispersive flux across the edge ∂Ei of E.

We use the $P1$ DG method where the approximate solution $C_h(\boldsymbol{x},t)$ is expressed with linear basis functions ϕ_i^E on each element E as follows:

$$C_h(\boldsymbol{x},t)|_E = \sum_{i=1}^{3} C_i^E(t)\,\phi_i^E(\boldsymbol{x}) \tag{2.31}$$

where $C_i^E(t)$ are the three unknown coefficients corresponding to the degrees of freedom which are the average value of the mass fraction defined at the triangle centroid $(\overline{x}_E, \overline{z}_E)$ and its deviations in each space direction [Cockburn et al. 1989] with the corresponding interpolation functions:

$$\phi_1^E(x,z) = 1, \quad \phi_2^E(x,z) = x - \overline{x}_E, \ \phi_3^E(x,z) = z - \overline{z}_E. \tag{2.32}$$

The variational formulation of (2.29) over the element E using ϕ_i^E as test functions leads to:

$$\begin{aligned}\sum_j \frac{\partial C_j^E}{\partial t}\int_E \phi_j^E\phi_i^E - \sum_j \int_E C_j^E\phi_j^E\,\boldsymbol{u}.\nabla\phi_i^E - \sum_j \int_E C_j^E\phi_j^E\,\phi_i^E\nabla.\boldsymbol{u} \\ + \int_{\partial E} C^*\phi_i^E\,\boldsymbol{u}.\boldsymbol{\eta}_{\partial E} + \int_E \frac{1}{|E|}\sum_{\partial Ej} Q^E_{D,j}\,\phi_i^E = 0\end{aligned} \tag{2.33}$$

This could be written in the following matrix form:

$$[A]\begin{pmatrix}\frac{dC_1^E}{dt}\\ \frac{dC_2^E}{dt}\\ \frac{dC_3^E}{dt}\end{pmatrix} = [B]\begin{bmatrix}C_1^E\\ C_2^E\\ C_3^E\end{bmatrix} - \left[M^0\right]\begin{bmatrix}C_1^E\\ C_2^E\\ C_3^E\end{bmatrix} - \sum_{\ell=1}^{3}\left[M^\ell\right]\begin{bmatrix}C_1^{E\ell}\\ C_2^{E\ell}\\ C_3^{E\ell}\end{bmatrix} + \begin{bmatrix}\sum_{\partial Ej} Q^E_{D,j}\\ 0\\ 0\end{bmatrix} \tag{2.34}$$

with,

$$A_{i,j} = \int_E \phi_j^E\phi_i^E \qquad B_{i,j} = \int_E \phi_j^E\,\boldsymbol{u}.\nabla\phi_i^E$$

$$M^0_{i,j} = \sum_{\ell=1}^{N_E}\lambda^E_{\partial E\ell}\frac{Q^E_{\partial E\ell}}{|\partial E\ell|}\int_{\partial E\ell}\phi_i^E\,\phi_j^E, \qquad M^\ell_{i,j} = \left(1-\lambda^E_{\partial E\ell}\right)\frac{Q^E_{\partial E\ell}}{|\partial E\ell|}\int_{\partial E\ell}\phi_i^E\,\phi_j^{E\ell} \quad (\ell = 1,..,3)$$

where Ej is the adjacent element to E such that ∂Ej is the common edge of E and Ej and $Q^E_{\partial E\ell} = \int_{\partial E\ell} \boldsymbol{u}.\boldsymbol{\eta}_{\partial Ej}$ the water flux across ∂Ej. The upwind parameter $\lambda^E_{\partial E\ell}$ is defined by

$$\lambda^E_{\partial Ej} = \begin{cases} 1 & if \quad \boldsymbol{u}.\boldsymbol{\eta}_{\partial Ej} \geq 0 \\ 0 & if \quad \boldsymbol{u}.\boldsymbol{\eta}_{\partial Ej} < 0 \end{cases} \tag{2.35}$$

An explicit time discretization is used for the equation (2.34). An efficient geometric slope limiter is used to avoid unphysical oscillations near sharp fronts [Younes et al. 2010b].

The dispersive fluxes $Q^E_{D,j}$ across edges are approximated using the MPFA method. The basic idea of this method is to divide each triangle into 3 sub-cells as in Figure 4.

Inside the sub-cell (O,F_1,G,F_2) formed by the corner O, the centre G and the midpoint edges F_1 and F_2, we assume linear variation of the mass fraction between C_1^E, TC_1 and TC_2, the mass fractions respectively at G and the two continuity points f_1 and f_2. The symmetry of the MPFA is achieved when the continuity points are localized at $\frac{Of_1}{OF_1} = \frac{Of_2}{OF_2} = \frac{2}{3}$. In this case (O, f_1, G, f_2) is a parallelogram. Therefore, half-edge fluxes $\left(Q^1_O = \int_O^{F_1} -D\nabla C \text{ and } Q^2_O = \int_O^{F_2} -D\nabla C \right)$, taken positive for outflow simplifies to [Younes and Fontaine 2008b]:

$$\begin{pmatrix} Q^1_O \\ Q^2_O \end{pmatrix} = \beta_E \begin{pmatrix} -\overrightarrow{OF_1}.\overrightarrow{OF_1} & \overrightarrow{OF_1}.\overrightarrow{OF_2} \\ \overrightarrow{OF_1}.\overrightarrow{OF_2} & -\overrightarrow{OF_2}.\overrightarrow{OF_2} \end{pmatrix} \begin{pmatrix} TC_1 - C_1^E \\ TC_2 - C_1^E \end{pmatrix} \tag{2.36}$$

with $\beta_E = 3D/|E|$.

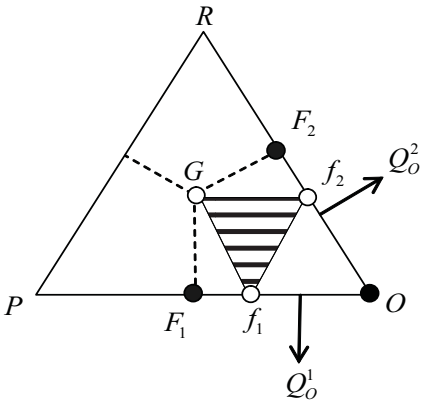

Figure 4: Triangle splitting into three sub-cells and linear concentration approximation on the sub-cell.

This system is written for all sub-cells sharing the vertex O which create an interaction region. Then by writing continuity of diffusive fluxes across half-edges and continuity of mass fraction at continuity points, we obtain a local system $[A](TC)=[B](C)$. This local system is solved to obtain the mass fraction at the continuity points (TC_i) as function of mass fraction at all elements sharing the vertex O. The obtained relation is then substituted into (2.36) to obtain half-edge fluxes explicitly as a weighted sum of the cell mass fraction of the interaction volume. Finally, the summation of these fluxes is written using an implicit time discretization and substituted into the equation (2.34).

2.3 Dissolution

The DG method is also used for the discretization of the dissolution equation. Hence, multiplying the dissolution equation (1.37) by the test function ϕ_i^E defined in (2.32) we get:

$$\int_E \lambda_E (C_{sat}-C)\phi_i^E = \lambda_E C_{sat}\int_E \phi_i^E - \lambda_E \theta \int_E C^{n+1}\phi_i^E - \lambda_E (1-\theta)\int_E C^n \phi_i^E \tag{2.37}$$

where C^n and C^{n+1} are the concentrations at the time step n and $n+1$ respectively. We use a θ time discretization where θ is such that:

$$\theta = \begin{cases} 0, \textit{ for a full explicit scheme} \\ 1, \textit{ for a full implicit scheme} \end{cases} \tag{2.38}$$

The first right side term in (2.37) is treated as a constant quantity and is therefore added to the right hand side term of the global transport equation. The last two terms in (2.37) are added to equation (2.34).

Chapter 3

Semi-analytical and numerical solutions for density driven flow in porous domains

Contents

Semi-analytical and numerical solutions for density driven flow in porous domains

Paper published in water resources research journal

The Henry semianalytical solution for saltwater intrusion with reduced dispersion

Ali Zidane[(1,2)], Anis Younes[(2)] , Peter Huggenberger[(1)], Eric Zechner[(1)]

(1) Institute of Geology and Paleontology, Environmental Sciences Department, University of Basel, Bernouillistr. 32, 4056 Basel, Switzerland

(2) Laboratoire d'Hydrologie et de Geochimie de Strasbourg, University of Strasbourg, CNRS UMR 7517, Strasbourg, France

The Henry semianalytical solution for saltwater intrusion with reduced dispersion

Ali Zidane,[1,2] Anis Younes,[1] Peter Huggenberger,[2] and Eric Zechner[2]

Received 18 July 2011; revised 7 May 2012; accepted 11 May 2012; published 27 June 2012.

[1] The Henry semianalytical solution for salt water intrusion is widely used for benchmarking density dependent flow codes. The method consists of replacing the stream function and the concentration by a double set of Fourier series. These series are truncated at a given order and the remaining coefficients are calculated by solving a highly nonlinear system of algebraic equations. The solution of this system is often subject to substantial numerical difficulties. Previous works succeeded to provide semianalytical solutions only for saltwater intrusion problems with unrealistic large amount of dispersion. In this work, different truncations for the Fourier series are tested and the Levenberg-Marquardt algorithm, which has a quadratic rate of convergence, is applied to calculate their coefficients. The obtained results provide semianalytical solutions for the Henry problem in the case of reduced dispersion coefficients and for two freshwater recharge values: the initial value suggested by Henry (1964) and the reduced one suggested by Simpson and Clement (2004). The developed semianalytical solutions are compared against numerical results obtained by using the method of lines and advanced spatial discretization schemes. The obtained semianalytical solutions improve considerably the worthiness of the Henry problem and therefore, they are more suitable for testing density dependent flow codes.

Citation: Zidane, A., A. Younes, P. Huggenberger, and E. Zechner (2012), The Henry semianalytical solution for saltwater intrusion with reduced dispersion, *Water Resour. Res.*, *48*, W06533, doi:10.1029/2011WR011157.

1. Introduction

[2] Saltwater intrusion into unconfined coastal aquifers has been largely investigated using laboratory experiments [e.g., *Goswami and Clement*, 2007; *Thorenz et al.*, 2002] and/or numerical simulations [e.g., *Park and Aral*, 2008]. However, the existence of a semianalytical solution made the synthetic Henry saltwater intrusion problem [*Henry*, 1964] as one of the most widely tests used for verification of density driven flow codes. The problem describes steady state saltwater intrusion through an isotropic confined aquifer. Freshwater enters the idealized rectangular aquifer (Figure 1) with a constant flux rate from the inland (left) boundary. A hydrostatic pressure is prescribed along the coast (right) boundary where the concentration corresponds to seawater concentration. The top and the bottom of the domain are impermeable boundaries. The saltwater intrudes from the right until an equilibrium with the injected freshwater is reached. The semianalytical solution of Henry [*Henry*, 1964] provides the steady state isochlors positions by expanding the salt concentration and the stream function in double Fourier series. *Henry* [1964] used only 78 terms in these series and calculated the coefficients using a Gauss elimination procedure with full pivoting. *Pinder and Cooper* [1970] were the first to simulate the Henry problem using a transient numerical code with two different initial conditions to ensure convergence to the steady state solution. The obtained results as well as those obtained later by [*Segol et al.*, 1975; *Frind*, 1982; *Huyakorn et al.*, 1987] were not in agreement with Henry's solution. In 1987, *Voss and Souza* [1987] showed that the discrepancies in the published papers were due to the use of different dispersion coefficients in numerical and semianalytical calculations. However, solving this problem did not lead to a satisfactory matching. Many possible reasons for the discrepancies have been invoked in the literature: for *Huyakorn et al.* [1987], the discrepancies may be due to the discretization errors within the numerical codes and/or to the use of different boundary conditions at the seaward side between semianalytical and numerical codes. Indeed, the sea boundary condition used in the work of *Frind* [1982], *Huyakorn et al.* [1987], and *Voss and Souza* [1987] was not consistent with the original Henry problem. *Croucher and O'Sullivan* [1995] presented a grid convergence study to evaluate the truncation error due to the spatial discretization. *Kolditz et al.* [1998] claimed that the discrepancies may be due to the inaccuracy of the Boussinesq approximation assumed by Henry.

[3] The most important reason for discrepancies has been invoked by *Voss and Souza* [1987] who claimed that, due to the lack of computing resources, Henry's truncation may not contain enough terms in the Fourier series to

[1]Laboratoire d'Hydrologie et de Geochimie de Strasbourg, CNRS, UMR 7517, University of Strasbourg, Strasbourg, France.
[2]Department of Environmental Sciences, Institute of Geology and Paleontology, University of Basel, Basel, Switzerland.

Corresponding author: A. Younes, Laboratoire d'Hydrologie et de Geochimie de Strasbourg, CNRS, UMR 7517, University of Strasbourg, 1 rue Blessig, 67084, Strasbourg Cedex, France. (younes@unistra.fr)

0043-1397/12/2011WR011157

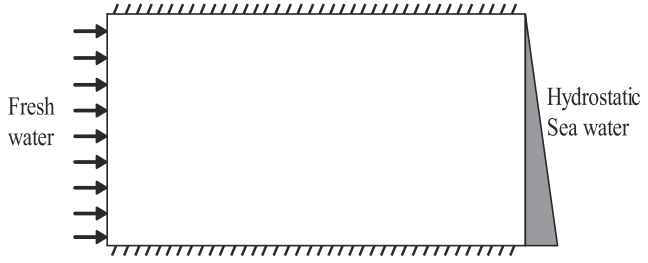

Figure 1. Domain and boundary conditions for the Henry saltwater intrusion problem.

represent accurately the solution. In 1994, *Segol* [1994] revaluated the semianalytical solution of Henry by using a new truncation of the Fourier series with 138 terms instead of the 78 used by Henry. The revaluated solution shows a good agreement with the numerical results [e.g., *Oldenbourg and Prues*, 1995; *Herbert et al.*, 1988; *Ackerer et al.*, 1999; *Buès and Oltéan*, 2000; *Abarca et al.*, 2007, *Younes et al.*, 2009].

[4] In 2003, *Simpson and Clement* [2003] performed a coupled versus uncoupled analysis to show that the true profile in the Henry problem is largely determined by boundary forcing and much less by the density-dependent effects. In the uncoupled flow, the solute transport acts as a tracer and has no influence on the flow equation. To improve the worthiness of the Henry problem, they suggested a decreasing of the fresh water recharge by half [*Simpson and Clement*, 2004]. The semianalytical solution is revaluated in this case by using 203 terms in the Fourier series [*Simpson and Clement*, 2004].

[5] *Henry* [1964], *Segol* [1994], and *Simpson and Clement* [2004] used the same iterative technique to calculate the coefficients of the Fourier series. They solved the nonlinear system as a system of linear equations where the expansion coefficients are considered as unknowns. The nonlinear right hand side is treated as a known quantity, updated iteratively until convergence. As stated by *Segol* [1994], this technique encountered substantial convergence difficulties for small values of the dispersion coefficient. Note that all published works succeeded to develop semianalytical solutions only when an unrealistically large amount of dispersion is introduced in the solution. This deficiency was pointed out by *Kolditz et al.* [1998] and by *Voss and Souza* [1987, p. 1857], who stated that due to the large amount of dispersion, "this test does not check whether a model is consistent or whether it accurately represents density driven flows, nor does it check whether a model can represent field situation with relatively narrow transition zones."

[6] In this work, we calculate the coefficients of the Fourier series by using the Levenberg-Marquardt algorithm, which has a quadratic rate of convergence, to solve the nonlinear algebraic system of equations. Different truncations of the infinite Fourier series are tested. Semianalytical solutions for the Henry problem are developed in the case of reduced dispersion coefficients and for two freshwater recharge values: the initial value suggested by Henry and the reduced one suggested by *Simpson and Clement* [2004]. The semianalytical solutions are compared against numerical results obtained using a robust numerical model based on the method of lines and advanced spatial discretization schemes [*Younes et al.*, 2009].

2. Semianalytical Method

[7] To obtain the semianalytical solution, *Henry* [1964] used a constant dispersion coefficient and assumed the Boussinesq approximation valid which implies the existence of stream function. Using these assumptions, the steady state flow and transport can be written in the following nondimensional form [*Henry*, 1964, *Segol*, 1994]:

$$a\left(\frac{\partial^2\psi}{\partial x^2}+\frac{\partial^2\psi}{\partial y^2}\right)=\frac{\partial C}{\partial x}+\frac{1}{\xi}, \tag{1}$$

$$b\left(\frac{\partial^2 C}{\partial x^2}+\frac{\partial^2 C}{\partial y^2}\right)=\frac{\partial\psi}{\partial y}\frac{\partial C}{\partial x}-\frac{\partial\psi}{\partial x}\frac{\partial C}{\partial y}+\frac{1}{\xi}\frac{\partial\psi}{\partial y}+\frac{\partial C}{\partial x}+\frac{1}{\xi}, \tag{2}$$

where ψ is the dimensionless stream function, C is the dimensionless concentration, $\xi=\frac{L}{d}$ is the aspect ratio of the domain with L and d, which are the length and the depth of the aquifer, respectively.

[8] The nondimensional parameters a and b in the previous equations are given by

$$a=\frac{Q}{k_1 d} \text{ and } b=\frac{D}{Q}, \tag{3}$$

where Q [L^2T^{-1}] is the freshwater recharge, D [L^2T^{-1}] is the coefficient of dispersion, $k_1=K\left(\frac{\rho_s-\rho_0}{\rho_0}\right)$ with K [LT^{-1}] the saturated hydraulic conductivity, ρ_0 [ML^{-3}] and ρ_s [ML^{-3}] are the freshwater and saltwater densities, respectively.

[9] The solution technique, known as Galerkin or Fourier-Galerkin solution [*Forbes*, 1988], is obtained by replacing the stream function and the salt concentration by double Fourier series of the form:

$$\psi=\sum_{m=1}^{\infty}\sum_{n=0}^{\infty}A_{m,n}\sin(m\pi y)\cos\left(n\pi\frac{x}{\xi}\right), \tag{4}$$

$$C=\sum_{r=0}^{\infty}\sum_{s=1}^{\infty}B_{r,s}\cos(r\pi y)\sin\left(s\pi\frac{x}{\xi}\right). \tag{5}$$

[10] Substituting these relations into equations (1) and (2), multiplying equation (1) by $4\sin(g\pi y)\cos(h\pi\frac{x}{\xi})$ and equation (2) by $4\cos(g\pi y)\sin(h\pi\frac{x}{\xi})$, and integrating over the rectangular domain gives an infinite set of algebraic equations for $A_{g,h}$ and $B_{g,h}$ namely,

$$\varepsilon_2 a\pi^2 A_{g,h}(g^2+h^2)\xi=\sum_{r=0}^{\infty}B_{r,h}hN(g,r)+\frac{4}{\pi}W(g,h), \tag{6}$$

$$\varepsilon_1 b\pi^2 B_{g,h}\left(g^2+\frac{h^2}{\xi^2}\right)\xi=\sum_{n=0}^{\infty}A_{g,n}gN(h,n)+\varepsilon_1\sum_{s=1}^{\infty}B_{g,s}sN(h,s)+Quad+\frac{4}{\pi}W(h,g). \tag{7}$$

[11] The functions ε_1, ε_2, N, W and $Quad$ are detailed in Appendix A.

[12] *Segol* [1994, p. 272] wrote about how *Henry* [1964] described his solution of the set of algebraic equations (6) and (7): "An iterative solution of equation (6) was used in which the $B_{0,h}$ were computed by several sub iterations and vice versa. The subiterative cycle consisted of recomputing the values of the quadratic terms (*Quad*) using the revised values of $B_{g,h}$ ($g > 0$) while continuing to hold the $B_{0,h}$ constant and then using these values to recompute the $B_{g,h}$ ($g > 0$)."

[13] This procedure for computing the coefficients of the Fourier series was also used by *Segol* [1994] and *Simpson and Clement* [2004]. The convergence rate of the method depends upon the values of the parameters a and b. To overcome the convergence difficulties, *Segol* [1994] and *Simpson and Clement* [2004] used the solution with the parameters $a = 0.263$ and $b = 0.2$ as an initial guess for the other parameterizations. Then, the parameters a and b, are reduced with small stepwise changes until the desired solution is obtained. *Segol* [1994] stated that the value $b = 0.1$ was the lower limit of the range for which a stable and convergent solution can be obtained.

3. New Semianalytical Strategy and Numerical Code

[14] In the first part of this section, we describe the new strategy used for solving the nonlinear system of algebraic equations to calculate the Fourier series coefficients of the semianalytical solution. In the second part, we briefly describe the numerical code used to compare numerical and semianalytical results.

3.1. Semianalytical Strategy

[15] The procedure used by *Henry* [1964], *Segol* [1994] and *Simpson and Clement* [2004] encounters substantial numerical difficulties because of its low convergence rate when lowering the values of the parameters a and/or b. Indeed, *Segol* [1994] stated that when lowering the value of b, more coefficients are required to obtain a stable solution and the convergence of the scheme becomes difficult. To obtain a stable solution, *Segol* [1994] decreased the value of b by considering small stepwise changes and iterating at intermediate steps. The value $b = 0.1$ was the lower limit of the range for which a stable and convergent solution can be obtained.

[16] To avoid these difficulties, we use in this work the Levenberg-Marquardt algorithm [*Levenberg*, 1944; *Marquardt*, 1963], which has a quadratic rate of convergence to solve the set of nonlinear algebraic equations [*Yamashita and Fukushima*, 2001]. The Levenberg-Marquardt method is considered as one of the most efficient algorithms for solving systems of nonlinear equations. The nonlinear algebraic system of equations (6)–(7) is written in the form $\mathbf{F}(\mathbf{X}) = 0$ where $\mathbf{X}$ is a vector formed by the coefficients $A_{g,h}$ and $B_{g,h}$. The algorithm attempts to minimize the sum of the squares of the function. The method is a combination of two minimization methods: the gradient descent method and the Gauss-Newton method. Far from the optimum, the Levenberg-Marquard method behaves like a gradient descent method, whereas, it acts like the Gauss-Newton method nearby the optimum.

[17] The Levenberg-Marquardt iterates starting from an initial solution $\mathbf{X}_0$. At each iteration k, the new solution $\mathbf{X}_{k+1} = \mathbf{X}_k + \mathbf{d}_k$ is obtained from the solution of the following linear system

$$\Big(\mathbf{J}(\mathbf{X}_k)^T\mathbf{J}(\mathbf{X}_k) + \lambda_k\mathbf{I}\Big)\mathbf{d}_k = -\mathbf{J}(\mathbf{X}_k)^T\mathbf{F}(\mathbf{X}_k), \tag{8}$$

where $\mathbf{J}$ is the Jacobian.

[18] Small values of the parameter λ_k correspond to the Gauss-Newton update while the large ones correspond to the gradient descent update. When the solution approaches the minimum, the parameter λ_k is decreased, what makes the algorithm tends to the Gauss-Newton method.

[19] In this study the Jacobian $\mathbf{J}$ is approximated numerically using finite differences and the Levenberg-Marquardt parameter is initially fixed to $\lambda_0 = 0.01$. During iterations, if the new estimate is sufficiently better than the old one, the parameter λ is reduced by ten. Otherwise it is increased by a factor of two. The tolerance is fixed to 10^{-12} for the sum of the squares of the function.

3.2. Numerical Code

[20] The semianalytical results will be compared against accurate numerical results obtained using a combination of the method of lines and advanced spatial discretization schemes.

[21] The flow system is written in terms of equivalent fresh water head [*Huyakorn et al.*, 1987]:

$$\rho S\frac{\partial h}{\partial t} + \varepsilon\frac{\partial \rho}{\partial C}\frac{\partial C}{\partial t} + \rho\nabla\cdot\mathbf{q} = 0, \tag{9}$$

$$\mathbf{q} = -\frac{\rho_0 g}{\mu}\mathbf{k}\left(\nabla h + \frac{\rho-\rho_0}{\rho_0}\nabla z\right), \tag{10}$$

where ρ is the fluid density [ML^{-3}], S the specific mass storativity related to head changes [L^{-1}], h the equivalent freshwater head [L], t the time [T], ε the porosity [-], C the solute mass fraction [M. salt/M. fluid], $\mathbf{q}$ the Darcy's velocity [LT^{-1}], ρ_0 the density of the displaced fluid [ML^{-3}], g the gravity acceleration [LT^{-2}], μ the fluid dynamic viscosity [$ML^{-1}T^{-1}$], $\mathbf{k}$ the permeability tensor [L^2] and z the depth [L].

[22] The solute mass conservation is written in term of mass fraction:

$$\frac{\partial(\varepsilon\rho C)}{\partial t} + \nabla\cdot(\rho C\mathbf{q} - \rho\mathbf{D}\nabla C) = 0. \tag{11}$$

[23] For the Henry problem, the dispersion tensor is assumed constant $D = D^*\mathbf{I}$ ($\mathbf{I}$ is the identity matrix) and the density is assumed to vary linearly with respect to the mass fraction. Due to the form of the governing equation used by Henry, the value of the dispersion coefficient D^* used in the numerical code is equal to the value used in the semianalytical solution divided by porosity ($D^* = D/\varepsilon$).

[24] To achieve high accuracy for the spatial discretization, each equation within the flow-transport system (9)–(11) is modeled with a specific numerical method. The flow equation is discretized with the locally mass conservative Mixed Finite Element method (MFE), that produces accurate and consistent velocity field [*Ackerer and Younes*, 2008; *Younes et al.*, 2009; *Younes et al.*, 2010]. The advection part of the

transport equation is discretized with the Discontinuous Galerkin (DG) method which produces accurate solution even for problems involving sharp fronts [*Siegel et al.*, 1997]. Finally, the multi-point flux approximation (MPFA) is used to discretize the dispersion equation [*Younes and Ackerer*, 2008] since it is locally conservative and can treat general irregular grids on anisotropic heterogeneous domains [*Aavatsmark*, 2002; *Younes and Fontaine*, 2008a, 2008b]. The combination of the three spatial discretization methods MPFA, DG and MFE, has proven to be accurate and robust for modeling density driven flow problems [*Younes and Ackerer*, 2008; *Konz et al.*, 2009: *Zechner et al.*, 2011].

[25] The Differential Algebraic Solver with Preconditioned Krylov (DASPK) time solver is used to solve the MFE_DG_MPFA spatial discretization with the method of lines. DASPK is a mature and sophisticated time integration package for large-scale Ordinary Differential Equations (ODE) or Differential Algebraic Equations (DAE) systems. DASPK uses the Fixed Leading Coefficient Backward Difference Formulas (FLCBDF). The BDF approach works well on stiff problems and has good stability properties. DASPK solves systems of the general form:

$$\mathbf{F}(t, \mathbf{y}, \mathbf{y}') = 0. \tag{12}$$

[26] Predictor and corrector polynomials are constructed in order to estimate the truncation error. The time step length and choice of order of integration (up to fifth order) are adapted to minimize the computational effort while keeping the local temporal truncation error τ_i small, $\tau_i \leq \varepsilon_i = \varepsilon_r|\mathbf{y}_i| + \varepsilon_a$ where the relative ε_r and absolute ε_a local error tolerances are specified by the user.

[27] In this study, the Henry problem is discretized with a uniform triangular mesh of 3200 elements (same results were obtained with 5000 and 8000 elements).

4. Results and Discussion

[28] As stated, by *Abarca et al.* [2007], the drawbacks of the Henry problem arise from the high values of the parameters a and b that Henry used to obtain the semianalytical solution. Indeed, Henry chose the dimensionless parameters $\xi = 2.0$, $a = 0.263$ and $b = 0.1$. *Segol* [1994] stated that the value $b = 0.1$ was the lower limit of the range for which a stable and convergent solution can be obtained. *Simpson and Clement* [2004] proposed a semianalytical solution where the parameter a is reduced by half and the parameter b is increased by a factor of 2 ($\xi = 2.0$, $a = 0.1315$ and $b = 0.2$). In this section, the semianalytical solution for the Henry problem is calculated using the Levenberg-Marquardt algorithm and compared to the numerical solution for different test cases. Table 1 provides the freshwater flux, the saltwater density and the diffusion coefficients for each test case. Two values for the parameter a are tested: the initial one and the halved one. The values of the parameter b are reduced until $b = 0.02$ (Table 1). Different truncations of the Fourier series are tested: the 78 coefficients of *Henry* [1964], the 138 coefficients of *Segol* [1994] and the 203 coefficients of *Simpson and Clement* [2004]. A new truncation using 424 terms is introduced to calculate the semianalytical solution in the case of small dispersion values. Two domains are used for the calculation of the semianalytical solution: the initial domain with an aspect ratio $\xi = L/d = 2$ and a larger domain with $\xi = 3$ (Table 1). Three concentration isochlors (0.25, 0.5 and 0.75) are used for the comparison between the semianalytical and the numerical solutions. Table 2 provides the position of the three isochlors for the new provided test cases. The transient numerical simulations are performed until a long time to ensure a steady state solution. Figure 2 shows the temporal variation of the concentration in the element corresponding to the intersection of the 0.25 isochlor with the base at $t = 800$ min for the studied test cases. The results show that the time required to reach a steady state depends on the parameters a and b. For all test cases, 500 min of time seems to be sufficient to obtain a steady position for the isochlors.

4.1. Case 1: The Standard Henry Problem With $a = 0.263$, $b = 0.1$, and $\xi = 2.0$

[29] This case is the standard test case solved by *Henry* [1964] on an IBM 650 digital computer using 38 coefficients for the expansion of the stream function and 40 coefficients for the expansion of the concentration. *Segol* [1994] revaluated the semianalytical solution using an expansion with 38 coefficients for the stream function and 100 coefficients for the concentration. *Simpson and Clement* [2004] calculated the solution using 103 and 100 coefficients for the expansion of the stream function and concentration, respectively. The same iteration procedure, including a number of subiterations, was used by all the authors.

[30] We recalculate this standard test case with the Levenberg-Marquardt algorithm using the 78 coefficients of Henry, the 138 coefficients of Segol and the 203 coefficients of Simpson and Clement. Figure 3 compares the new calculated isochlors and the semianalytical solution of *Segol* [1994] to the numerical solution.

Table 1. Aspect Ratio, Freshwater Reacharge, Saltwater Density, Diffusion Coefficient and the Parameters $(a; b)$ for the Different Test Cases

	$\xi = \frac{L}{d}$	Q ($m^2 s^{-1}$)	ρ_s ($kg m^{-3}$)	$D = \varepsilon D^*$ ($m^2 s^{-1}$)	$a = \frac{Q\rho_0}{K(\rho_s - \rho_0)d}$	$b = \frac{D}{Q}$
Case 1	2	6.610^{-5}	1025	6.610^{-6}	0.263	0.1
Case 2	2	3.310^{-5}	1025	6.610^{-6}	0.1315	0.2
Case 3	2	3.310^{-5}	1025	3.310^{-6}	0.1315	0.1
	2	6.610^{-5}	1050	6.610^{-6}	0.1315	0.1
Case 4	2	6.610^{-5}	1025	2.6410^{-6}	0.263	0.04
Case 5	2	6.610^{-5}	1025	1.3210^{-6}	0.263	0.02
Case 6a	2	3.310^{-5}	1025	1.3210^{-6}	0.1315	0.04
Case 6b	3	3.310^{-5}	1025	1.3210^{-6}	0.1315	0.04

Table 2. Position of the 0.25, 0.5 and 0.75 Isochlors for the Test Cases 3, 4, 5 and 6b

	Case 3 ($a = 0.1315$, $b = 0.1$, $\xi = 2.0$)			Case 4 ($a = 0.263$, $b = 0.04$, $\xi = 2.0$)			Case 5 ($a = 0.263$, $b = 0.02$, $\xi = 2.0$)			Case 6b ($a = 0.263$, $b = 0.04$, $\xi = 3.0$)		
$z =$	(0.25) $x =$	(0.5) $x =$	(0.75) $x =$	(0.25) $x =$	(0.5) $x =$	(0.75) $x =$	(0.25) $x =$	(0.5) $x =$	(0.75) $x =$	(0.25) $x =$	(0.5) $x =$	(0.75) $x =$
0.000	0.540	0.824	1.167	1.043	1.184	1.375	0.951	1.048	1.200	1.217	1.458	1.806
0.050	0.549	0.836	1.181	1.054	1.199	1.392	0.968	1.072	1.230	1.233	1.482	1.832
0.100	0.570	0.867	1.216	1.079	1.233	1.432	1.006	1.125	1.291	1.272	1.538	1.895
0.150	0.604	0.914	1.268	1.115	1.282	1.484	1.058	1.195	1.369	1.329	1.619	1.983
0.200	0.649	0.974	1.331	1.161	1.341	1.543	1.123	1.274	1.447	1.402	1.716	2.084
0.250	0.697	1.043	1.401	1.213	1.400	1.607	1.190	1.349	1.526	1.489	1.826	2.191
0.300	0.761	1.121	1.475	1.272	1.464	1.666	1.265	1.433	1.604	1.587	1.941	2.297
0.350	0.826	1.204	1.548	1.335	1.537	1.728	1.341	1.506	1.672	1.696	2.060	2.399
0.400	0.904	1.291	1.619	1.402	1.602	1.781	1.422	1.582	1.739	1.812	2.178	2.495
0.450	0.985	1.380	1.687	1.470	1.666	1.831	1.501	1.655	1.800	1.935	2.294	2.585
0.500	1.081	1.468	1.750	1.540	1.730	1.876	1.571	1.725	1.854	2.060	2.405	2.669
0.550	1.176	1.555	1.807	1.610	1.784	1.915	1.649	1.784	1.901	2.187	2.510	2.745
0.600	1.279	1.638	1.857	1.680	1.842	1.943	1.719	1.842	1.938	2.313	2.610	2.813
0.650	1.383	1.717	1.900	1.748	1.890	1.963	1.784	1.896	1.966	2.436	2.701	2.872
0.700	1.487	1.791	1.930	1.813	1.929	1.977	1.848	1.938	1.985	2.556	2.784	2.920
0.750	1.593	1.856	1.956	1.874	1.957	1.992	1.901	1.966		2.668	2.859	2.957
0.800	1.700	1.907	1.975	1.923	1.974		1.946	1.991		2.773	2.918	2.983
0.850	1.795	1.944	1.991	1.953	1.985		1.971			2.866	2.962	
0.900	1.882	1.967		1.970			1.996			2.938	2.993	
0.950	1.929	1.987		1.984						2.978		
1.000	1.946											

[31] The semianalytical solution obtained using the Henry truncation (78 terms) presents strong oscillations along the three isochlors (0.25, 0.5 and 0.75). This shows that the Henry solution was in error not because the full equilibrium solution was not reached, but rather because of the limited number of coefficients used in the Fourier series. Note that *Segol* [1994] stated that the values obtained by Henry are interpolated and "are drawn to eliminate local variations that appear due to truncation of Fourier series".

[32] The Simpson and Clement truncation gives the same semianalytical solution (not plotted in Figure 3) than the Segol truncation (138 terms). Contrarily to the solution of *Segol* [1994], which is slightly shifted to the right (especially the 0.75 isochlor), the calculated semianalytical solution has an excellent agreement with the numerical solution (Figure 3).

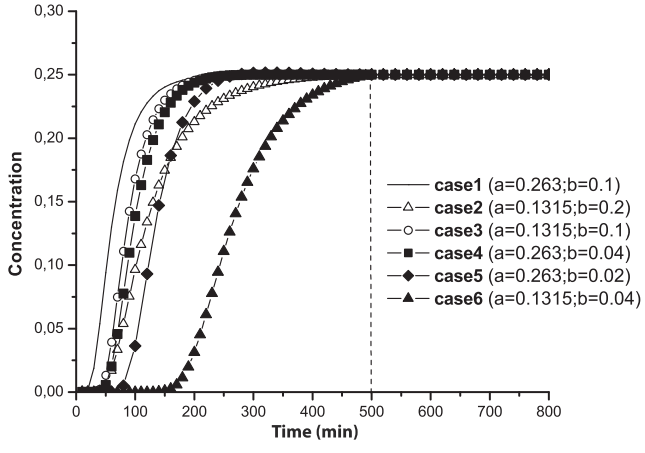

Figure 2. Temporal variation of the concentration in the element corresponding to the intersection of the 0.25 isochlor with the base at $t = 800$ min for the studied test cases.

4.2. Case 2: The Modified Henry Problem With $a = 0.1315$, $b = 0.2$, and $\xi = 2.0$

[33] *Simpson and Clement* [2004] discussed the worthiness of the Henry problem by comparing the isochlors obtained with the coupled and uncoupled flow transport models. To increase the density-dependent effects compared to boundary forces, they proposed to decrease the freshwater recharge by half. Compared to the previous test case, the parameter a is reduced by 50% and the parameter b is increased by a factor of 2.

[34] The semianalytical solution is revaluated using a scheme of 203 terms. To facilitate the convergence, they used the solution with the parameters $a = 0.263$ and $b = 0.2$ as an initial guess and then lowered the parameter a using 10 nonuniform steps.

[35] The semianalytical solution calculated with the Levenberg-Marquardt algorithm in the case of Henry truncation (78 terms) and the case of Segol truncation (138 terms) are shown in Figure 4. For both calculations, the initial solution for the Levenberg-Marquardt algorithm was set to zero.

[36] Figure 4 shows that the truncation of Henry (78 terms) is not sufficient to obtain accurate results. The Simpson truncation (203 terms) gives the same results (not plotted in Figure 4) than the Segol truncation (138 terms). Indeed, *Simpson and Clement* [2004] used the same expansion for the concentration (100 terms) than *Segol* [1994]. This confirms the observation of *Segol* [1994] who stated that the system is much less sensitive to the number of coefficients for the expansion of the stream function A_{gh} than the number of coefficients for the expansion of the concentration B_{gh}. As in the previous case, the 38 coefficients proposed by Henry and Segol for the expansion of the stream function are adequate. Comparison with numerical solution shows a very good agreement with numerical results. Note that the steady state position of the 0.25 isochlor

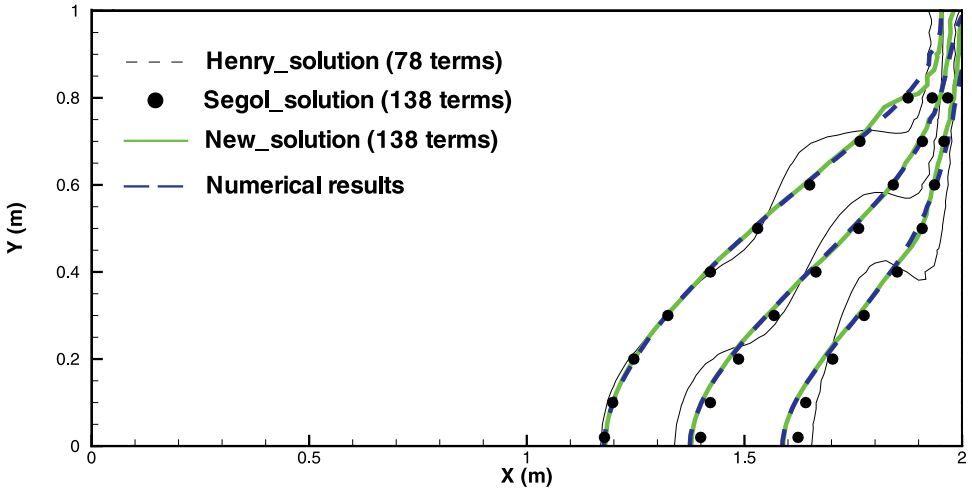

Figure 3. Comparison of numerical and semianalytical results for the standard Henry problem with $a = 0.263$, $b = 0.1$, and $\xi = 2.0$. The semianalytical solution is calculated using the Henry truncation (78 terms) and the Segol truncation (138 terms).

is obtained after around 350 min whereas for the previous case it was around 150 min (Figure 2).

[37] Figure 4 presents also the numerical results of the uncoupled flow model where the solute transport acts as a tracer. In this case, the solute intrusion is due to boundary forcing. Indeed, the right hand side boundary condition corresponds to hydrostatic pressure with heavier saline water. This induces solute intrusion even in the case of uncoupled flow where the solute acts as a tracer inside the domain (for more details see *Simpson and Clement* [2004]).

4.3. Case 3: The Modified Henry Problem With $a = 0.1315$, $b = 0.1$, and $\xi = 2.0$

[38] This test case is obtained from the modified Henry problem of *Simpson and Clement* [2004] and by lowering the dispersion coefficient by half (Table 1). This increases the density-dependent effects compared to boundary forcing. Figure 5 shows that the semianalytical isochlors move inland significantly farther then the uncoupled numerical isochlors. Therefore, this case is more sensitive to density-dependent effects than the *Simpson and Clement* [2004] test case. A very good agreement is observed between semianalytical and numerical results, except the unphysical oscillations (local over- and undershoots) observed in the 0.25 semianalytical isochlor at the upper right corner of the domain (Figure 5). Note that these unphysical oscillations, due to truncation of the Fourier series, remain in the solution with the Simpson and Clement truncation of 203 terms. Therefore, a new truncation is performed by using 424 terms of the Fourier series with 214 terms $(A_{1\ldots7,0\ldots30})$ for the expansion of the stream function and 210 terms $(B_{0\ldots6,1\ldots30})$ for the expansion of the concentration. The results of this new truncation avoid the unphysical oscillations at the right top corner of the domain, although the position of the isochlors does not change. Note that the new truncation requires significantly more computational time (around 5 days) than the Segol truncation (around 10 h).

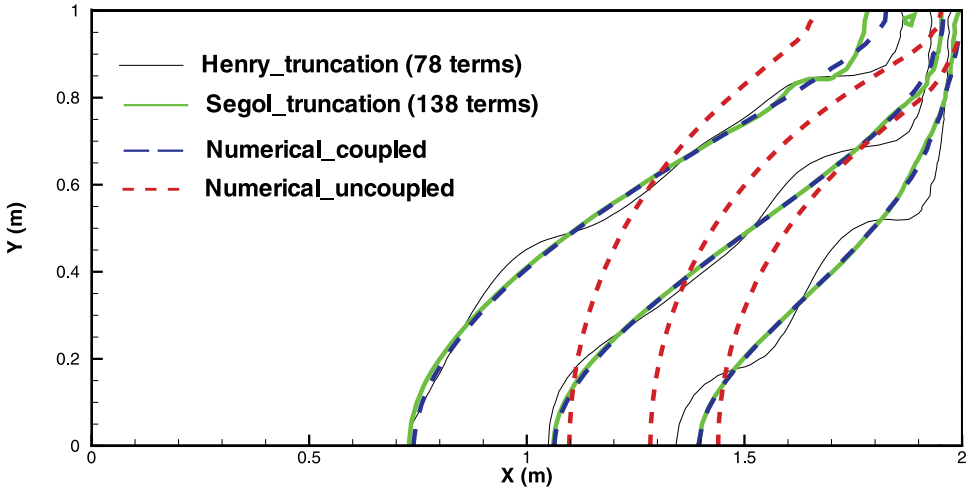

Figure 4. Comparison of numerical and semianalytical results for the modified Henry problem with $a = 0.1315$, $b = 0.2$, and $\xi = 2.0$. The semianalytical solution is calculated using the Henry truncation (78 terms) and the Segol truncation (138 terms). The uncoupled numerical isochlors are also shown.

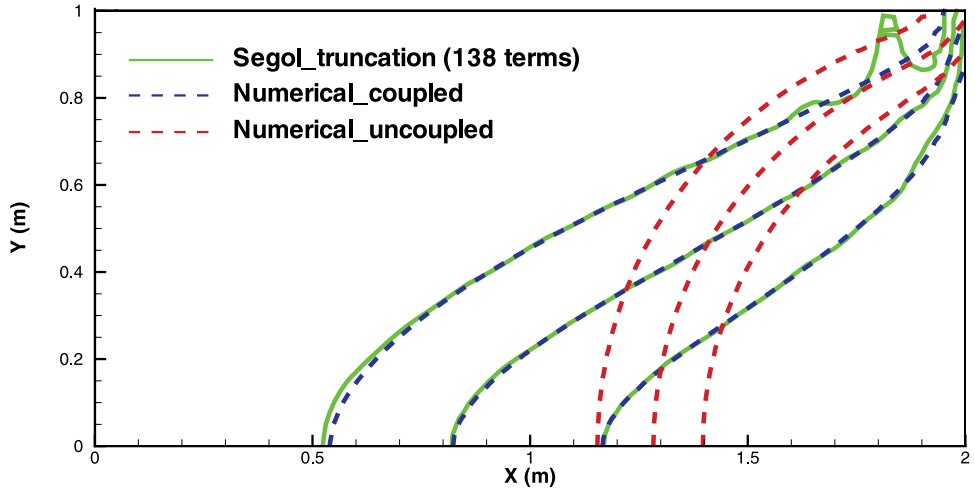

Figure 5. Comparison of numerical and semianalytical results for the modified Henry problem with $a = 0.1315$, $b = 0.1$ and $\xi = 2.0$. The semianalytical solution is calculated using the Segol truncation (138 terms). The uncoupled numerical isochlors are also shown.

On the other hand, the numerical simulation with the DASPK numerical code requires less than 3 min of CPU time.

[39] Finally, as shown in Table 1, this test case ($a = 0.1315$ and $b = 0.1$) can also be obtained using the initial freshwater recharge (instead of the halved one), the initial dispersion coefficient (6.610^{-6} m^2 s^{-1}) and a salt water density of $\rho = 1050$ kg m^{-3} (instead of $\rho = 1025$ kg m^{-3}). A new numerical simulation is performed with these values. The obtained isochlors are in excellent agreement with the semianalytical solution. This shows the validity of the Boussinesq approximation for the Henry problem even for a salt-water density of $\rho = 1050$ kg m^{-3}. Indeed, the Boussinesq approximation is used in the semianalytical calculation but not in the numerical calculation and both give the same results.

4.4. Case 4: The Modified Henry Problem With $a = 0.263$, $b = 0.04$, and $\xi = 2.0$

[40] As stated by *Voss and Souza* [1987], *Kolditz et al.* [1998], and *Abarca et al.* [2007], the major drawback of the Henry problem arises from the high dispersion value used by Henry to obtain the semianalytical solution. Therefore the last three test cases are devoted to the semianalytical solution with a strong reduction of the dispersion coefficient which implies strong reduction of the parameter b.

[41] The results for $a = 0.263$, $b = 0.04$ and $\xi = 2.0$ presented in Figure 6 show a reduced transition zone and a significant difference between coupled and uncoupled results. This makes this test case suitable for testing seawater intrusion codes. The semianalytical solution obtained with the Segol truncation (138 terms) is in very good agreement with the coupled numerical solution. Note, however, that small unphysical oscillations appear in the right and left corners at the top of the domain. These unphysical oscillations remain with the Simpson and Clement truncation (203 terms). As previously mentioned, the results of the new truncation with 424 terms show that the unphysical oscillations at the top of the domain are completely avoided, although the position of the isochlors does not change.

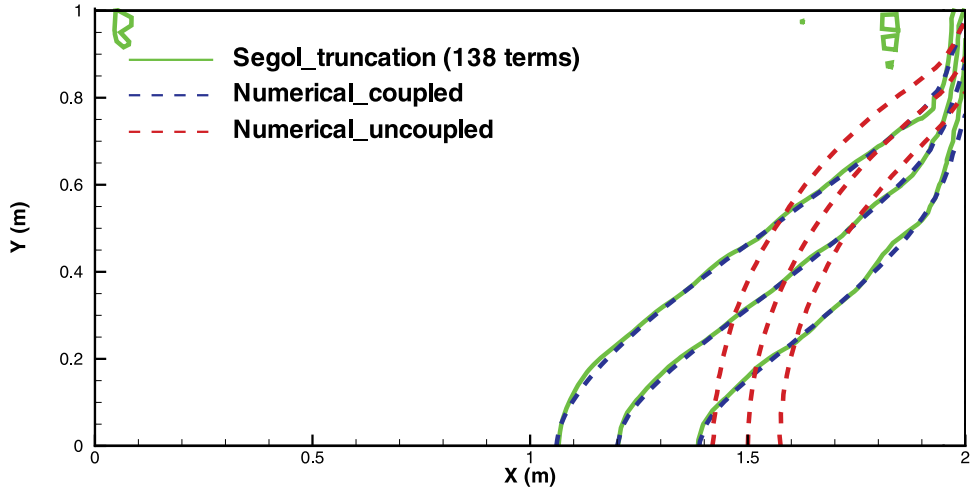

Figure 6. Comparison of numerical and semianalytical results for the modified Henry problem with $a = 0.263$, $b = 0.04$, and $\xi = 2.0$. The semianalytical solution is calculated using the Segol truncation (138 terms). The uncoupled numerical isochlors are also shown.

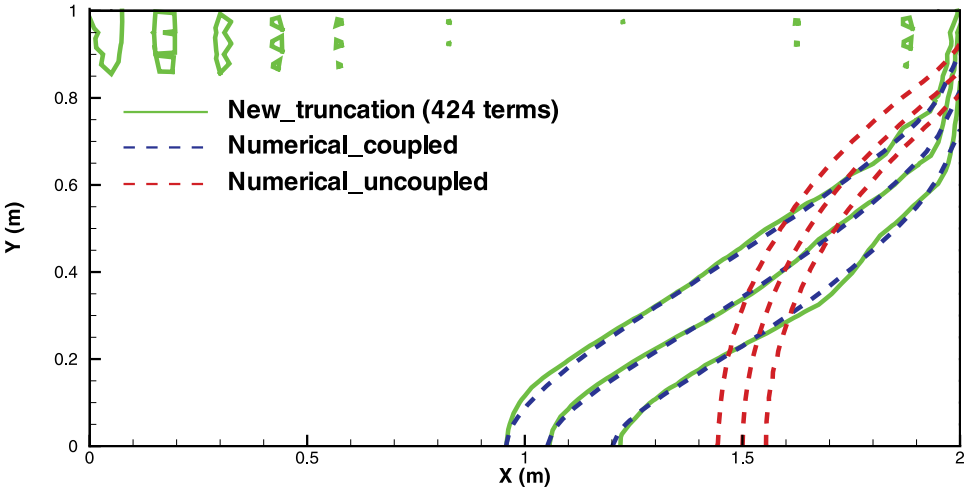

Figure 7. Comparison of numerical and semianalytical results for the modified Henry problem with $a = 0.263$, $b = 0.02$, and $\xi = 2.0$. The semianalytical solution is calculated using the new truncation (424 terms). The uncoupled numerical isochlors are also shown.

4.5. Case 5: The Modified Henry Problem With $a = 0.263$, $b = 0.02$, and $\xi = 2.0$

[42] In this test case, we lowered the dispersion by half compared to the previous case. The truncations proposed by Segol (138 terms) and Simpson and Clement (203 terms) are not sufficient to obtain a stable solution in this case. Both truncations lead to significant unphysical oscillations not only in the top of the domain but also in the isochlors curves. The results of the new truncation (424 terms) are compared to the numerical solution in Figure 7. Despite the unphysical oscillations observed at the top of the domain, a good agreement is observed between the semianalytical and the numerical isochlors. These unphysical oscillations could be avoided if one uses a truncation with much more coefficients. This requires very long computational time (several weeks) and as previously this will have no significant effects on the three isochlors positions. The results of Figure 7 show a very narrow transition zone due the low dispersion coefficient, thus, saltwater invades more the domain than the previous case. Coupled and uncoupled numerical results are significantly different (Figure 7) which reflects the importance of the density-dependent effects compared to boundary forcing.

4.6. Case 6a: The Modified Henry Problem With $a = 0.1315$, $b = 0.04$, and $\xi = 2.0$

[43] This case has a small dispersion and a freshwater recharge reduced by half as suggested by *Simpson and Clement* [2004]. As mentioned before, the solutions obtained using the Segol (138 terms) and Simpson and Clement (203 terms) truncations are not accurate and lead to significant unphysical oscillations not only at top of the domain but also in the isochlor curves. Figure 8 shows that the new truncation (424 terms) gives a stable solution which is in good agreement with the numerical results except in the lower left corner of the domain where the

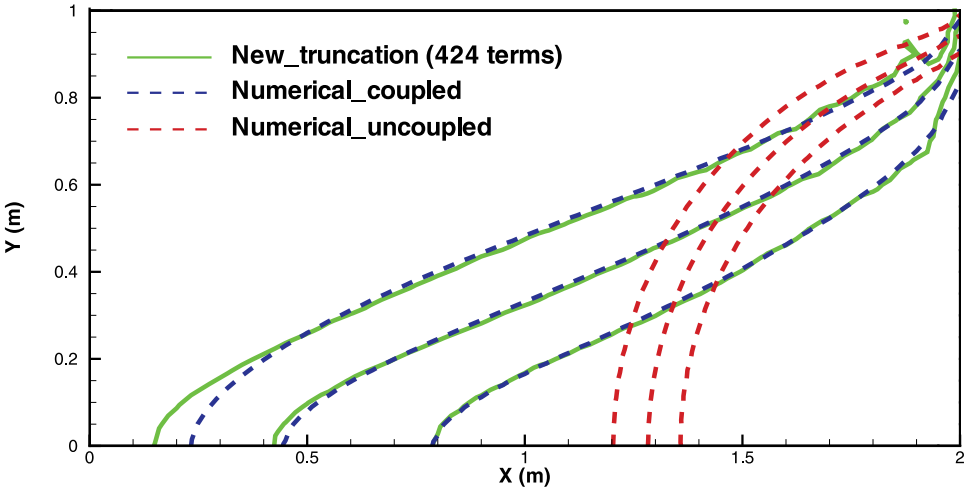

Figure 8. Comparison of numerical and semianalytical results for the modified Henry problem with $a = 0.1315$, $b = 0.04$, and $\xi = 2.0$. The semianalytical solution is calculated using the new truncation (424 terms). The uncoupled numerical isochlors are also shown.

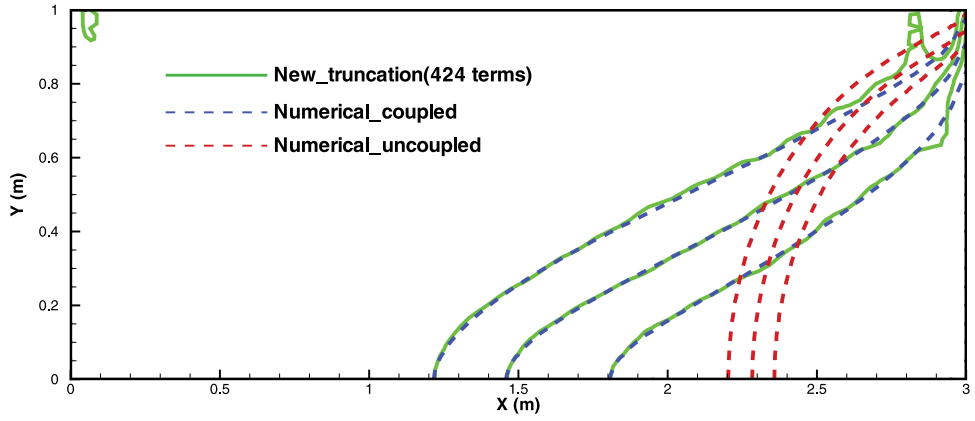

Figure 9. Comparison of numerical and semianalytical results for the modified Henry problem with $a = 0.1315$, $b = 0.04$, and $\xi = 3.0$. The semianalytical solution is calculated using the new truncation (424 terms). The uncoupled numerical isochlors are also shown.

semianalytical 0.25 isochlor is slightly more advanced than the numerical one. This discrepancy is observed because the semianalytical 0.25 isochlor is very close to the inland boundary with zero concentration. Note that the 0.5 and 0.75 isochlors are well reproduced by the numerical code.

4.7. Case 6b: The Modified Henry Problem With $a = 0.1315$, $b = 0.04$, and $\xi = 3.0$

[44] To reduce the influence of the zero-concentration Dirichlet left boundary condition on the 0.25 isochlor for the previous case, a new semi analytical solution is performed on a larger rectangular domain with an aspect ration $\xi = L/d = 3$. The obtained semianalytical results are in very good agreement with the numerical solution as shown in Figure 9. Note that in this case, the steady state position of the isochors is reached within 500 min. In Figure 9, the saltwater intrudes much more in the domain than all previous cases. Large differences can be observed between coupled and uncoupled results. Therefore, this test case is the most sensitive one upon all the previous to density-dependent effects and should be preferred for benchmarking density driven flow codes.

5. Conclusions

[45] The Henry saltwater intrusion problem is considered as one of the most popular test cases of density-dependent groundwater flow models, since *Henry* [1964] provided a semianalytical solution of the problem by expanding the stream function and the salt concentration in double Fourier series. These series are truncated at a given order and the remaining coefficients are calculated by solving a highly nonlinear system of algebraic equations. *Henry* [1964] used a truncation of 78 terms, *Segol* [1994] used a truncation of 138 terms and *Simpson and Clement* [2004] used a truncation of 203 terms. These authors solved the nonlinear system as a system of linear equations treating the nonlinear right hand side as a known quantity, updated iteratively until convergence. This procedure encountered substantial convergence difficulties especially for reduced dispersion values. Consequently, all published works succeeded to develop semianalytical solutions only when an unrealistically large amount of dispersion is introduced in the solution.

[46] In this work, this deficiency of the Henry problem was avoided by using the Levenberg-Marquardt algorithm, which has a quadratic rate of convergence, to calculate the coefficients of the Fourier series. Different truncations are studied and a new truncation based on 424 terms is proposed to develop the semianalytical solutions of the Henry problem with reduced dispersion coefficients.

[47] The obtained semianalytical solutions are in a very good agreement with the numerical results obtained using the method of lines and advanced spatial discretization schemes. These solutions improve the applicability of the semianalytical solution of the Henry problem to saltwater intrusion problems with reduced diffusion and are therefore more suitable to benchmark density-driven flow codes.

Appendix A

[48] The non linear algebraic equations are as follows:

$$\varepsilon_2 a\pi^2 A_{g,h}\left(g^2+\frac{h^2}{\xi^2}\right)\xi = \sum_{r=0}^{\infty} B_{r,h} hN(g,r) + \frac{4}{\pi}W(g,h),$$

$$\varepsilon_1 b\pi^2 B_{g,h}\left(g^2+\frac{h^2}{\xi^2}\right)\xi = \sum_{n=0}^{\infty} A_{g,n} gN(h,n) + \varepsilon_1\sum_{s=1}^{\infty} B_{g,s} SN(h,s) + Quad + \frac{4}{\pi}W(h,g),$$

where

$$\varepsilon_1 = \begin{cases} 2, & if: g = 0 \\ 1, & if: g \neq 0 \end{cases},$$

$$\varepsilon_2 = \begin{cases} 2, & if: h = 0 \\ 1, & if: h \neq 0 \end{cases},$$

$$N(h,n) = \frac{(-1)^{h+n}-1}{h+n} + \frac{(-1)^{h-n}-1}{h-n},$$

$$W(h,g) = \begin{cases} \dfrac{(-1)^h - 1}{h}, & if : g = 0 \\ 0, & if : g \neq 0 \end{cases},$$

$$Quad = \frac{\pi}{4} \sum_{m=1}^{\infty} \sum_{n=0}^{\infty} \sum_{r=0}^{\infty} \sum_{s=1}^{\infty} A_{m,n} B_{r,s} (msLR - nrFG),$$

with

$$F = \delta_{(m-r),g} + \delta_{(r-m),g} - \delta_{(m+r),g},$$

$$L = \delta_{(m-r),g} + \delta_{(r-m),g} + \delta_{(m+r),g},$$

$$G = \frac{(-1)^{h+n-s} - 1}{h+n-s} + \frac{(-1)^{h-n+s} - 1}{h-n+s} - \frac{(-1)^{h+n+s} - 1}{h+n+s} - \frac{(-1)^{h-n-s} - 1}{h-n-s},$$

$$R = \frac{(-1)^{h+n-s} - 1}{h+n-s} + \frac{(-1)^{h-n+s} - 1}{h-n+s} + \frac{(-1)^{h+n+s} - 1}{h+n+s} + \frac{(-1)^{h-n-s} - 1}{h-n-s},$$

and $\delta_{i,j}$ is the Kronecker delta such that

$$\delta_{i,j} = \begin{cases} 1, & if : i = j \\ 0, & if : i \neq j \end{cases}.$$

[49] **Acknowledgments.** The authors would like to thank the anonymous reviewers for their valuable comments and suggestions to improve the quality of the paper. This study was partially supported by the GnR MoMaS (PACEN/CNRS ANDRA, BRGM CEA EDF IRSN) France. And in part, was made possible by the support of SNF (Swiss National Foundation, grant 200020_125167), whose support is gratefully acknowledged. And a special thanks to Stefan Wiesmeier and Silvia Leupin for their appreciated support.

References

Aavatsmark, I. (2002), An introduction to multipoint flux approximations for quadrilateral grids, *Comput. Geosci.*, *6*, 404–432.

Abarca, E., J. Carrera, X. Sanchez-Vila, and M. Dentz (2007), Anisotropic dispersive Henry problem, *Adv. Water Resour.*, *30*(4), 913–926.

Ackerer, P., and A. Younes (2008), Efficient approximations for the simulation of density driven flow in porous media, *Adv. Water Resour.*, *31*, 15–27.

Ackerer, P., A. Younes, and R. Mose (1999), Modeling variable density flow and solute transport in porous medium: 1. Numerical model and verification, *Transp. Porous Media*, *35*(3), 345–373.

Buès, M., and C. Oltéan (2000), Numerical simulations for saltwater intrusion by the mixed hybrid finite element method and discontinuous finite element method, *Transp. Porous Med.*, *40*(2), 171–200.

Croucher, A. E., and M. J. O'Sullivan (1995), The Henry problem for saltwater intrusion, *Water Resour. Res.*, *31*(7), 1809–1814.

Forbes, L. K. (1988), Surface waves of large amplitude beneath an elastic sheet, Part 2, Galerkin solution, *J. Fluid Mech.*, *188*, 491–508.

Frind, E. O. (1982), Simulation of long-term transient density-dependent transport in groundwater, *Adv. Water Resour.*, *5*, 73–88.

Goswami, R. R., and T. P. Clement (2007), Laboratory-scale investigation of saltwater intrusion dynamics, *Water Resour. Res.*, *43*, W04418, doi:10.1029/2006WR005151.

Henry, H. R. (1964), Effects of dispersion on salt encroachment in coastal aquifers, in *Sea Water in Coastal Aquifers*, edited by H. H. Cooper, U.S. Geol. Surv. Supply Pap., *1613-C*, C71–C84.

Herbert, A. W., C. P. Jackson, and D. A. Lever (1988), Coupled groundwater flow and solute transport with fluid density strongly dependent upon concentration, *Water Resour Res.*, *24*, 1781–1795.

Huyakorn, P. S., P. F. Andersen, J. W. Mercer, and H. O. White Jr. (1987), Saltwater intrusion in aquifers: Development and testing of a three-dimensional finite element model, *Water Resour. Res.*, *23*, 293–312.

Kolditz, O., R. Ratke, H. J. G. Diersch, and W. Zielke (1998), Coupled groundwater flow and transport: 1. Verification of variable density flow and transport models, *Adv. Water Res.*, *21*, 27–46.

Konz, M., P. Ackerer, A. Younes, P. Huggenberger, and E. Zechner (2009), Two-dimensional stable-layered laboratory-scale experiments for testing density-coupled flow models, *Water Resour. Res.*, *45*, W02404, doi:10.1029/2008WR007118.

Levenberg, K. (1944), A method for the solution of certain nonlinear problem in least squares, *Quart. Appl. Math.*, *2*, 164–168.

Marquardt, D. W. (1963), An algorithm for least-squares estimation of nonlinear inequalities, *SIAM J. Appl. Math.*, *11*, 431–441.

Oldenburg, C. M., and K. Pruess (1995), Dispersive transport dynamics in a strongly coupled groundwater-brine flow system, *Water Resour. Res.*, *31*, 289–302.

Park, C. H., and M. M. Aral (2008), Saltwater intrusion hydrodynamics in a tidal aquifer, *J. Hydrol. Eng.*, *9*, 863–872.

Pinder, G. F., and H. H. Cooper Jr. (1970), A numerical technique for calculating the transient position of the saltwater front, *Water Resour. Res.*, *6*(3), 875–882.

Segol, G. (1994), *Classic Groundwater Simulations Proving and Improving Numerical Models*, Prentice-Hall, Old Tappan, N. J.

Segol, G., G. F. Pinder, and W. G. Gray (1975), A Galerkin-finite element technique for calculating the transient position of the saltwater front, *Water Resour. Res.*, *11*(2), 343–347.

Siegel, P., R. Mose, P. Ackerer, and J. Jaffré (1997), Solution of the advection diffusion equation using a combination of discontinuous and mixed finite elements, *Int. J. Numer. Methods Fluids*, *24*, 595–613.

Simpson, M. J., and T. P. Clement (2003), Theoretical analysis of the worthiness of the Henry and Elder problems as benchmarks of density-dependent groundwater flow models, *Adv. Water Resour.*, *26*, 17–31.

Simpson, M. J., and T. P. Clement (2004), Improving the worthiness of the Henry problem as a benchmark for density-dependent groundwater flow models, *Water Resour. Res.*, *40*, W01504, doi:10.1029/2003WR002199.

Thorenz, C., G. Kosakowski, O. Kolditz, and B. Berkowitz (2002), An experimental and numerical investigation of saltwater movement in coupled saturated–partially saturated systems, *Water Resour. Res.*, *38*(6), 1069, doi:10.1029/2001WR000364.

Voss, C. I., and W. R. Souza (1987), Variably density flow and solute transport simulation of regional aquifers containing a narrow freshwater-saltwater transition zone, *Water Resour. Res.*, *23*(10), 1851–1866.

Yamashita, N., and M. Fukushima (2001), On the rate of convergence of the Levenberg-Marquardt method, *Computing*, *15*, 239–249.

Younes, A., and P. Ackerer (2008), Solving the advection-dispersion equation with discontinuous Galerkin and multipoint flux approximation methods on unstructured meshes, *Int. J. Numer. Methods Fluids*, *58*(6), 687–708.

Younes, A., and V. Fontaine (2008a), Hybrid and multi point formulations of the lowest order mixed methods for Darcy's flow on triangles, *Int. J. Numer. Methods Fluids*, *58*, 1041–1062.

Younes, A., and V. Fontaine (2008b), Efficiency of mixed hybrid finite element and multi point flux approximation methods on quadrangular grids and highly anisotropic media, *Int. J. Numer. Methods Eng.*, *76*(3), 314–336.

Younes, A., M. Fahs, and S. Ahmed (2009), Solving density flow problems with efficient spatial discretizations and higher-order time integration methods, *Adv. Water Resour.*, *32*, 340–352.

Younes, A., P. Ackerer, and F. Delay (2010), Mixed finite element for solving diffusion-type equations, *Rev. Geophys.*, *48*, RG1004, doi:10.1029/2008RG000277.

Zecheter, E., M. Konz, A. Younes, and P. Huggenberger (2011), Effects of tectonic structures, salt solution mining, and density-driven groundwater hydraulics on evaporite dissolution, *Hydrogeol. J.*, *19*, 1323–1334, doi:10.1007/s10040-011-0759-5.

Chapter 4

Semi-analytical and numerical solutions for density driven free flows

Contents

Paper Submitted to Advances in Water Resources Journal

A semi-analytical solution for density driven flow of free fluids

Anis Younes [(1*)], Ali Zidane[(1,2)], Peter Huggenberger[(2)] , Eric Zechner[(2)]

[(1)] Laboratoire d'Hydrologie de Geochimie de Strasbourg, University of Strasbourg, CNRS, UMR 7517
[(2)] Department of Environmental Sciences, University of Basel, Institute of Geology, Switzerland

** Corresponding author: Anis Younes*
e-mail: younes@unistra.fr

Abstract

The Henry semi-analytical solution for salt water intrusion into costal aquifers is widely used for benchmarking density driven flow in porous media. In this work, we develop a modified Henry semi-analytical solution for density driven flow of free fluids. The new benchmark concerns saltwater intrusion trough a channel where Stokes flow is coupled to mass transport via buoyancy forces. The semi-analytical solution is calculated by replacing the stream function and the concentration by a double set of Fourier series, truncated at a given order. The remaining coefficients are calculated using the Levenberg-Marquardt algorithm to solve the obtained highly nonlinear system of algebraic equations. The semi-analytical solution is validated against the results of a transient numerical code based on the nonconforming Crouzeix-Raviart (CR) finite element approximation for the Stokes flow and a combination of Discontinuous Galerkin (DG) and Multi-Point Flux Approximation (MPFA) methods for the mass transport equation.

Keywords: Density driven flow, free fluids, Analytical solution, Crouzeix-Raviart, Discontinuous Galerkin, MPFA

1. INTRODUCTION

The existence of semi-analytical solutions for nonlinear transport problems is well suited for the validation of numerical codes before their use on real cases. In this sense, the synthetic Henry saltwater intrusion problem [1] is one of the most widely used tests for the verification of density driven flow codes in porous media. Indeed, the semi-analytical solution of Henry [1] provides the steady state isochlors positions by expanding the salt concentration and the stream function in double Fourier series. Henry [1] used 78 terms in these series and calculated the coefficients using a Gauss elimination procedure. In 1994, Segol [2] revaluated the semi-analytical solution by using a new truncation with 138 terms. A good agreement was generally observed between this solution and numerical results [e.g. 3-8]. Effects of dispersion and anisotropy on the Henry problem have been studied numerically in [9]. Recently, a new semi-analytical solution was developed for the Henry problem in the case of small dispersion using a truncation based on 424 terms in the Fourier series [10].

In this work, we extend the Henry problem to free fluids domains and we develop a semi-analytical solution for saltwater intrusion trough a channel (or a single fracture). To this aim, we consider a synthetic problem describing the steady state saltwater intrusion through the channel. Freshwater enters an idealized rectangular domain (Fig. 1) with a constant flux rate from the left boundary. A hydrostatic pressure is prescribed along the right boundary with a denser salt-water solution. The top and the bottom of the domain are impermeable boundaries. The saltwater intrudes from the right until an equilibrium with the injected freshwater is reached. The free-flow is governed by the Stokes equation [11-17] since the flow through the channel is considered steady and laminar and the inertial forces in the flow field are assumed to be negligibly small compared with the viscous and pressure forces. As with the standard Henry problem [1], we develop the semi-analytical solution by expanding the concentration and the stream function in a double set of Fourier series. Two test problems are studied corresponding to different density contrasts. The Fourier series are evaluated using the truncation proposed in [10] based 424 coefficients. These coefficients are calculated by solving a highly nonlinear system of algebraic equations with the Levenberg-Marquardt algorithm, which has a quadratic rate of convergence.

The semi-analytical solution is then compared against numerical results obtained using a robust transient numerical code based on advanced numerical methods. Hence, the Stokes flow is discretized using the Crouzeix-Raviart (CR) approximation, based on the nonconforming

piecewise linear finite elements for the velocity and the piecewise constant finite elements for the pressure. This approximation provides locally mass conservative velocity which is an essential property for mass transport to avoid artificial mass sources and sinks.

For the transport equation, the Discontinuous Galerkin (DG) method is used to discretize the advection equation and combined with the symmetric Multipoint Flux Approximation (MPFA) method for the discretization of the diffusion equation [18]. The DG method is a robust and accurate numerical scheme for problems involving sharp fronts [19]. On the other hand, the MPFA method is locally conservative and handles general irregular grids [20-22]. The MPFA and the DG discretizations can be gathered into one system matrix without operator splitting [18]. To reduce the computational cost of simulations, flow and transport equations are solved sequentially using a non-iterative scheme with proper time management based on local truncation error control as in [23].

2. MATHEMATICAL MODELS

Single-phase steady incompressible flow is governed by the Navier-Stokes equation:

$$\rho\left(\boldsymbol{u}.\nabla\right)\boldsymbol{u}+\nabla p-\mu\nabla^{2}\boldsymbol{u}=\rho\boldsymbol{g} \tag{1}$$

and the continuity equation:

$$\nabla.\boldsymbol{u}=0 \tag{2}$$

where ρ is the fluid density, $\boldsymbol{u}$ is the velocity vector, p is the pressure, $\boldsymbol{g}$ is gravity, and μ is the dynamic viscosity.

In this work, we assume that the flow is sufficiently slow to consider the inertial forces in the flow field (the first nonlinear term in equation (1)) negligibly small compared with the viscous and pressure forces. Therefore, the free-flow simplifies to the following Stokes equations [24-26]:

$$\nabla p-\mu\nabla^{2}\boldsymbol{u}=\rho\boldsymbol{g} \tag{3}$$

$$\nabla.\boldsymbol{u}=0 \tag{4}$$

Three kinds of boundary conditions are used with this system:

- The velocity $\boldsymbol{u}$ is prescribed on the boundary;
- Free outflow boundary condition $\mu\left(\nabla\boldsymbol{u}\right)\boldsymbol{\eta}-p\boldsymbol{\eta}=0$ with $\boldsymbol{\eta}$ the outward normal vector to the boundary;

- The pressure p is prescribed at the boundary. Note that in this case, we set also the velocity components in the tangential direction to zero on the same boundary as used in [27-31]. This condition is named Normal Flow/Pressure or straight-out boundary condition.

Solute transport in the free-fluid region can be described by the following convection-diffusion equation:

$$\frac{\partial C}{\partial t} + \boldsymbol{u}.\nabla C = D\nabla^2 C \tag{5}$$

where C is the solute mass fraction and D is the molecular diffusion coefficient.

Flow and transport equations are coupled by the linear state equation linking density to mass fraction:

$$\rho = \rho_0 + (\rho_1 - \rho_0)C \tag{6}$$

where ρ_1 and ρ_0 are respectively saltwater and freshwater density.

The boundary conditions for the transport equation are of Dirichlet type (C is fixed) or Neumann type ($\partial C/\partial \boldsymbol{\eta} = 0$ where $\boldsymbol{\eta}$ is the direction normal to the boundary).

3. THE SEMI-ANALYTICAL SOLUTION

The synthetic problem is adapted from the saltwater intrusion problem of Henry [1], by replacing the confined aquifer (porous medium where the flow is governed by Darcy equation) by a channel (free-flow region where flow is governed by Stokes equation). The developments to obtain the semi-analytical solution are summarized in this section.

The Stokes equations (3)-(4) are written in the following form:

$$\begin{cases} -\dfrac{\partial P}{\partial x} + \mu\left(\dfrac{\partial^2 u}{\partial x^2} + \dfrac{\partial^2 u}{\partial z^2}\right) = 0 \\ -\dfrac{\partial P}{\partial z} + \mu\left(\dfrac{\partial^2 v}{\partial x^2} + \dfrac{\partial^2 v}{\partial z^2}\right) = f \\ \dfrac{\partial u}{\partial x} + \dfrac{\partial v}{\partial z} = 0 \end{cases} \tag{7}$$

where the body forces f can be written using (6) as,

$$f = [\rho_0 + (\rho_1 - \rho_0)C]g \tag{8}$$

The last equation in (7) implies the existence of a stream function ϕ, such as:

$$u = \frac{\partial \phi}{\partial z} \text{ and } v = -\frac{\partial \phi}{\partial x} \tag{9}$$

Inserting (9) into (7) leads to:

$$\mu\left[\frac{\partial^4 \phi}{\partial x^4} + 2\frac{\partial^4 \phi}{\partial x^2 \partial z^2} + \frac{\partial^4 \phi}{\partial z^4}\right] = -(\rho_1 - \rho_0) g \frac{\partial C}{\partial z} \tag{10}$$

As in [1, 2], we define the following new variables:

$$x' = x/d\ ,\ z' = z/d\ ,\ u' = u\,d/Q\ ,\ v' = v\,d/Q\ ,\ u' = \partial\psi'/\partial z'\ ,\ v' = -\partial\psi'/\partial x'\ ,\ \psi = \psi' - z' \tag{11}$$

where x' and z' are non-dimensional coordinates, u' and v' are the non-dimensional velocities and ψ' the non-dimensional stream function.

Using (11), eq (10) leads to:

$$a\left(\frac{\partial^4 \psi}{\partial x^4} + 2\frac{\partial^4 \psi}{\partial x^2 \partial z^2} + \frac{\partial^4 \psi}{\partial z^4}\right) = -\left(\frac{\partial C}{\partial x} + \frac{1}{\xi}\right) \tag{12}$$

with $a = \dfrac{\mu Q}{(\rho_1 - \rho_0) g d^3}$ and $\xi = \dfrac{L}{d}$ the aspect ratio of the domain, where L is the length and d is the depth of the domain.

Similarly, the change of variables applied to the mass transport equation (5) (see [1, 2] for details) leads to:

$$b\left(\frac{\partial^2 C}{\partial x^2} + \frac{\partial^2 C}{\partial z^2}\right) = \frac{\partial \psi}{\partial z}\frac{\partial C}{\partial x} - \frac{\partial \psi}{\partial x}\frac{\partial C}{\partial z} + \frac{1}{\xi}\frac{\partial \psi}{\partial z} + \frac{\partial C}{\partial x} + \frac{1}{\xi} \tag{13}$$

with $b = \dfrac{D}{Q}$ and C is now the non-dimensional concentration.

The stream function and the concentration are represented by double Fourier series of the form:

$$\psi = \sum_{m=1}^{\infty}\sum_{n=0}^{\infty} A_{m,n} \sin(m\pi z)\cos(n\pi \frac{x}{\xi}) \tag{14}$$

$$C = \sum_{r=0}^{\infty}\sum_{s=1}^{\infty} B_{r,s} \cos(r\pi z)\sin(s\pi \frac{x}{\xi}) \tag{15}$$

Substituting these relations into equations (12) and (13), multiplying equation (12) by $4\sin(g\pi z)\cos(h\pi\frac{x}{\xi})$ and equation (13) by $4\cos(g\pi z)\sin(h\pi\frac{x}{\xi})$, and integrating over the rectangular domain gives an infinite set of algebraic equations for $A_{g,h}$ and $B_{g,h}$ namely,

$$\varepsilon_2 a\pi^4 A_{g,h}(g^2+\frac{h^2}{\xi^2})^2\xi=\sum_{r=0}^{\infty}B_{r,h}hN(g,r)+\frac{4}{\pi}W(g,h) \tag{16}$$

$$\varepsilon_1 b\pi^2 B_{g,h}(g^2+\frac{h^2}{\xi^2})\xi=\sum_{n=0}^{\infty}A_{g,n}gN(h,n)+\varepsilon_1\sum_{s=1}^{\infty}B_{g,s}SN(h,s)+Quad+\frac{4}{\pi}W(h,g) \tag{17}$$

Details about the parameters $\varepsilon_1,\varepsilon_2,N,W,Quad$, can be found in Appendix A.

The algebraic system of equations (16)-(17) has the same form than the system obtained by Henry [1] and Segol [2] for the standard saltwater intrusion through a coastal aquifer. Note that the flow equation (16) is different from the one obtained with the Darcy flow in [1].

Henry [1], Segol [2] and Simpson and Clement [32] used different truncations of the Fourier series. They solved the nonlinear system as a system of linear equations where the expansion coefficients are considered as unknowns. The nonlinear right hand side is treated as a known quantity, updated iteratively until convergence. As stated by Segol [2], this technique encountered substantial convergence difficulties for small values of the parameters a and b which for the standard Henry problem correspond to $a_{Darcy}=\frac{Q\rho_0}{K(\rho_1-\rho_0)d}$ (K is the hydraulic conductivity of the porous medium) and $b_{Darcy}=\frac{D}{Q}$.

To avoid convergence difficulties in the case of saltwater intrusion within a channel, we use in this work the Levenberg-Marquardt algorithm [33, 34], which has a quadratic rate of convergence, to solve the set of nonlinear algebraic equations (16) - (17) [35]. The method is considered as one of the most efficient algorithm for solving systems of nonlinear equations. The nonlinear algebraic system of equations (16)-(17) is written in the form $F(\boldsymbol{X})=0$ where $\boldsymbol{X}$ is a vector formed by the coefficients $A_{g,h}$ and $B_{g,h}$ to calculate. The Levenberg-Marquardt algorithm includes two minimization methods: the gradient descent method and the Gauss-Newton method. Far from the optimum, the Levenberg-Marquardt method behaves like a gradient descent method,

whereas, it acts like the Gauss Newton method nearby the optimum. The Jacobian $\boldsymbol{J}$ is approximated numerically using finite differences.

Two test problems, corresponding to different density contrast, are studied in this work. The Fourier series are truncated using 424 coefficients as in [10] with 214 terms $\left(A_{1..7,0..30}\right)$ for the expansion of the stream function and 210 terms $\left(B_{0..6,1..30}\right)$ for the expansion of the concentration.

4. THE NUMERICAL SOLUTION

In this part, we summarize the numerical techniques used for the solution of the coupled stokes flow and mass transport system.

4.1 STOKES FLOW DISCRETIZATION

The flow system (3)-(4) cannot be discretized with the same order for pressure and velocity approximations due to stability conditions. Otherwise some sort of stabilization is added to the mixed formulation [36]. To avoid these difficulties, we use the non-conforming Crouzeix-Raviart (CR) elements for the velocity approximation in combination with constant pressure per element, since they satisfy the Babuska-Brezzi condition [37-39]. This condition is central for ensuring that the final linear system to solve is non-singular [40]. Moreover, the non-conforming Crouzeix-Raviart (CR) finite element method has local mass conservation properties [41] and leads to a relatively small number of unknowns due to the low-order shape functions. The CR elements are used in many problems such as the Darcy-Stokes problem [42], the Stokes problem [43] and the elasticity problem [44, 45]. The CR method gives a simple stable optimal order approximation of the Stokes equations [46]. In the following, we recall the main stages for the discretization of the Stokes equation with the CR triangular elements.

With the non-conforming finite elements method, the degrees of freedom for the velocity vector $\boldsymbol{u}$ are the two component $\left(u_i, v_i\right)$ of $\boldsymbol{u}$ at the midedge i facing the node i. Inside the element E, we assume a linear variation of the velocity components $\left(u_E, v_E\right)$

$$u_E = u_i\varphi_i^E + u_j\varphi_j^E + u_k\varphi_k^E \quad , \quad v_E = v_i\varphi_i^E + v_j\varphi_j^E + v_k\varphi_k^E \tag{18}$$

where the interpolation function φ_i^E equals 1 on the midedge i and zero on the midedges j and k of E (Fig. 2).

The variational formulation of the Stokes equation (3) using the test function φ_i over the domain Ω writes:

$$\int_{\Omega} \nabla.\left(\mu \nabla \boldsymbol{u} - p\boldsymbol{I}\right)\varphi_i = \int_{\Omega} \rho g \nabla z \varphi_i \tag{19}$$

where $\nabla \boldsymbol{u}$ is the gradient of the velocity vector $\boldsymbol{u}$ and $\boldsymbol{I}$ the 2×2 identity matrix.

Using Green's formula, we obtain

$$\int_{\partial\Omega} \varphi_i \left(\mu \nabla \boldsymbol{u} - p\boldsymbol{I}\right)\boldsymbol{\eta}_{\partial\Omega} - \int_{\Omega} \nabla.\left(\mu \nabla \boldsymbol{u} - p\boldsymbol{I}\right)\varphi_i = \int_{\Omega} \rho g \nabla z \varphi_i \tag{20}$$

The first integral contains boundary conditions. It vanishes in case of free-flow boundary or in case of an interior edge i. In this last case, equation (20) becomes

$$-\int_{E} \nabla.\left(\mu \nabla \boldsymbol{u}_E - p_E \boldsymbol{I}\right)\varphi_i^E - \int_{E'} \nabla.\left(\mu \nabla \boldsymbol{u}_{E'} - p_{E'} \boldsymbol{I}\right)\varphi_i^{E'} = \int_{E} \rho g \nabla z \varphi_i^E + \int_{E'} \rho g \nabla z \varphi_i^{E'} \tag{21}$$

Using (18) and (19), we obtain

$$-\int_{E} \nabla.\left(\mu \nabla \boldsymbol{u}_E - p_E \boldsymbol{I}\right)\varphi_i^E = \begin{pmatrix} \Delta z^i \\ \Delta x^i \end{pmatrix} P_E - \frac{\mu}{|E|}\begin{pmatrix} \sum_{j=1}^{3}\left(\Delta x^i \Delta x^j + \Delta z^i \Delta z^j\right)u_j \\ \sum_{j=1}^{3}\left(\Delta x^i \Delta x^j + \Delta z^i \Delta z^j\right)v_j \end{pmatrix} \tag{22}$$

and

$$\int_{E} \rho g \nabla z \varphi_i^E = \rho_E g\left(\overline{z}_i - z_E\right)\begin{pmatrix} \Delta z^i \\ \Delta x^i \end{pmatrix} \tag{23}$$

where $\Delta x^i = x_j - x_k$ and $\Delta z^i = z_k - z_j$, z_E and $\overline{z}_i$ are respectively the z-coordinate of the centre of E and of the midpoint of edge i, ρ_E and p_E are respectively the mean density and pressure over E.

The finite volume formulation of the continuity equation (4) over the element E writes:

$$\int_{E} \nabla.\boldsymbol{u} = 0 \tag{24}$$

using (18), it becomes

$$\sum_{j=1}^{3}\left(\Delta z^j u_j + \Delta x^j v_j\right) = 0 \tag{25}$$

The final system to solve for the flow is obtained by writing equation (21) for each edge (two equations per edge) and equation (25) for each element.

4.2 MASS TRANSPORT DISCRETIZATION

The DG leads to a high-resolution scheme for advection that has been proven to be clearly superior to the already existing finite element methods [47]. In this work, the explicit DG method, where fluxes are upwinded using a Riemann solver, is used to solve the advection equation and combined with the symmetric Multipoint Flux Approximation (MPFA) method for the diffusion equation.

The transport equation (5) is written in the following mixed form

$$\begin{cases} \dfrac{\partial C}{\partial t} + \boldsymbol{u}.\nabla C + \nabla.\left(\boldsymbol{u}_D\right) = 0 \\ \boldsymbol{u}_D = -D\nabla C \end{cases} \tag{26}$$

The dispersive flux $\boldsymbol{u}_D$ is assumed to vary linearly inside the element E, therefore,

$$\nabla.\boldsymbol{u}_D = \frac{1}{|E|}\sum_i Q^E_{D,\partial Ei} \tag{27}$$

where $Q^E_{D,\partial Ei} = \int_{\partial Ei} \boldsymbol{u}_D.\boldsymbol{\eta}_{\partial Ei}$ is the dispersive flux across the edge ∂Ei of E.

We use the $P1$ DG method where the approximate solution $C_h(\boldsymbol{x},t)$ is expressed with linear basis functions ϕ_i^E on each element E as follows:

$$C_h\left(\boldsymbol{x},t\right)|_E = \sum_{i=1}^{3} C_i^E\left(t\right)\phi_i^E\left(\boldsymbol{x}\right) \tag{28}$$

where $C_i^E\left(t\right)$ are the three unknown coefficients corresponding to the degrees of freedom which are the average value of the mass fraction defined at the triangle centroid $\left(\overline{x}_E,\overline{z}_E\right)$ and its deviations in each space direction [48] with the corresponding interpolation functions:

$$\phi_1^E\left(x,z\right)=1,\quad \phi_2^E\left(x,z\right)=x-\overline{x}_E,\ \phi_3^E\left(x,z\right)=z-\overline{z}_E. \tag{29}$$

The variational formulation of (26) over the element E using ϕ_i^E as test functions leads to (see [12] for details),

$$[A]\begin{pmatrix}\frac{dC_1^E}{dt}\\ \frac{dC_2^E}{dt}\\ \frac{dC_3^E}{dt}\end{pmatrix}=[B]\begin{bmatrix}C_1^E\\ C_2^E\\ C_3^E\end{bmatrix}-\left[M^0\right]\begin{bmatrix}C_1^E\\ C_2^E\\ C_3^E\end{bmatrix}-\sum_{\ell=1}^{3}\left[M^\ell\right]\begin{bmatrix}C_1^{E\ell}\\ C_2^{E\ell}\\ C_3^{E\ell}\end{bmatrix}+\begin{bmatrix}\sum_{\partial Ej}Q_{D,j}^E\\ 0\\ 0\end{bmatrix} \tag{30}$$

with,

$$A_{i,j}=\int_E \phi_j^E\phi_i^E \qquad B_{i,j}=\int_E \phi_j^E\,\boldsymbol{u}.\nabla\phi_i^E$$

$$M_{i,j}^0=\sum_{\ell=1}^{N_E}\lambda_{\partial E\ell}^E\frac{Q_{\partial E\ell}^E}{|\partial E\ell|}\int_{\partial E\ell}\phi_i^E\,\phi_j^E, \qquad M_{i,j}^\ell=\left(1-\lambda_{\partial E\ell}^E\right)\frac{Q_{\partial E\ell}^E}{|\partial E\ell|}\int_{\partial E\ell}\phi_i^E\,\phi_j^{E\ell} \quad (\ell=1,..,3)$$

where Ej is the adjacent element to E such that ∂Ej is the common edge of E and Ej and $Q_{\partial E\ell}^E=\int_{\partial E\ell}\boldsymbol{u}.\boldsymbol{\eta}_{\partial Ej}$ the water flux across ∂Ej. The upwind parameter $\lambda_{\partial E\ell}^E$ is defined by

$$\lambda_{\partial Ej}^E=\begin{cases}1 & if \quad \boldsymbol{u}.\boldsymbol{\eta}_{\partial Ej}\geq 0\\ 0 & if \quad \boldsymbol{u}.\boldsymbol{\eta}_{\partial Ej}<0\end{cases} \tag{31}$$

An explicit time discretization is used for the equation (30). An efficient geometric slope limiter is used to avoid unphysical oscillations near sharp fronts [49].

The dispersive fluxes $Q_{D,j}^E$ across edges are approximated using the MPFA method. The basic idea of this method is to divide each triangle into 3 sub-cells as in Fig. 3. Inside the sub-cell (O,F_1,G,F_2) formed by the corner O, the centre G and the midpoint edges F_1 and F_2, we assume linear variation of the mass fraction between C_1^E, TC_1 and TC_2, the mass fractions respectively at G and the two continuity points f_1 and f_2. The symmetry of the MPFA scheme is achieved when the continuity points are localized at $\frac{Of_1}{OF_1}=\frac{Of_2}{OF_2}=\frac{2}{3}$. In this case half-edge fluxes $\left(Q_O^1=\int_O^{F_1}-D\nabla C \text{ and } Q_O^2=\int_O^{F_2}-D\nabla C\right)$, taken positive for outflow write [50]:

$$\begin{pmatrix}Q_O^1\\ Q_O^2\end{pmatrix}=\beta_E\begin{pmatrix}-\overrightarrow{OF_1}.\overrightarrow{OF_1} & \overrightarrow{OF_1}.\overrightarrow{OF_2}\\ \overrightarrow{OF_1}.\overrightarrow{OF_2} & -\overrightarrow{OF_2}.\overrightarrow{OF_2}\end{pmatrix}\begin{pmatrix}TC_1-C_1^E\\ TC_2-C_1^E\end{pmatrix} \tag{32}$$

with $\beta_E=3D/|E|$.

This system is written for all sub-cells sharing the vertex O which create an interaction region. Then by writing continuity of diffusive fluxes across half-edges and by assuming continuity of mass fraction at continuity points, we obtain a local system $[A](TC)=[B](C)$. This local system is solved to obtain the mass fraction at the continuity points (TC_i) as function of mass fraction at all elements sharing the vertex O. The obtained relation is then substituted into (32) to obtain half-edge fluxes explicitly as a weighted sum of the cell mass fraction of the interaction volume. Finally, the summation of these fluxes is written using an implicit time discretization and substituted into the equation (30).

4.3 COUPLING STOKES FLOW AND MASS TRANSPORT

Stokes flow equations (3)-(4) and the advection-diffusion mass transport equation (26) are coupled by the state equation (6) linking density to mass fraction. Due to nonlinearities, simulations can require an excessive computational time and/or heavy equipments. Adaptive temporal discretization based on local truncation error control has been shown to be useful to reduce the computational cost of the simulation [51-58]. In this work, we use the non-iterative time stepping scheme based on local truncation error control developed in [23].

5. VALIDATION OF THE SEMI-ANALYTICAL SOLUTION

We consider a synthetic example $\left(2\times 1\ m^2\right)$ where the domain is discretized with a regular triangular mesh of 3200 elements. The flux at the left (inland) boundary is set to $Q=0.92\,m^2s^{-1}$. To avoid very small values of the parameter a for which we cannot obtain a converged semi-analytical solution, the viscosity is set to $\mu=1$ Pa s in this synthetic problem.

5.1 TEST CASE 1: $a=0.008; b=0.1$

In this test case, we set the freshwater density (at the left boundary) to $\rho_0=1000\,kg\,m^{-3}$, the saltwater density (at the right boundary) to $\rho_1=1011 kg\,m^{-3}$ and the diffusion coefficient to $D=0.092\,m^2s^{-1}$. The corresponding non-dimensional parameters a and b are:

$$a=\frac{\mu Q}{(\rho_1-\rho_0)gd^3}=0.008 \text{ and } b=\frac{D}{Q}=0.1.$$

Table 1 provides the position of the three principal isochlors (0.25, 0.5 and 0.75) obtained with the semi-analytical solution using the truncation suggested in [10]. The transient numerical

simulation is performed until a long time to ensure a steady state solution. The three semi analytical isochlors are then compared against the numerical solution in Fig. 4. A good agreement can be observed between the semi-analytical and the numerical solutions (Fig. 4).

5.2 *TEST CASE 2*: $a = 0.006; b = 0.05$

In this case, the saltwater density is increased to $\rho_1 = 1015\, kg\, m^{-3}$ and the diffusion coefficient is reduced to $D = 0.046\, m^2 s^{-1}$. The corresponding non-dimensional parameters a and b are then:

$$a = \frac{\mu Q}{(\rho_1 - \rho_0) g d^3} = 0.006 \text{ and } b = \frac{D}{Q} = 0.05.$$

The same truncation based 424 coefficients of the Fourier series is used for the semi-analytical solution. The positions of the three principal isochlors (0.25, 0.5, and 0.75) are listed in Table 1. Fig. 5 shows the semi analytical and numerical isochlors. As previously, a good agreement can be observed between the numerical and the semi-analytical solutions.

6. CONCLUSION

In this manuscript, we developed a semi analytical solution for the validation of density driven flow of free fluids. The problem is adapted from the saltwater intrusion problem of Henry [1], by replacing the confined aquifer by a channel. The semi-analytical solution is calculated by replacing the stream function and the concentration by a double set of Fourier series. These series are truncated using 424 terms as in [10]. The remaining coefficients are calculated by solving a highly nonlinear system of algebraic equations using the Levenberg-Marquardt algorithm.

The semi analytical solution is validated using a synthetic problem of saltwater intrusion. Two test cases including different density contrasts are studied. A transient numerical model is developed for coupled Stokes flow and mass transport with large density variations. The model is developed for a general triangular meshes and uses the CR finite elements for the flow discretization, the DG method for advection and the symmetric MPFA method for diffusion. A good agreement is observed between the semi-analytical and numerical solutions fro the two studied test cases. The semi-analytical positions of the three principal isochlors are listed in Table 1 and can then be used for the validation of numerical codes.

ACKNOWLEDGMENTS

This study was supported by the SNF (Swiss National Foundation), whose support is gratefully acknowledged.

Appendix A

$$\varepsilon_2 a\pi^4 A_{g,h}(g^2+\frac{h^2}{\xi^2})^2\xi=\sum_{r=0}^{\infty}B_{r,h}hN(g,r)+\frac{4}{\pi}W(g,h)$$

$$\varepsilon_1 b\pi^2 B_{g,h}(g^2+\frac{h^2}{\xi^2})\xi=\sum_{n=0}^{\infty}A_{g,n}gN(h,n)+\varepsilon_1\sum_{s=1}^{\infty}B_{g,s}SN(h,s)+Quad+\frac{4}{\pi}W(h,g)$$

Where

$$\varepsilon_1=\begin{cases}2, if: g=0\\ 1, if: g\neq 0\end{cases}$$

$$\varepsilon_2=\begin{cases}2, if: h=0\\ 1, if: h\neq 0\end{cases}$$

$$N(h,n)=\frac{(-1)^{h+n}-1}{h+n}+\frac{(-1)^{h-n}-1}{h-n}$$

$$W(h,g)=\begin{cases}\dfrac{(-1)^h-1}{h}, if: g=0\\ 0, \quad if: g\neq 0\end{cases}$$

$$Quad=\frac{\pi}{4}\sum_{m=1}^{\infty}\sum_{n=0}^{\infty}\sum_{r=0}^{\infty}\sum_{s=1}^{\infty}A_{m,n}B_{r,s}(msLR-nrFG)$$

With

$$F=\delta_{(m-r),g}+\delta_{(r-m),g}-\delta_{(m+r),g}$$

$$L=\delta_{(m-r),g}+\delta_{(r-m),g}+\delta_{(m+r),g}$$

$$G=\frac{(-1)^{h+n-s}-1}{h+n-s}+\frac{(-1)^{h-n+s}-1}{h-n+s}-\frac{(-1)^{h+n+s}-1}{h+n+s}-\frac{(-1)^{h-n-s}-1}{h-n-s}$$

$$R=\frac{(-1)^{h+n-s}-1}{h+n-s}+\frac{(-1)^{h-n+s}-1}{h-n+s}+\frac{(-1)^{h+n+s}-1}{h+n+s}+\frac{(-1)^{h-n-s}-1}{h-n-s}$$

And $\delta_{i,j}$ is the Kronecker delta such that

$$\delta_{i,j}=\begin{cases}1, if: i=j\\ 0, if: i\neq j\end{cases}$$

References

[1] Henry HR. Effects of dispersion on salt encroachment in coastal aquifers, in Sea Water in Coastal Aquifers, U.S. Geol. Surv. Supply Pap., 1964,1613-C, 70 – 84.

[2] Segol G. Classic Groundwater Simulations Proving and Improving Numerical Models, Prentice-Hall, Old Tappan, N. J. 1994.

[3] Oldenburg CM, Pruess K. Dispersive transport dynamics in a strongly coupled groundwater-brine flow system. Water Resour Res 1995;31:289–302.

[4] Herbert AW, Jackson CP, Lever DA. Coupled groundwater flow and solute transport with fluid density strongly dependent upon concentration. Water Resour Res 1988;24:1781–95.

[5] Ackerer P, Younes A, and R. Mose. Modeling variable density flow and solute transport in porous medium: 1. Numerical model and verification, Transp. Porous Media, 1999, 35(3), 345–373.

[6] Buès M, Oltéan C. Numerical simulations for saltwater intrusion by the mixed hybrid finite element method and discontinuous finite element method, Transp. Porous Med., 2000 ,40(2), 171–200.

[7] Younes A, Fahs M, Ahmed S. Solving density flow problems with efficient spatial discretizations and higher-order time integration methods, Adv. Water Resour., 2009, 32, 340–352.

[8] Hinkelmann R, Sheta H, Class H and Helmig R. A Comparison of Different Model Concepts for Salt Water Intrusion Processes. In: Stauffer, F., Kinzelbach, W., Kovar, K. & E. Hoehn (eds.): ModelCARE 99: International Conference on Calibration and Reliability in Groundwater Modeling - Coping with uncertainty (20. - 23. September 1999, ETH Zurich, Switzerland). 265. IAHS Redbook, Zürich, Schweiz, 2000, 385-391.

[9] Abarca E, Carrera J, Sanchez-Vila X and Dentz M. Anisotropic dispersive Henry problem, Adv. Water Resour., 2007,30(4),pp.913–926.

[10] Zidane A, Younes A, Huggenberger P, Zechner E. The Henry semi-analytical solution for saltwater intrusion with reduced dispersion, Water Resou Res, 2012, VOL. 48, W06533, doi:10.1029/2011WR011157.

[11] Beavers G, Joseph D. Boundary conditions at a naturally permeable wall, J. Fluid Mech., 1967, 30:197.

[12] Saffman P. On the boundary condition at the surface of a porous medium, Studies Appl. Math. 1971, 50:93.

[13] Sanchez-Palencia E. Non-Homogeneous Media and Vibration Theory, volume 127 of Lecture Notes in Physics 1980, Spring-Verlag, Berlin.

[14] Kaviany M. Principles of Heat Transfer in Porous Media, Mechanical Engineering Series 1999, Springer-Verlag, New York.

[15] Jäger W, Mikelić A. On the interface boundary condition of Beavers, Joseph, and Saffman. SIAM J. Appl. Math 2000. 60:1111.

[16] Jäger W, Mikelić A. Asymptotic analysis of the laminar viscous flow over a porous bed. SIAM J. Sci. Comput., 2001a, 22:2006.

[17] Arbogast T, Lehr HL. Homogenization of a Darcy-Stokes system modeling vuggy porous media. Comput. Geosci. 2006, 10:291.

[18] Younes A, Ackerer P. Solving the advection-dispersion equation with Discontinuous Galerkin and Multipoint Flux Approximation methods on unstructured meshes. Int. J Numer Methods in Fluids. 2008; DOI: 10.1002/fld.1783.

[19] Shuangzhang T, Shahrouz A. A slope limiting procedure in Discontinuous Galerkin finite element method for gasdynamics applications. Int. J Numer Analy Modell 2005;2:163-178.

[20] Aavatsmark I. An introduction to multipoint flux approximations for quadrilateral grids. Comput Geosci, 2002;6:404–432.

[21] Aavatsmark I, Barkve T, Bøe Ø, Mannseth T. Discretization on non-orthogonal, quadrilateral grids for inhomogeneous, anisotropic media. J Comput Phys, 1996;127:2–14.

[22] Wheeler MF, Yotov I. A multipoint flux mixed finite element method. SIAM44 2006;5:2082-2106.

[23] Younes A, Ackerer P. Empirical versus time stepping with embedded error control for density-driven flow in porous media, Water Resour. Res., 2010, 46, W01504, doi:10.1029/2009WR008229

[24] Flekkøy EG, Rage T, Oxaal U, Feder J. Hydrodynamic Irreversibility in Creeping Flow, Phys. Rev,1996, PACS numbers: 47.15.Gf, 02.70.Bf, 02.70.Lq, 47.60.+I, VOLUME 77, NUMBER 20

[25] Happel J, Brenner H. Low Reynolds Number Hydrodynamics (Prentice Hall Inc., Englewood Cliffs, NJ,1965).

[26] Landau LD, Lifshitz EM. Fluid Mechanics (Pergamon Press, New York, 1987), 2nd ed.

[27] Conca C, Murat F, Pironneau O. The Stokes and Navier-Stokes equations with boundary conditions involving the pressure. Jpn J. Math.,1994,20, 263-318.

[28] Conca C, Parés C, Pironneau O, Thiriet M. Navier-Stokes equations with imposed pressure and velocity fluxes. Int. J. Numer. Methods Fluids, 1995, 20(4), 267-287.

[29] Gresho PM, Sani RL. On pressure boundary conditions for the incompressible Navier-Stokes equations. Int. J. Numer. Methods Fluids 7, 1987 ,1111-1145.

[30] Jäger W, Mikelić A. On the roughness-induced effective boundary conditions for an incompressible viscous flow, J. Differ. Equ. 2001b ,170, 96-122.

[31] Lukaszewicz G. On the Navier-Stokes equations in time dependent domains with boundary conditions involving the pressure. J. Math. Sci. Univ. Tokyo 4, 1997 ,529-550.

[32] Simpson MJ, Clement TP. Improving the worthiness of the Henry problem as a benchmark for density-dependent groundwater flow models, Water. Resour. Res., 2004 ,40, W01504, doi: 10.1029/2003WR002199

[33] Levenberg K. A method for the solution of certain nonlinear problem in least squares, Quart. Appl. Math., 1944,2 , 164-168.

[34] Marquardt DW. An algorithm for least-squares estimation of nonlinear inequalities, SIAM J. Appl. Math., 1963 ,11 , 431-441.

[35] Yamashita N, Fukushima M. On the rate of convergence of the Levenberg-Marquardt method. Computing 15, 2001, 239-249.

[36] Li J, Chen Z. A new local stabilized nonconforming finite element method for the Stokes equations, Computing, 2008, 82:157-170, doi 10.1007/s00607-008-0001-z

[37] Brezzi F, Fortin M. Mixed and hybrid finite element methods, Berlin: Springer 1991.

[38] Girault V, Raviart PA. Finite element methods for Navier-Stokes equations, Berlin: Springer 1986.

[39] Gresho PM, Sani RL. Incompressible flow and the finite element method, New York: Wiley; 1998.

[40] Langtangen HP, Mardal K, Winther R. Numerical methods for incompressible viscous flow. Adv. Water Res. 25, 2002, 1125-1146.

[41] Bruman E, Hansbo P. A stabilized nonconforming finite element method for incompressible flow, Comput. Methods App Mech. Eng., 2004 ,vol. 195, num. 23-24, p. 2881-99.

[42] Bruman E, Hansbo P. Stabilized Crouzeix-Raviart element for the Darcy-Stokes problem, Numerical Methods for Partial Differential Equation,2005 ,21(5), 986-997.

[43] Crouzeix M, Raviart P. Conforming and nonconforming finite element methods for solving the stationary Stokes equations. RAIRO Sér. Rouge, 1973 ,7(3), 33-75.

[44] Hansbo P, Larson MG. Discontinuous Galerkin and the Crouzeix-Raviart element: application to elasticity. ESAIM: Math. Model. Numer. Anal. 2003,37(1), 63-72.

[45] Hansbo P, Larson MG. Discontinuous Galerkin methods for incompressible and nearly incompressible elasticity by Nitshe's method. Comput. Methods Appl. Mech. Engrg, 2002 ,191(17-18), 1895-1908.

[46] Arnold DN. On nonconforming linear-constant elements for some variants of the Stokes equations, presenta dal s.c. Franco Brezzi nella seduta del 24-6-93.

[47] Arnold DN, Brezzi F, Cockburn B, Marini LD. Unified analysis of discontinuous Galerkin methods for elliptic problems. SIAM J. Numer. Anal. 2002;5:1749-1779.

[48] Cockburn B, Hou S, Shu CW. TVB Runge Kutta local projection discontinuous Galerkin finite element method for conservative laws III: One dimensional systems, J. Compu.t Phys. 1989;84: 90-113.

[49] Younes A, Fahs M, Ackerer P. An efficient geometric approach to solve the slope limiting problem with the Discontinuous Galerkin method on unstructured triangles, Int. J. Numer. Meth. Biomed. Engng. 2010; 26:1824–1835.

[50] Younes A, Fontaine V. Efficiency of Mixed Hybrid Finite Element and Multi Point Flux Approximation methods on quadrangular grids and highly anisotropic media. Int J for Numer Meth in Engrg, 2008b;DOI: 10.1002/nme.2327.

[51] Diersch HJ. Finite element modelling of recirculation density driven saltwater intrusion processes in groundwater, Adv. Water Resour., 1988, 11, 25–43, doi:10.1016/0309-1708(88)90019-X.

[52] Diersch HJ, Kolditz O. Coupled groundwater flow and transport: 2. Thermohaline and 3D convection systems, Adv. Water Resour., 1998, 21, 401–425, doi:10.1016/S0309-1708(97)00003-1.

[53] Turek S. A comparative study of some time stepping techniques for the incompressible Navier-Stokes equations: From fully implicit nonlinear schemes to semi-implicit projection methods, Int. J. Numer. Methods Fluids, 1996, 22(10), 987–1011, doi:10.1002/(SICI)1097-0363 (19960530) 22:10<987::AID-FLD394>3.0.CO;2-7.

[54] Tocci MD, Kelley CT, Miller CT. Accurate and economical solution of the pressure□head form of Richards' equation by the method of lines, Adv. Water Resour., 1997,20(1), 1–14, doi:10.1016/S0309-1708(96)00008-5

[55] Williams GA, Miller CT. An evaluation of temporally adaptive transformation approaches for solving Richards' equation, Adv. Water Resour., 1999, 22(8), 831–840, doi:10.1016/S0309-1708(98)00048-7

[56] Kavetski D, Binning P, Sloan SW. Adaptive time stepping and error control in a mass conservative numerical solution of the mixed form of Richards equation, Adv. Water Resour., 2001,24(6), 595–605, doi:10.1016/S0309-1708(00)00076-2.

[57] Sloan SW, Abbo AJ. Biot consolidation analysis with automatic time stepping and error control. Part 1: Theory and implementation, Int. J. Numer. Anal. Methods Geomech., 1999, 23, 467–492, doi:10.1002/(SICI) 1096-9853(199905)23:6<467::AID-NAG949>3.0.CO;2-R.

[58] Saaltink MW, Carrera J, Olivella S. Mass balance errors when solving the convective form of the transport equation in transient flow problems, Water Resour. Res., 2004, 40, W05107, doi:10.1029/2003WR002866.

List of figures

List of tables

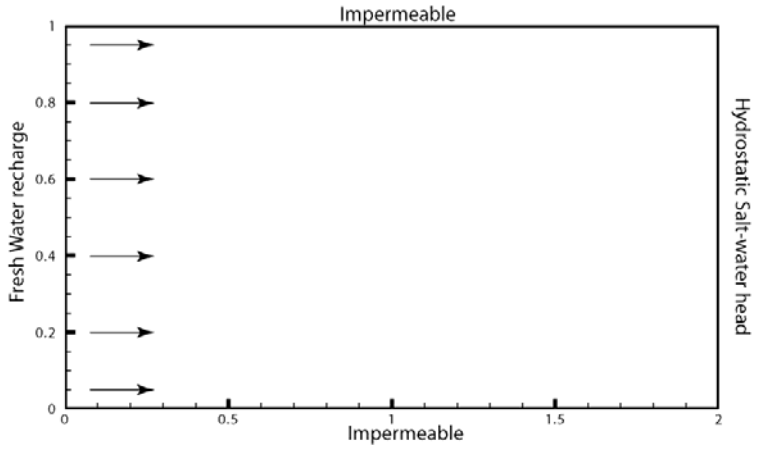

Fig. 1

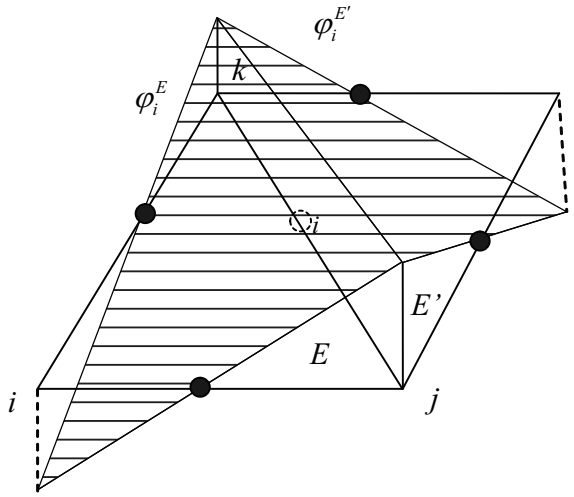

Fig. 2

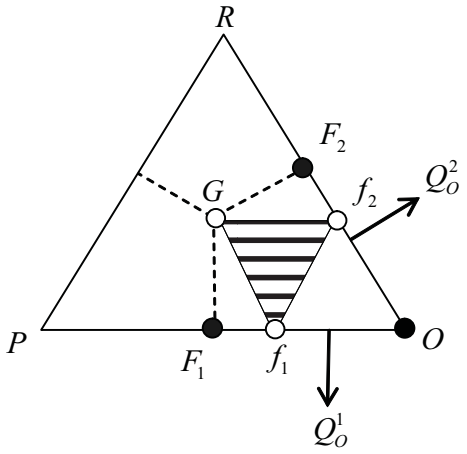

Fig. 3

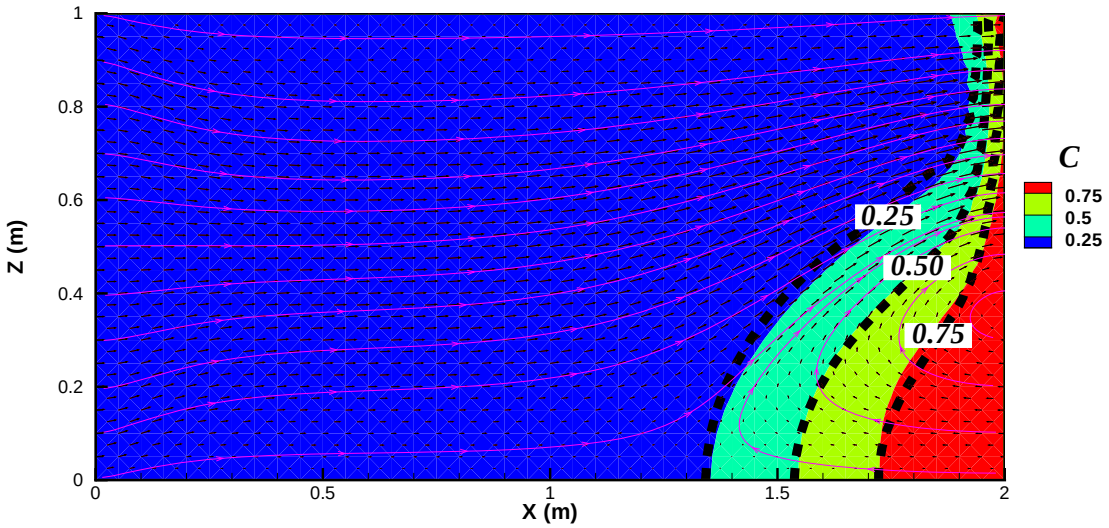

Fig. 4

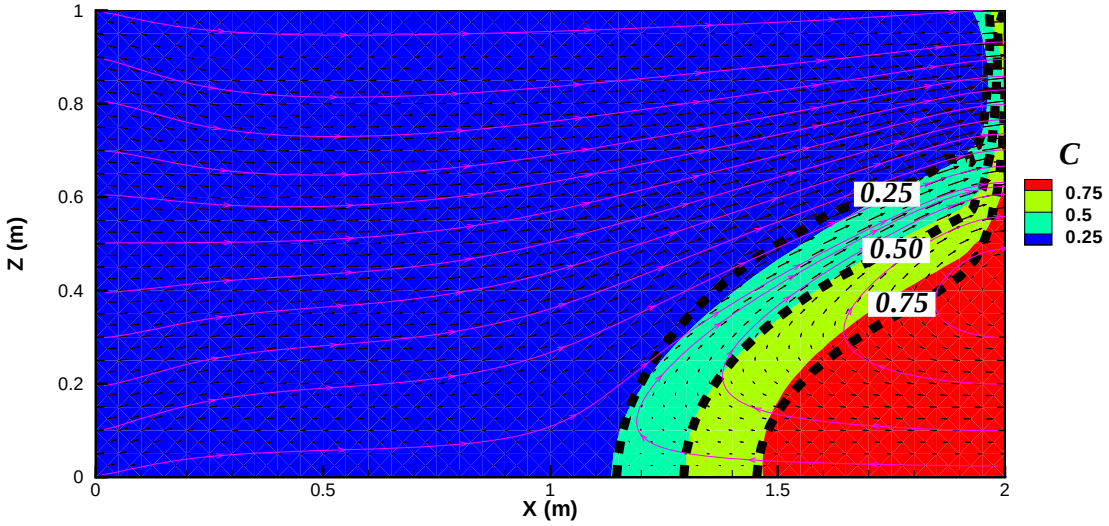

Fig. 5

Case 1 ($a = 0.008$, $b = 0.1$)				**Case 2** ($a = 0.006$, $b = 0.05$)			
z =	**(0.25) x =**	**(0.5) x =**	**(0.75) x =**	**z =**	**(0.25) x =**	**(0.5)x =**	**(0.75) x =**
0.000	1.342	1.540	1.722	0.000	1.146	1.294	1.453
0.050	1.347	1.543	1.728	0.050	1.149	1.297	1.462
0.100	1.353	1.551	1.739	0.100	1.160	1.311	1.479
0.150	1.367	1.568	1.758	0.150	1.174	1.333	1.509
0.200	1.386	1.593	1.784	0.200	1.199	1.364	1.551
0.250	1.409	1.624	1.817	0.250	1.227	1.403	1.604
0.300	1.442	1.663	1.853	0.300	1.263	1.451	1.677
0.350	1.476	1.711	1.881	0.350	1.308	1.509	1.767
0.400	1.521	1.758	1.909	0.400	1.364	1.585	1.853
0.450	1.571	1.809	1.932	0.450	1.431	1.674	1.915
0.500	1.630	1.856	1.946	0.500	1.504	1.789	1.951
0.550	1.705	1.895	1.960	0.550	1.585	1.887	1.971
0.600	1.767	1.921	1.965	0.600	1.700	1.937	1.979
0.650	1.820	1.935	1.971	0.650	1.831	1.954	1.988
0.700	1.887	1.943	1.979	0.700	1.915	1.971	1.991
0.750	1.912	1.951	1.985	0.750	1.951	1.974	1.993
0.800	1.918	1.957	1.985	0.800	1.954	1.977	
0.850	1.929	1.960	1.988	0.850	1.960	1.979	
0.900	1.932	1.965	1.991	0.900	1.960	1.982	
0.950	1.935	1.965	1.991	0.950	1.963	1.982	
1.000	1.932	1.965		1.000	1.968	1.996	

Table 1

Chapter 5

Salt dissolution process

Contents

On the salt dissolution within fractures

Ali Zidane[(1,2)*], Anis Younes [(1)], Constantin Oltéan[(3)] ,Peter Huggenberger[(2)] , Eric Zechner[(2)]

[(1)] Laboratoire d'Hydrologie de Geochimie de Strasbourg, University of Strasbourg, CNRS, UMR 7517, France
[(2)] Department of Environmental Sciences, University of Basel, Institute of Geology, Switzerland
[(3)] Laboratoire d'Environnement de Geochimie et Ouvrages, University of Nancy, France

Paper submitted to "Theoretical and computational fluid dynamics journal".

[*]*Corresponding author*: Ali Zidane
E-mail : ali.zidane@unibas.ch

Abstract

In this study, we investigated both experimentally and numerically the dissolution of a “model fracture”. To take into account the influence of the density effects on the spatial and temporal evolution of the fracture shape, a slow freshwater flux was pumped through a vertical fracture constituted by two salt blocks. The experimental results are subject to numerical analysis. The used numerical model is based on robust numerical approaches. An efficient and advanced approximation for both spatial and temporal discretization is used in order to reduce the high computational needs while maintaining accuracy. The flow equation is solved using the nonconforming Crouzeix-Raviart (CR) finite element approximation for the Stokes equation. For the transport equation, a combination between Discontinuous Galerkin Method and Multipoint Flux Approximation Method is proposed. The numerical effect of the dissolution is considered by using a dynamic mesh variation that increases the size of the mesh based on the amount of the dissolved salt. Similar results are observed between the laboratory experiments and the numerical results, which prove the efficiency of the numerical code to solve density driven flow problems including dissolution.

Keywords: Salt dissolution, Dynamic mesh, CR, DG, MPFA, time control.

1. Introduction

Different geomechanical problems, such as land subsidences and collapses are due to density driven flow in evaporite sedimentary rocks. Salt deposits (*e.g*. rock salt) are common in continental regions [37]. The buried salt layers are dissolved and then removed due to circulation of subsaturated groundwater [44, 22]. Dissolution cavities that occur above or within the impermeable salt deposits lead to subsidences or catastrophic collapses [5, 45, 41, 23]. Moreover, the groundwater salt dissolution affects also the water quality, such as salinization and high mineralization [33]. One of the highest environmental risks as stated by [5] is when radioactive waste repositories are situated in salt rock units which are affected by subsurface dissolution. Different aspects of salt dissolution can occur, as in some cases groundwater can interact with the salt rock from above [33, 45], from the side [42] or from below [5].

In this work, we study the dissolution process of a fractured salt body that is vertically imposed gets in contact with a freshwater source from below and circulating opposite to gravity direction. Highest dissolution values were recorded at the top of the salt layer, whereas dissolution rates reduce gradually until the bottom of the salt body. This type of dissolution aspect is a simplified form of what could be observed in nature. Subvertical fractures are e.g often related to normal fault zones and, if hydraulically active, may accelerate density driven flow and, hence, dissolution of rock salt. One could approximate it as two layers above each other, when one is reactive and the other is impermeable. If there is a fracture that propagates through these layers and freshwater circulates from below as shown in Figures (1a, 1b), then this conical shape could be obtained. In other cases the ceiling is not impermeable; hence a different aspect of the dissolution shape could be observed and solution cavities could be created at the ceiling. In this study, more concern is given to the non-reactive ceiling.

A robust numerical model is developed including some advanced approximations for both spatial and temporal discretization to reduce the computational needs and maintaining accuracy at the same time. The numerical code is used to simulate the density driven flow problem including the dissolution equation. The coupled flow-transport numerical model is based on the Stokes flow equation and the advection dispersion equation. On one hand, flow and transport equations are coupled by the state equations linking density and viscosity variations to mass fraction. On the other hand, both flow and transport are coupled with the dissolution equation by using a dynamic mesh routine, where the size of the finite element modifies with respect to the amount of dissolution that occurs near that element. To achieve high accuracy level for the spatial discretization of flow and transport, we used specifically suited methods. The flow through the fracture is considered steady and laminar and the inertial forces in the flow field are assumed to be negligibly small compared with the viscous and pressure forces. Therefore, the free-flow is governed by the Stokes equation [9, 46, 47, 34, 31, 32]. The Stokes flow is discretized using the Crouzeix-Raviart (CR) approximation, based on the nonconforming piecewise linear finite elements for the velocity and the

piecewise constant finite elements for the pressure. This approximation provides locally mass conservative velocity which is an essential property for mass transport to avoid artificial mass sources and sinks. The transport equation is solved using a combination between the Discontinuous Galerkin Method (DG) and the Multipoint Flux Approximation Method (MPFA). The first one is used to discretize the advection part while the second one is used for the discretization of the dispersion part [53]. As the DG includes the advantageous of both the Finite Element (FE) and the Finite Volume (FV) methods, it gives a robust and an accurate numerical scheme [48]. Considering the MPFA and as stated by [1, 2, 20, 36, 51] it is locally conservative and could handle irregular grids on anisotropic heterogeneous domains. On the other hand, both the MPFA and DG use the same type of unknowns that give the advantage of gathering it into one system matrix [53]. At this end, the combination (DG-MPFA) has shown to be a robust and accurate approach for modelling density driven flow problems [3, 52, and 55]. Non iterative time stepping is used in this work. The scheme based on local truncation error control as in [54]. It was able to increase the numerical accuracy and to reduce the computational cost at the same time [54].

2. Experimental set-up

The experimental device is represented in Figures (2, 3). The fracture is constituted of two salt blocks dimensions 9.9 x 3.5 x 0.42 cm^3 spaced about 0.4 cm apart. The blocks were obtained by cutting from a compacted salt loaf used in cattle feed. The salt blocks were inserted between two parallel transparent glass plates supported by a rigid metal structure. During this operation, the fracture aperture can undergo a slight decrease estimated at about 0.025 – 0.075 mm. In order to ensure a good adhesion between the salt blocks and glass plates, the former were polished with very fine sandpaper. The impermeability of lateral boundaries is guaranteed by rubber seals. The cell is initially filled with fully saturated saline solution (C_{sat} = 357 g/L). After about 12 hours, in order to induce dissolution of the rock matrix, distilled water is injected at low flow rate (Q_v = 1.0 mL/h) into the lower part of the cell *via* a plastic injection tip. The injection tip (1.5 mm inner diameter) is centered between the two plates and located 2.0 mm above the lower cell edge. A peristaltic pump ensures a quasi-constant flow rate. The mixing between the injected fluid and the dissolved part of the rock matrix is removed through an exhaust nozzle disposed in the same way as the injection tip but in the upper part of the cell. In order to better visualize the dissolution of the salt blocks, the injected fluid was stained by adding a few milligrams of fluorescein. Illuminated by a homogeneous light source located behind the experimental model, the temporal and spatial evolution of the flow channel between the salt blocks is followed using a numerical camera with a standard Charge Coupled Device (CCD) detector consisting of 3888 x 2592 pixels. As the numerical camera is set in front of the experimental model, the recorded images, caught at various interval of time, are analyzed by image processing software.

The experimental configuration is characterized by a more rapidly dissolution in the upper part than in the lower part. This behavior suggests that the fracture dissolution is the result of the free buoyant convection. The less dense fluid will overcome the denser fluid resulting in different dissolution rates in agreement with the fracture height. For relatively short times, *i.e.*: at the beginning of the experiment (t < 10h) the dissolution rate increases approximately linearly with the fracture height while for relatively high times (t > 20h), the fracture dissolution is more rapidly in the upper part than in the lower part.

However, we must note that the analysis of our experimental results highlighted the emergence and the development of the gas bubbles arising from degassing during the dissolution of the rock matrix (small black spots located in the flow channel). Despite setting in saturated of the salt blocks more than 12 hours followed by vacuum degassing or the injection of CO_2, this degassing phenomenon was observed for each carried out experiment. To verify the influence of this phenomenon on the spatial-temporal fracture evolution, the experiment was repeated at least twice. A very good reproducibility was observed. It not only shows a weak influence of the degassing phenomenon on the fracture dissolution but also a relatively small impact of the heterogeneities of the porous matrix.

3. Mathematical model

Taking into account the experimental conditions, the creeping flow and the transport into the fracture can be described by the following system of equations [21, 28, 38, 3, 10, 19]:

Stokes equation:

$$\nabla p - \mu \nabla^2 \boldsymbol{u} = \rho \boldsymbol{g} \tag{1}$$

Continuity equation:

$$\nabla . \boldsymbol{u} = 0 \tag{2}$$

The solute mass conservation with dissolution is written in term of mass fraction as follows:

$$\frac{\partial (\rho C)}{\partial t} + \nabla . (\rho C \boldsymbol{u} - \rho D . \nabla C) = \lambda \left(C_{sat} - C \right) \tag{3}$$

State equations linking density and viscosity to mass fraction:

$$\rho = \rho_0 + \left(\rho_1 - \rho_0 \right) C, \quad and \quad \mu = \mu_0 \left(\frac{\mu_1}{\mu_0} \right)^C \tag{4}$$

where ρ is the fluid density [ML^{-3}], t the time [T], C the solute mass fraction [M. salt/M. fluid], $\boldsymbol{u}$ the velocity [LT^{-1}], ρ_0 the density of the injected fluid [ML^{-3}], g the gravity acceleration [LT^{-2}], μ the fluid

dynamic viscosity [$ML^{-1}T^{-1}$], λ is the "modified" mass transfer coefficient [$ML^{-3}T^{-1}$], α_L and α_T the longitudinal and transverse dispersivities [L], D is the diffusion coefficient [L^2T^{-1}], ρ_1 and μ_1 are respectively, density and viscosity of the high density fluid (saltwater) and μ_0 the viscosity of the injected fluid. The associated boundary conditions of the flow-transport system are of Dirichlet, Neuman or mixed type.

3.1. SPATIAL DISCRETIZATION OF THE FLOW EQUATION

The system (1)-(2) cannot be discretized with the same order for pressure and velocity approximations due to stability conditions. Otherwise some sort of stabilization is added to the mixed formulation [40]. To avoid these difficulties, we use the non-conforming Crouzeix-Raviart (CR) elements for the velocity approximation in combination with constant pressure per element, since they satisfy the Babuska-Brezzi condition [12, 24, 25]. This condition is central for ensuring that the final linear system to solve is non-singular [39]. Moreover, the non-conforming Crouzeix-Raviart (CR) element has local mass conservation properties [13] and leads to a relatively small number of unknowns due to the low-order shape functions. The CR element is used in many problems such as the Darcy-Stokes problem [14], the Stokes problem [18] and the elasticity problem [26, 27]. The CR element gives a simple, stable and optimal order approximation of the Stokes equations [7]. In the following, we recall the main stages for the discretization of the Stokes equation with the CR triangular element.

With the non-conforming finite element method, the degrees of freedom for the velocity vector $\boldsymbol{u}$ are the two components (u_i, v_i) of $\boldsymbol{u}$ at the midedge i facing the node i (Fig. 4). Inside the element E, we assume a linear variation of the velocity components (u_E, v_E)

$$u_E = u_i\varphi_i^E + u_j\varphi_j^E + u_k\varphi_k^E \quad , \quad v_E = v_i\varphi_i^E + v_j\varphi_j^E + v_k\varphi_k^E \tag{5}$$

Where the interpolation function φ_i^E equals 1 on the midedge i and zero on the midedges j and k of E.

The variational formulation of the Stokes equation (1) using the test function φ_i over the domain Ω writes:

$$\int_\Omega \nabla.\left(\mu\nabla\boldsymbol{u} - p\boldsymbol{I}\right)\varphi_i = \int_\Omega \rho g \nabla z \varphi_i \tag{6}$$

where $\nabla\boldsymbol{u}$ is the gradient of the velocity vector $\boldsymbol{u}$ and $\boldsymbol{I}$ the 2×2 identity matrix.

Using Green's formula,

$$\int_{\partial\Omega} \varphi_i \left(\mu\nabla\boldsymbol{u} - p\boldsymbol{I}\right)\boldsymbol{\eta}_{\partial\Omega} - \int_\Omega \nabla.\left(\mu\nabla\boldsymbol{u} - p\boldsymbol{I}\right)\varphi_i = \int_\Omega \rho g \nabla z \varphi_i \tag{7}$$

The first integral contains boundary conditions. It vanishes in case of free-flow boundary or in case of an interior edge i. In this last case, equation (7) becomes

$$-\int_E \nabla.\left(\mu\nabla \boldsymbol{u}_E - p_E \boldsymbol{I}\right)\varphi_i^E - \int_{E'} \nabla.\left(\mu\nabla \boldsymbol{u}_{E'} - p_{E'} \boldsymbol{I}\right)\varphi_i^{E'} = \int_E \rho g \nabla z \varphi_i^E + \int_{E'} \rho g \nabla z \varphi_i^{E'} \tag{8}$$

Using (6) we obtain

$$-\int_E \nabla.\left(\mu\nabla \boldsymbol{u}_E - p_E \boldsymbol{I}\right)\varphi_i^E = \begin{pmatrix} \Delta z^i \\ \Delta x^i \end{pmatrix} P_E - \frac{\mu}{|E|}\begin{pmatrix} \sum_{j=1}^{3}\left(\Delta x^i \Delta x^j + \Delta z^i \Delta z^j\right)u_j \\ \sum_{j=1}^{3}\left(\Delta x^i \Delta x^j + \Delta z^i \Delta z^j\right)v_j \end{pmatrix} \tag{9}$$

and

$$\int_E \rho g \nabla z \varphi_i^E = \rho_E g\left(\overline{z}_i - z_E\right)\begin{pmatrix} \Delta z^i \\ \Delta x^i \end{pmatrix} \tag{10}$$

where $\Delta x^i = x_j - x_k$ and $\Delta z^i = z_k - z_j$, z_E and $\overline{z}_i$ are respectively the z-coordinate of the centre of E and of the midpoint of edge i, ρ_E and p_E are respectively the mean density and pressure over E.

The finite volume formulation of the continuity equation (2) over the element E writes:

$$\int_E \nabla.\boldsymbol{u} = 0 \tag{11}$$

using (5), it becomes

$$\sum_{j=1}^{3}\left(\Delta z^j u_j + \Delta x^j v_j\right) = 0 \tag{12}$$

The final system to solve for the flow is obtained by writing equation (8) for each edge (two equations per edge) and equation (12) for each element.

3.2. SPATIAL DISCRETIZATION OF THE TRANSPORT EQUATION

Standard numerical methods, such as FE or FV, usually generate solution with numerical diffusion and/or non-physical oscillations when the advection part is dominant within the transport equation. The DG allows us to avoid these oscillations [49] since it provides high-resolution scheme for advection. The local conservation of FV methods are maintained by the DG, in addition it allows higher order approximations that could be used through a variational formulation in place of some hybridised difference or functional reconstruction [35]. The method was used on diffusion-advection problems in [9, 15, 29] and multiple strategies have been used to adapt the DG method to elliptic problems [4, 8]. More details of DG methods can be found in [8, 16, 17].

Concerning the hyperbolic systems, the DG method has proven to be superior to the already existing FE methods [8]. The DG method is used to solve the advection equation and combined with the Multipoint Flux Approximation (MPFA) method for the dispersion equation.

The MPFA is locally conservative and handle general irregular grids on anisotropic heterogeneous domains. The MPFA method can be combined with the DG method without the time splitting procedure [53]. Since the MPFA and the DG use the same type of unknowns (average value per element), therefore both discretizations can be gathered into one system matrix.

The spatial discretization of the DG-MPFA is given as follows:

By substituting the mass conservation of the fluid in the transport equation [43] and referring to [3], the transport equation (3) can then be written in the following mixed form:

$$\begin{cases} \dfrac{\partial C}{\partial t} + \boldsymbol{u}.\nabla C + \nabla.\boldsymbol{u}_D = \lambda'\left(C_{sat} - C\right) \\ \boldsymbol{u}_D = -\boldsymbol{D}.\nabla C \end{cases} \tag{13}$$

where $\lambda' = \lambda / \rho$, and the dispersive flux $\boldsymbol{u}_D$ is assumed to vary linearly inside the element E, therefore,

$$\int_E \nabla.\boldsymbol{u}_D dE = \int_{\partial E} \boldsymbol{u}_D.n_{\partial E} dl = \sum_i Q_{D,i}^E \qquad \Rightarrow \qquad \nabla.\boldsymbol{u}_D = \frac{1}{|E|}\sum_i Q_{D,i}^E \tag{14}$$

where $Q_{D,i}^E$ is the dispersive flux across the edge *i*.

We use the *P*1 DG method where the approximate solution $C_h(\boldsymbol{x},t)$ is expressed with linear basis functions ϕ_i^E on each element E as follows:

$$C_h\left(\boldsymbol{x},t\right)|_E = \sum_{i=1}^{3} C_i^E\left(t\right)\phi_i^E\left(\boldsymbol{x}\right) \tag{15}$$

The three unknowns for each element are the average value of the mass fraction defined at the triangle centroid $\left(\overline{x}_E, \overline{y}_E\right)$ and its deviations in each space direction [16] with the corresponding interpolation functions:

$$\phi_1^E\left(x,y\right) = 1, \quad \phi_2^E\left(x,y\right) = x - \overline{x}_E, \ \phi_3^E\left(x,y\right) = y - \overline{y}_E. \tag{16}$$

The variational formulation of (13) over the element E using ϕ_i^E as test functions gives (see [53]),

$$\begin{aligned} \sum_j \frac{\partial C_j^E}{\partial t}\int_E \phi_j^E\phi_i^E - \sum_j \int_E C_j^E\phi_j^E\,\boldsymbol{u}.\nabla\phi_i^E - \sum_j \int_E C_j^E\phi_j^E\,\phi_i^E\nabla.\boldsymbol{u} \\ + \int_{\partial E} C^*\phi_i^E\,\boldsymbol{u}.\boldsymbol{\eta}_{\partial E} + \int_E \frac{1}{|E|}\sum_{\partial Ej} Q_{D,j}^E\,\phi_i^E = \int_E \lambda_E^{'}\left(C_{sat} - C\right)\phi_i^E \end{aligned} \tag{17}$$

where ∂E is the boundary edge of the element *E*, and C^* the upstream mass fraction on ∂E, and

$\lambda_E^{'} = \lambda / \rho_E$ where the density ρ_E is considered as constant inside the element *E*.

More details about the expression of the left hand side terms in (18) could be found in [52].

Concerning the right hand side term in (17): $\int_E \lambda_E^{'} \left(C_{sat} - C\right) \phi_i^E$

$$\int_E \lambda_E^{'} (C_{sat} - C)\phi_i^E = \lambda_E^{'} C_{sat} \int_E \phi_i^E - \lambda_E^{'} \theta \int_E C^{n+1} \phi_i^E - \lambda_E^{'} (1-\theta) \int_E C^n \phi_i^E \tag{18}$$

Where

$$\theta = \begin{cases} 0, \textit{ for a full explicit scheme} \\ 1, \textit{ for a full implicit scheme} \end{cases} \tag{19}$$

3.3. DISSOLUTION PROCESS

To model the salt dissolution process, we used a technique based on the variation of the size of the mesh. The simulated domain is only the water circulation area (*i.e.*, flow channel), and as long as the dissolution occurs, the size of the mesh within this area will increase (Fig.5). The variation of mesh size is directly related to the amount of dissolved salt. For an element E with area $|E|$, the dissolved mass within an interval of time dt is given as follows:

$$Q = \lambda (C_{sat} - C)|E| = \frac{dm}{dt} \tag{20}$$

where dm is the amount of the dissolved mass within an interval of time dt.

Knowing the density definition of a certain amount of salt:

$$\rho_s = \frac{dm}{dA.e} \tag{21}$$

where ρ_s is the salt density, $dA.e$ is the volume of the dissolved salt, with dA the dissolved area and e the dissolved thickness. In the case of 2D dissolution process the volume is then reduced to the area dA. Using (21) in (20) we get:

$$dA = \frac{\lambda |E| (C_{sat} - C).dt}{\rho_s} \tag{22}$$

As shown in (Fig.6), the area of the dissolved salt could be approximated as follows:

$$dA = dh.dy \tag{23}$$

where dh is the increment that should be added to the edge at the salt boundary, and dy is the height of that edge. And since the coordinate variation is related to the nodes, then in case of multiple edges at the salt boundary, the amount of dissolved area at each edge is divided on the two corresponding nodes. In this case, the height dy used in (23) to deduce the amount of coordinate increment dh for each node, is

nothing but the sum of the halves of the two edges sharing the same node (Fig.7). Consequently, the increment dh can be calculated for each node *n* at the salt boundary as follows:

$$dh(n) = \frac{\lambda |E| (C_{sat} - C).dt}{2.dy(n).\rho_s} \tag{24}$$

and then it is added to the horizontal ordinate of that node at each time step.

4. Coupling flow and transport equations

Numerical simulations of density driven problems require excessive computational time and/or heavy equipments due to the strong nonlinearities between the flow and the transport equations. In order to reduce the computational needs and maintaining accuracy at the same time, a non iterative time stepping scheme based on local truncation error control is used as in [54]. The time stepping procedure is shown as follows:

The local time truncation error of the concentration is evaluated using two approximations of adjacent order of accuracy.

$$\boldsymbol{e}^{n+1} \approx \frac{1}{2}\left| C^{n+1} - \left(C^n + \frac{\Delta t^{n+1}}{\Delta t^n}\left(C^n - C^{n-1} \right) \right) \right| \tag{25}$$

The time step is accepted if the absolute error criterion is verified,

$$\left| \boldsymbol{e}^{n+1} \right| < \gamma \tag{26}$$

If this criterion is met, the following time step is controlled by the temporal truncation error tolerance γ using,

$$\Delta t^{n+1} = \Delta t^n \times \min\left(s\sqrt{\frac{\gamma}{max\left|\boldsymbol{e}^{n+1}\right|}}, r_{max} \right) \tag{27}$$

If the error criterion is not satisfied, the current time step is repeated using the latest error estimate

$$\Delta t_{j+1}^{n+1} = \Delta t_j^{n+1} \times \max\left(s\sqrt{\frac{\gamma}{max\left|\boldsymbol{e}^{n+1}\right|}}, r_{min} \right) \tag{28}$$

where j indexes the recursive step size reduction, r_{max} and r_{min} are used to limit multiplication and reduction factors and often set equal to 2.0 and 0.1 respectively and $s = 0.9$ a safety factor [50]. And the temporal truncation error tolerance is set to $\gamma = 0.01$.

5. Results and discussion

The dissolution results of the laboratory experiments shown refer to the salt block shape after 10, 20, 30 and 40 hours (Fig.8). The dissolution is significantly remarkable after 40h, and the dissolution at the top of the domain is much more important than at the bottom. Despite the direction of freshwater from below to above, the low flow velocity value makes the density effect much more important than the boundary flux effect of the pump. When dissolution occurs, high density fluid tends to rise and less dense fluid tend to sink within the fracture. Referring to equation (20), the dissolution process between solid salt and fluid is directly related to the concentration gradient, thus, dissolution is much more important when the fluid is not saturated (i.e. low concentration value). And because the less dense fluid is less saturated, the dissolution at the top is larger than at the bottom where the fluid with higher density is saturated. Due to the fact that the observed dissolution is symmetric with respect to the centre of the domain (Fig. 8), only half of the domain was simulated. Therefore, a 2mm wide and 10 cm high fracture is simulated. The flow and transport equations are solved within the fracture, and the dissolution effect is considered by increasing the size of the fracture (i.e. size of the mesh). The horizontal ordinate of the nodes at the salt boundary increases as per equation (24) at each time step. And the horizontal ordinates of all the other nodes within the domain increase proportionally to the boundary nodes. This results in a homogeneous mesh variation after each time step. A remarkable change of the size of the mesh is observed especially at the top of the domain; this variation tends to be less important when going towards the bottom. The mesh variation profile confirms the experimental results that show an important dissolution at the top with respect to the amount of dissolution that occurs at the bottom, especially after 40h of injection. Even for earlier times, the numerical results are also similar to the laboratory experiments (Fig. 9). The concentration distribution (Fig. 9 e) affirms the importance of the density effect with respect to the injection flux. High concentration values are observed at the bottom and result in a very low the concentration gradient between the salt block and the water domain. Therefore, the amount of dissolution is lower than at the top of the domain.

6. Conclusion

The current study reveals the importance of small scale dissolution experiments when trying to understand larger field dissolution phenomena. In the presented laboratory experiments a low freshwater flux was induced at the opposite of gravity direction. The freshwater flow through a small fracture between two salt blocks was observed for 40h, and dissolution occurred from both sides. The results show a high amount of dissolution at the top of the domain, and a reduced dissolution towards the base. A specific numerical

model was developed to simulate the dissolution problem. The numerical code is based on efficient advanced approximations for both spatial and temporal discretization in order to reduce the high computational needs and maintaining accuracy at the same time. The numerical model is developed for a general triangular mesh and uses the CR finite element method to solve the flow, coupled with DG method to solve the advection and MPFA method to solve the dispersion. For the temporal discretization a non-iterative time stepping scheme based on local truncation error control was used. In addition, the dissolution process is treated numerically by using a dynamic mesh procedure. The mesh variation is based on the amount of dissolution flux (i.e. mass) at each edge of the salt boundary. The numerical results were found in a good agreement with the laboratory experiments. Hence, the results show the efficiency of the developed scheme for solving density driven flow in a reactive dissolution media.

ACKNOWLEDGMENTS

This study was partially supported by the SNF (Swiss National Foundation, Grant 200020_125167), whose support is gratefully acknowledged.

References

[1] Aavatsmark, I.: An introduction to multipoint flux approximations for quadrilateral grids. Computat Geoscien,6:404-432, (2002).

[2] Aavatsmark, I., Barkve, T., Bøe, Ø., Mannseth, T.: Discretization on non-orthogonal, quadrilateral grids for inhomogeneous, anisotropic media. J Computat Physics;127:2-14, (1996).

[3] Ackerer, P., Younes, A.: Efficient approximations for the simulation of density driven flow in porous media. Adv Water Res;31:15-27, (2008).

[4] Aizinger, V., Dawson, C., Cockburn, B., Castillo, P.: The local discontinuous Galerkin method for contaminant transport. Adv Water Res; 24:73-87, (2001).

[5] Anderson, R. Y., Kirkland, D. W.: Dissolution of salt deposits by brine density flow, *Geology*, *8*, 66−69, (1980).

[6] Arbogast, T., Lehr, HL.: Homogenization of a Darcy-Stokes system modeling vuggy porous media. *Comput. Geosci.*, 10:291, (2006).

[7] Arnoldk, DN.: On nonconforming linear-constant elements for some variants of the Stokes equations, presenta dal s.c. Franco Brezzi nella seduta del 24-6-93.

[8] Arnold, DN., Brezzi, F., Cockburn, B., Marini, LD.: Unified analysis of discontinuousGalerkinmethods for elliptic problems. SIAM J. Numer. Anal.;5:1749-1779,(2002).

[9] Baumann, C.E, Oden, JT.: A discontinuous hp finite element method for convection–diffusionproblems. *Comput. Methods App Mech. Eng.*;175:311–341,(1999).

[10] Bear, J.: *Dynamics of Fluids in Porous Media* ~Elsevier, New York, (1972).

[11] Beavers, G., Joseph, D.: Boundary conditions at a naturally permeable wall, *J. Fluid Mech.*, 30:197, (1967).

[12] Brezzi, F., Fortin, M.: Mixed and hybrid finite element methods, Berlin: Springer (1991).

[13] Bruman, E., Hansbo, P.: A stabilized nonconforming finite element method for incompressible flow, *Comput. Methods App Mech. Eng.*,vol. 195, num. 23-24, p. 2881-99, (2004).

[14] Bruman, E., Hansbo, P.: Stabilized Crouzeix-Raviart element for the Darcy-Stokes problem, *Numerical Methods for Partial Differential Equation*,21(5), 986-997,(2005).

[15] Cockburn, B., Hou S., Shu, CW.: TVB Runge Kutta local projection discontinuous Galerkin finite element method for conservative laws III: One dimensional systems. J Comput Phys;84: 90-113,(1989).

[16] Cockburn, B., Shu, CW.: The Runge-Kutta Discontinuous Galerkin Method for conservative laws V: Multidimentional Systems. J Comput Phys;141:199-224,(1998).

[17] Cockburn, B., Karniadakis, GE., Shu CW.(Eds.): Discontinuous Galerkin Methods: Theory, Computation and Applications. Lecture Notes in Computational Science and Engineering;11:Springer-Verlag,(2000).

[18] Crouzeix, M., Raviart, P.: Conforming and nonconforming finite element methods for solving the stationary Stokes equations. *RAIRO Sér. Rouge*,7(3), 33-75, (1973).

[19] Diersch, H.J, Kolditz, O.: Coupled groundwater flow and transport: 2. Thermoline and 3D convection systems, Adv Water Res;21:401-425,(1998).

[20] Edwards, M.G., Rogers, C.F.: Finite volume discretization with imposed flux continuity for the general tensor pressure equation. Computat Geoscien,2:259-290, (1998).

[21] Flekkøy, EG., Rage, T., Oxaal, U., Feder, J.: Hydrodynamic Irreversibility in Creeping Flow, *Phys. Rev*, PACS numbers: 47.15.Gf, 02.70.Bf, 02.70.Lq, 47.60.+I, VOLUME 77, NUMBER 20,*(*1996).

[22] Frumkin, A.: Speleogenesis in salt − the Mount Sedom area, Israel, in *Speloegenesis − evolution of karst aquifers*, edited by A. B. Klimchouk, D. C. Ford, A. N. Palmer and W. Dreybrodt, pp. 443−451, National Speleological Society, Huntsville, (2000).

[23] Frumkin, A., Raz, E..: Collapse and subsidence associated with salt karstification along the Dead Sea, Carbonates Evaporates, 16(2), 117-130,(2001).

[24] Girault, V., Raviart, PA.: Finite element methods for Navier-Stokes equations, Berlin: Springer (1986).

[25] Gresho, PM., Sani, RL.: Incompressible flow and the finite element method, New York: Wiley; (1998).

[26] Hansbo, P.: Larson MG. Discontinuous Galerkin and the Crouzeix-Raviart element: application to elasticity. *ESAIM: Math. Model. Numer. Anal.*,37(1), 63-72, (*2003)*.

[27] Hansbo, P., Larson, MG.: Discontinuous Galerkin methods for incompressible and nearly incompressible elasticity by Nitshe's method. *Comput. Methods Appl. Mech. Engrg*,191(17-18), 1895-1908, (2002) .

[28] Happel, J., Brenner, H.: *Low Reynolds Number Hydrodynamics* (Prentice Hall Inc., Englewood Cliffs, NJ,1965).

[29] Hughes, TJR., Masud, A., Wan, J.: A stabilized mixed discontinuous Galerkin method for Darcy flow. Computat Meth Appl Mech Engrg;195(25-28):3347- 3381,(2006).

[30] Huyakorn, P., Anderson, P., Mercer, J., White, H.: Saltwater intrusion in aquifers: development and testing of a three-dimensional finite element model. Water Resour Res;23:293-312,(1987).

[31] Jäger, W., Mikelić, A.: On the interface boundary condition of Beavers, Joseph, and Saffman. *SIAM J. Appl. Math.* 60:1111, (2000).

[32] Jäger, W., Mikelić, A.: Asymptotic analysis of the laminar viscous flow over a porous bed. *SIAM J. Sci. Comput.*, 22:2006, (2001a).

[33] Johnson, K. S: Dissolution of salt on the east flank of the Permian Basin in the southwestern U.S.A., *J. Hydrol.*, *54*, 75−93, (1981).

[34] Kaviany, M.: Principles of Heat Transfer in Porous Media, *Mechanical Engineering Series*, Springer-Verlag, New York, (1999).

[35] Kirby, R.: A Posteriori Error Estimates and Local Time-Stepping for Flow and Transport Problems in Porous Media, Ph.D thesis, University of Texas at Austin, (2000).

[36] Klausen, R.A, Russell T.F.: Relationships among some locally conservative discretization methods which handle discontinuous coefficients. Journal Computat Geoscien,8(4):1-37, (2004).

[37] Kozary, M.T., Dunlap, J. C. and Humphrey, W. E.: Incidence of saline deposits in geologic time, *Geol. Soc. Am. Spec. Pap.*, *88*, 43−57, (1968).

[38] Landau, LD., Lifshitz, EM.: *Fluid Mechanics* (Pergamon Press, New York, 1987), 2nd ed.

[39] Langtangen, HP., Mardal, K., Winther, R.: Numerical methods for incompressible viscous flow. *Adv. Water Res*. 25, 1125-1146, (2002).

[40] Li, J., Chen, Z.: A new local stabilized nonconforming finite element method for the Stokes equations, *Computing,* 82:157-170, doi 10.1007/s00607-008-0001-z, (2008).

[41] Martinez, J. D., Johnson, K. S., Neal, J. T.: Sinkholes in evaporite rocks, *Am. Sci.*, *86*, 38−51. (1998).

[42] McManus, K. M., Hanor, J. S.: Diagenetic evidence for massive evaporite dissolution, fluid flow, and mass transfer in the Louisiana Gulf Coast. Geology, 21, 727?730, (1993).

[43] Oltean, C., Buès, M.A.: Coupled groundwater flow and transport in porous media. A conservative or non-conservative form? Transport in Porous Media, 44 (2), 219-246, (2001).

[44] Quinlan, J. F., Smith, R. A. and Johnson, K. S.: Gypsum karst and salt karst of the United States of America, Le Grotte d'Italia, 4(XIII), 73?92, (1986).

[45] Reuter, F., Stoyan, D.: Sinkholes in carbonate, sulphate, and chloride karst regions: Principles and problems of engineering geological investigations and predictions, with comments for the destruction and mining industries, in Applied karst geology, edited by B. F. Beck, pp. 3?25, A. A. Balkema, Rotterdam, Brookfield, (1993),

[46] Saffman, P.: On the boundary condition at the surface of a porous medium, *Studies Appl. Math*., 50:93, (1971).

[47] Sanchez-Palencia, E.: Non-Homogeneous Media and Vibration Theory, volume 127 of *Lecture Notes in Physics* Spring-Verlag, Berlin (1980).

[48] Shuangzhang, T., Shahrouz, A.: A slope limiting procedure in Discontinuous Galerkin finite element method for gasdynamics applications. Int. J Numer Analy Modell,2:163-178, (2005).

[49] Siegel, P., Mosé, R., Ackerer, P., Jaffre, J.: Solution of the advection-diffusion equation using a combination of discontinuous and mixed finite elements. Int J Numer Meth in Fluids; 24(6): 595-613,(1997).

[50] Sloan, S.W., Abbo, A.J.: Biot consolidation analysis with automatic time stepping and error control. Part 1: Theory and implementation", International journal for numerical and analytical methods in geomechanics, Vol. 23, No. 6, pp. 467-492, (1999).

[51] Wheeler, M.F., Yotov, I.: A multipoint flux mixed finite element method. SIAM44;5:2082-2106,(2006).

[52] Younes, A., Fahs, M., Ahmed, S.: Solving density flow problems with efficient spatial discretizations and higher-order time integration methods, Advances in Water Resources, 32, 340-352, (2009).

[53] Younes A., Ackerer P.: Solving the advection-dispersion equation with Discontinuous Galerkin and Multipoint Flux Approximation methods on unstructured meshes. Int. J Numer Methods in Fluids.DOI: 10.1002/fld.1783, (2008).

[54] Younes, A., Ackerer, P.: Empirical versus time stepping with embedded error control for density-driven flow in porous media", Water Resources Research, Vol. 46, No. 8, (2010).

[55] Zidane, A., Younes, A., Huggenberger, P., Zechner, E.: The Henry semi-analytical solution for saltater intrusion with reduced dispersion, Water Resou Res, VOL. 48, W06533, doi:10.1029/2011WR011157, (2012).

List of Figures

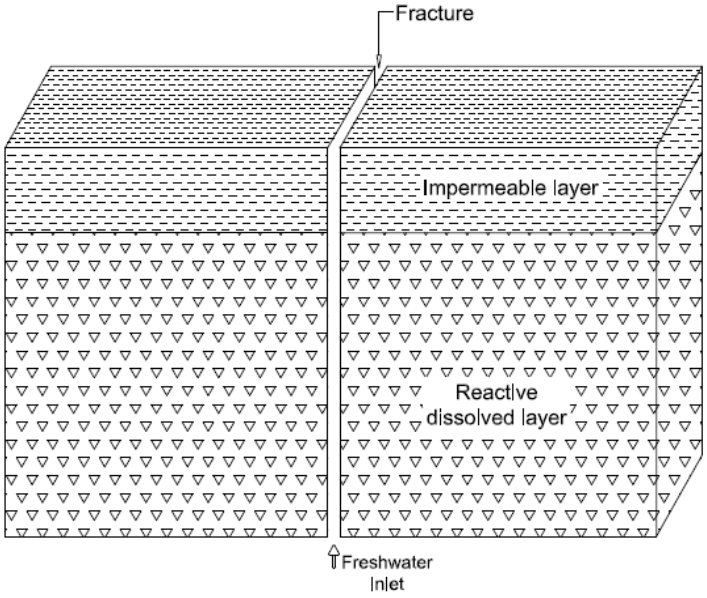

a)

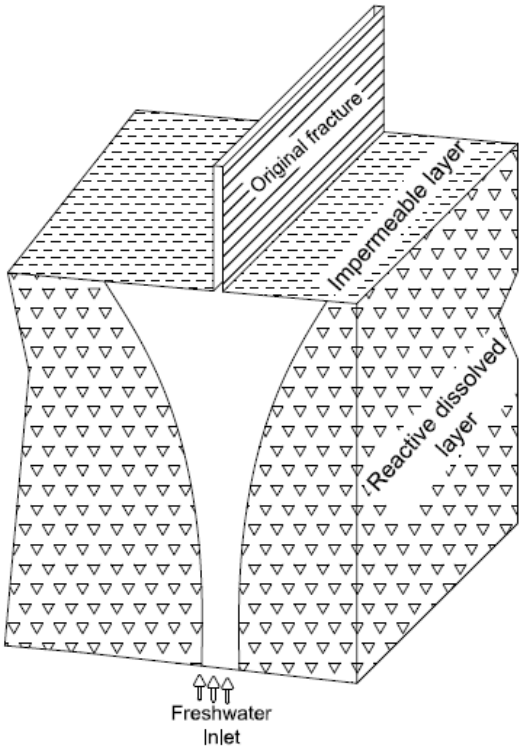

b)

Fig.1: Models of natural dissolution aspects, a) before dissolution and b) after dissolution with non-reactive ceiling.

Fig.2: Domain and boundary condition of the experiment.

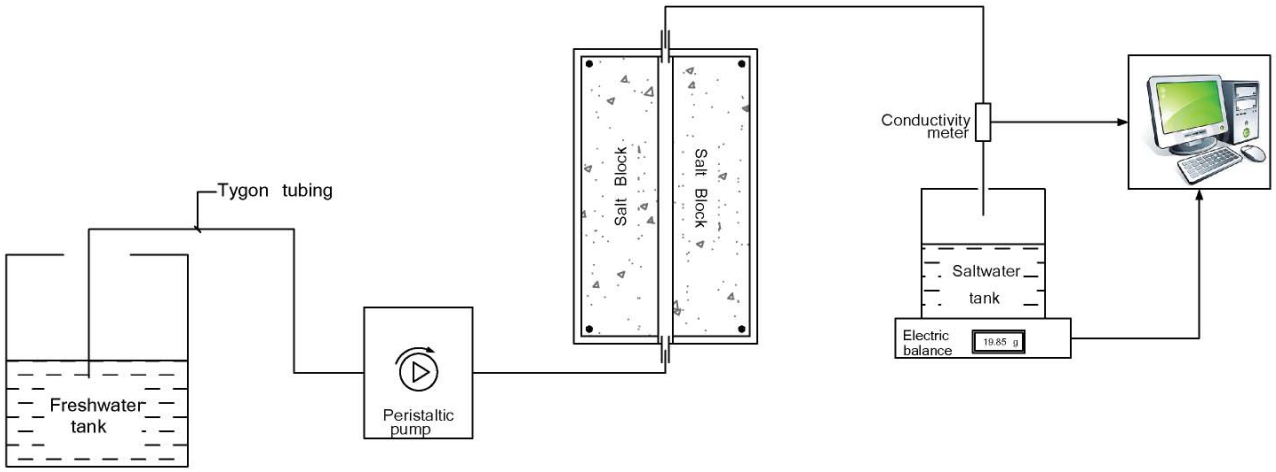

Fig.3: Schematic view of the experimental setup for the laboratory dissolution runs.

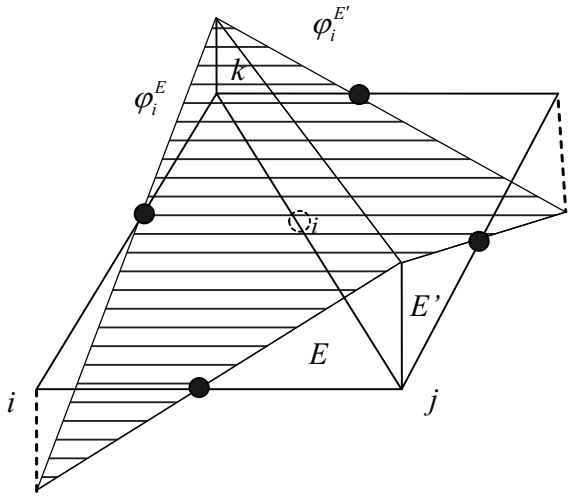

Figure 4: The linear interpolation function for velocity field.

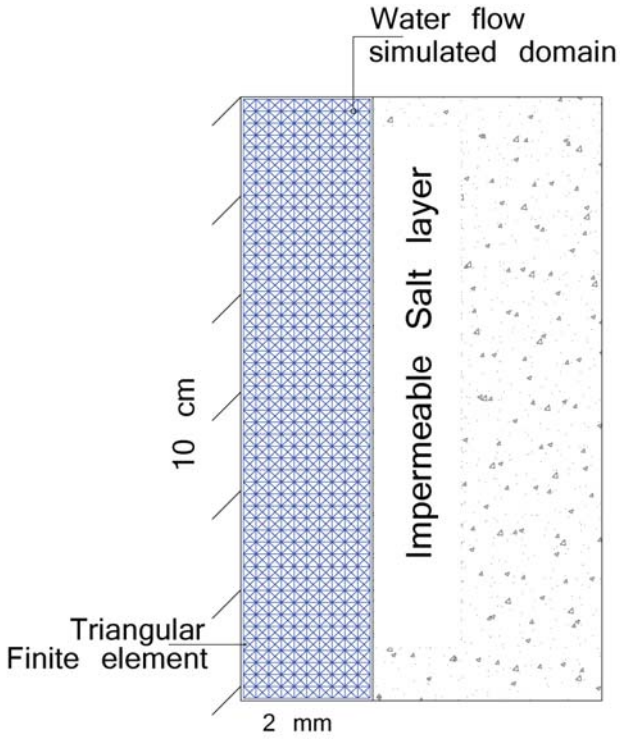

Fig.5: The numerical simulated domain.

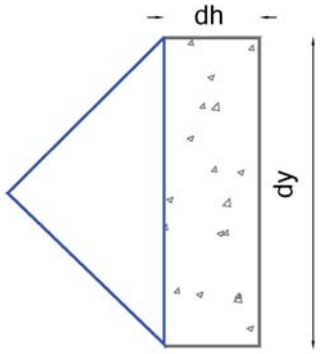

Fig.6: Area of the dissolved salt for one finite element.

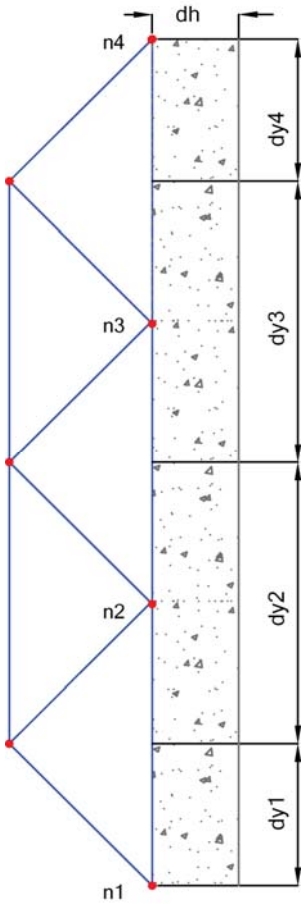

Fig.7: Relative height of the dissolved salt for each node at the boundary.

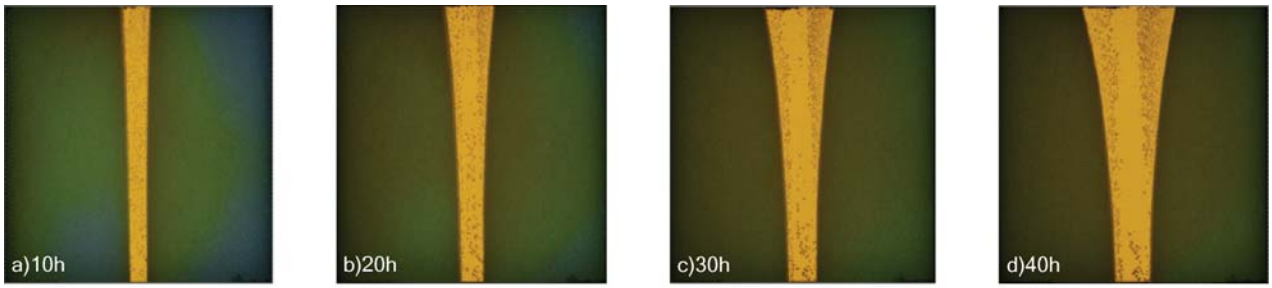

Fig.8: Photograph of the dissolution shape at different time steps of the experiment.

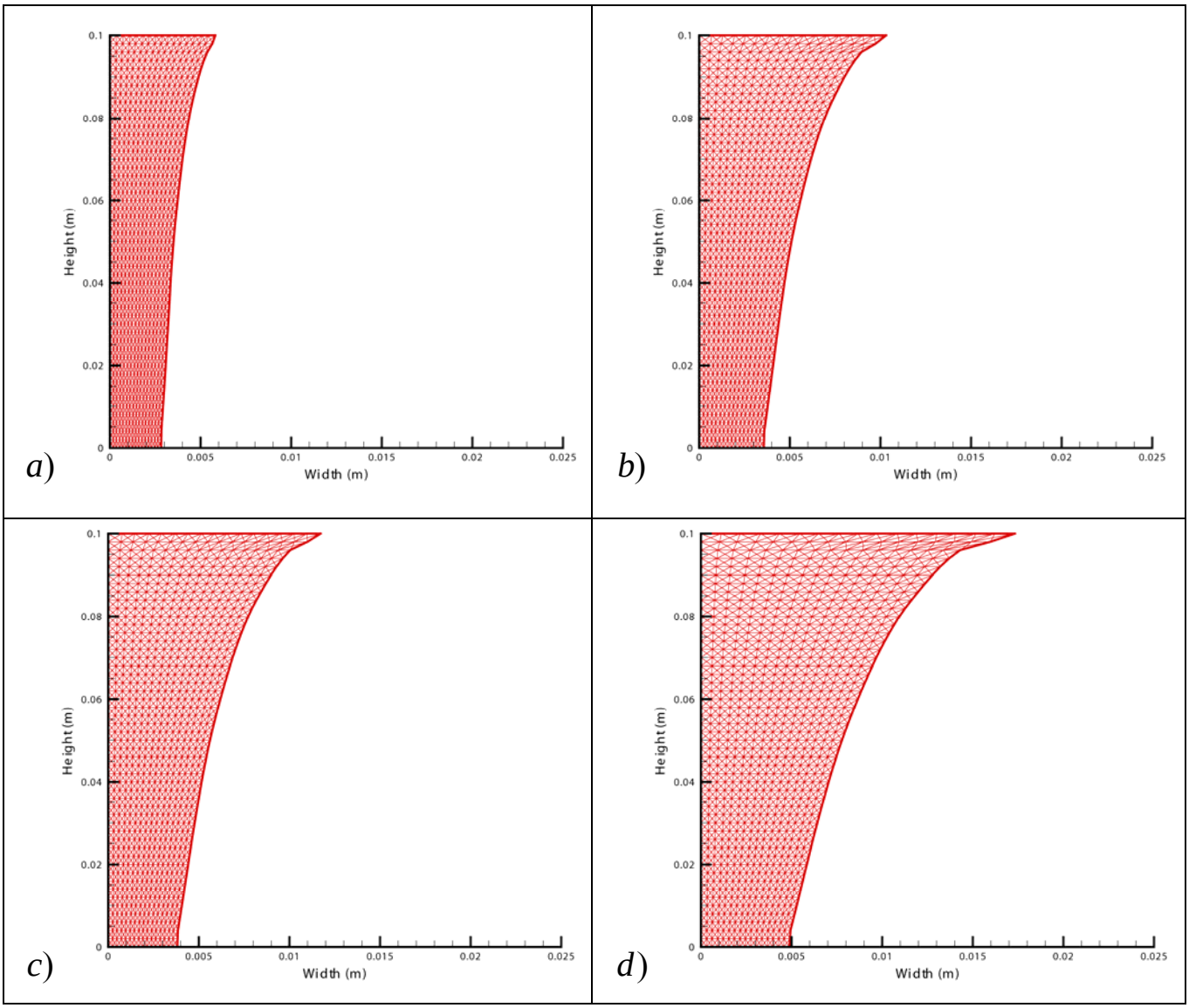
a)
b)
c)
d)
Height (m)
Width (m)
0
0.02
0.04
0.06
0.08
0.1
0.005
0.01
0.015
0.02
0.025

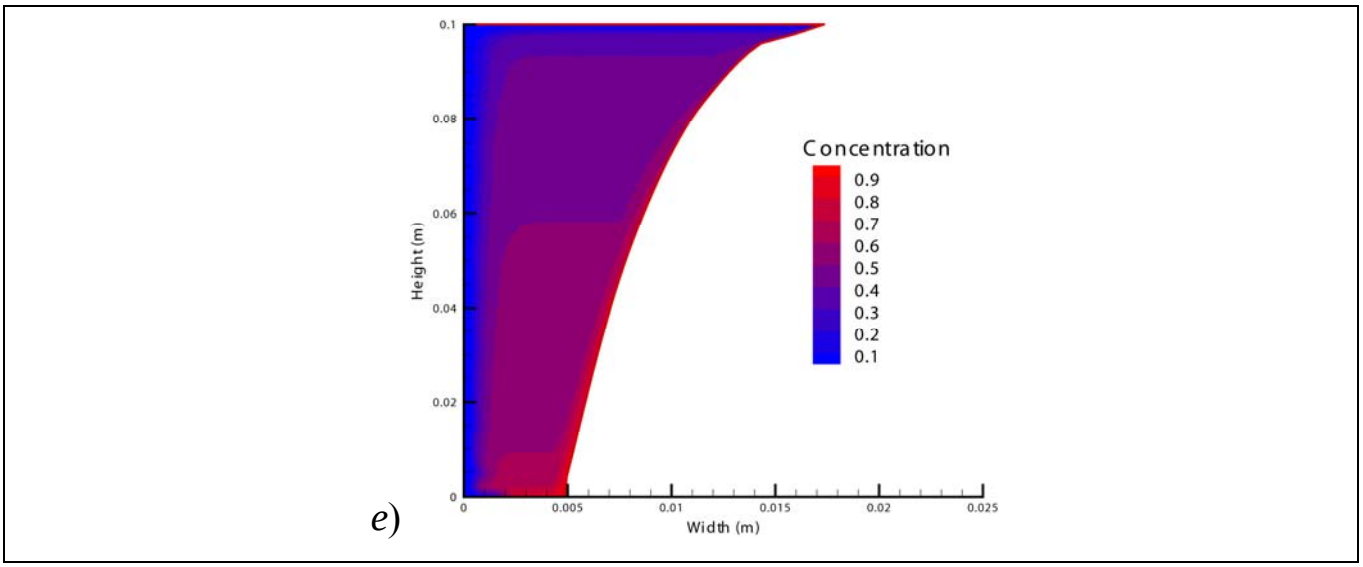

Fig.9: Dynamic mesh variation at different time interval, a)-10h, b)-20h, c)-30h,d)-40h, and e) the normalized concentration distribution after 40h.

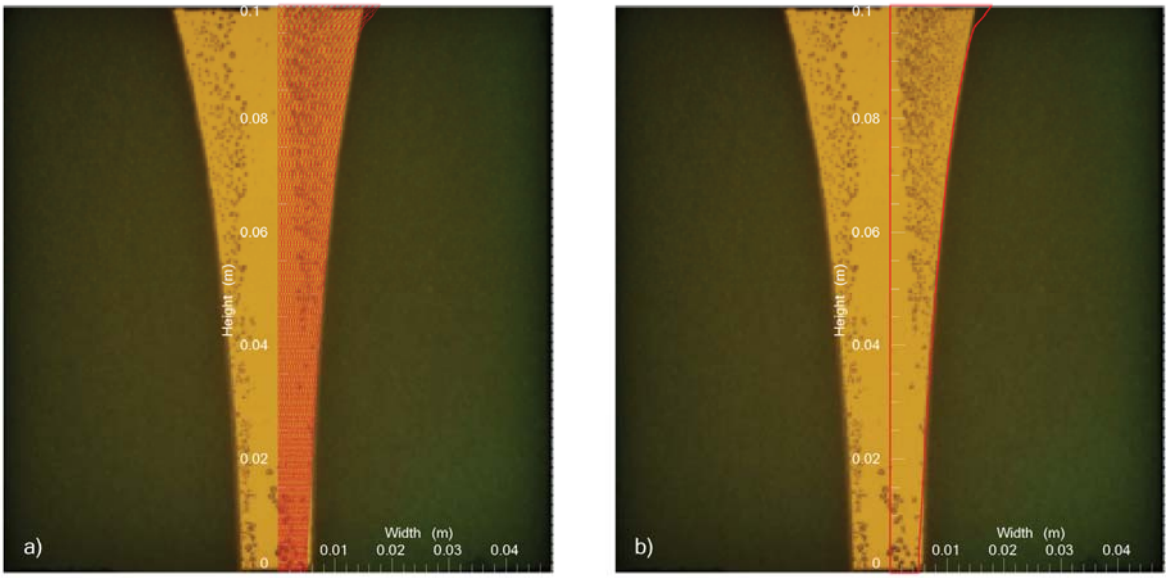

Fig.10: Comparison between the experimental and the simulated results, a)-with mesh, b) - without mesh.

Chapter 6

Evaporite dissolution and risk of subsidence

Contents

Paper submitted to journal of contaminant hydrology

On the effects of subsurface parameters on evaporite dissolution (Switzerland)

Ali Zidane*[(1,2)], Eric Zechner[(1)], Peter Huggenberger[(1)], Anis Younes[(2)]

(1) Institute of Geology and Paleontology, Environmental Sciences Department, University of Basel, Bernouillistr. 32, 4056 Basel, Switzerland

(2) Laboratoire d'Hydrologie et de Geochimie de Strasbourg, University of Strasbourg, CNRS UMR 7517, Strasbourg, France

*** Contact Person: Ali Zidane**

Email: ali.zidane@unibas.ch

Abstract

Uncontrolled subsurface evaporite dissolution could lead to hazards such as land subsidence. Observed subsidences in a study area of Northwestern Switzerland were mainly due to subsurface dissolution (subrosion) of evaporites such as halite and gypsum. A set of 2D density driven flow simulations were evaluated along 1,000 m long and 150 m deep 2D cross sections within the study area that is characterized by tectonic horst and graben structures. The simulations were conducted to study the effect of the different subsurface parameters that could affect the dissolution process. Specific concern is given to the heterogeneity of normal fault zones and its role for the dissolution of evaporites by considering several permeable faults that include non-permeable areas. Results show that a large fault zone consisting of several smaller higher conductive faults is the most important factor that affects the dissolution compared to the other investigated parameters of thickness of the lower karstic aquifer above the halite, a dynamic conductivity of the lower aquifer, and varying boundary conditions in the upper aquifer. The mixed finite element method (MFE) is used to solve the flow equation, coupled with the multipoint flux approximation (MPFA) and the discontinuous Galerkin method (DG) to solve the diffusion and the advection parts of the transport equation.

Keywords: Density driven flow, Discontinuous finite elements, MPFA, Subrosion, Tectonics, Switzerland.

1. Introduction

The importance of density driven flow arises due to its significant role in water resources management and engineering (Oude Essink 2001, Paniconi et al. 2001, and Xue Y et al. 1995). Simulation of saltwater transport models becomes a real need due to the large number of environmental problems such as intrusion of saltwater in coastal aquifers, landfills leakage, collapse of abandoned salt mines, radioactive waste disposal in salt rock formations and subsurface dissolution of evaporites (Oude Essink 2001, Luo et al. 2012, Ludwig et al. 2001, Magri et al. 2009). When carbonate rocks develop cavities over centuries, evaporite rocks can form cavities within days. Therefore, gypsum or rock salt are seen as the most soluble common rock formation (Martinez et al. 1998). Subsurface dissolution or subrosion occurs when non-saturated groundwater gets in contact with evaporitic rock formations. The subsurface karst development can create additional groundwater pathways. As a consequence, additional mobilization of solutes can lead to widespread salinization of aquifers, and also land subsidence. Even comparably small subsidence rates can have an important effect on sensitive urban infrastructures (e.g. dams, buildings, traffic lines, power plants). The dissolution of salt is directly related to the concentration gradient between salt and water. The basic principle was discussed by (Johnson 1981, 2005) when he defined four requirements for dissolution of salt (NaCl) or gypsum ($CaSO_4$): (1) a deposit of salt or gypsum against which, or through which, water can flow, (2) a supply of water subsaturated with Nacl/$CaSO_4$, (3) an outlet where the resulting brine can escape, and (4) energy provided from hydrostatic head differences and/or density gradients, which causes groundwater flow through the system. Human activities can induce or influence any of the four requirements. Zechner et al. (2011) studies three possible causes for the observed land subsidence in northwestern Switzerland: (1) natural dissolution of the evaporites of the Middle Muschelkalk (anhydrite and halite), which is related to the tectonic setting of the evaporitic formations within a set of horst and graben structures, (2) salt solution mining, which has been pursued at different locations over the last 150 years, (3) large scale extraction of groundwater in an overlying fissured aquifer with hydrostatic connection to the underlying evaporites along fault zones with increased hydraulic conductivity. The effects of increased hydrostatic gradient due to both groundwater withdrawal and fluid density contrasts were evaluated in more details with a series of 2D density-coupled solute transport simulations along an approximately 1000-m long, and 150-m deep 2D cross section. Simulation results indicate that the upcoming process of saline

groundwater in to the main aquifer occurs under different distributions of subsurface parameters and hydraulic boundary conditions. For the presented setup the simulations also revealed that the most sensitive factor for the dissolution rate is the structure, or dip of the halite formation, which leads to an increase of dissolution rates with increasing dips. However, the authors pointed out that the assumption of a well-established homogenous karst with a constant thickness of 10 m on top of the salt layer does not take into account the process of evaporitic karst evolution, which is characterized by a dissolution process which is coupled to a dynamic development of subsurface aquifer parts with increasing porosity and hydraulic conductivity.

Therefore, the presented work investigates the role of varying parameters such as aquifer geometry and transient conductivity on the rate of salt dissolution. They include (1) variations of thicknesses of the karst aquifer on top of the salt, or the thickness of the fault zones, (2) a dynamic conductivity of the karst aquifer on top of the salt which is directly related to the amount of the dissolved salt, and, in addition, (3) variations of the imposed hydraulic boundary conditions such as the value of the constant head, or the depth of a well. The 2D simulations are conducted using a numerical code that has been tested on a benchmark laboratory experiment in Konz et al (2008, 2009a, b), Younes et al (2009, 2011) and field scale models (Zechner et al. 2011). In addition, the code has been recently tested against the Henry semianalytical solution for salt water intrusion (Zidane et al. 2012). The karstified evaporites are represented as porous aquifer. The opening porous space and fractures which are created during the dissolution process and result in a transient hydraulic conductivity are simulated with a modified discrete fracture approach (e.g. Kaufmann, 2002). The authors consider the approach valid on the simulated scale due to the fact that no hydraulically relevant larger voids, or conduit network have been observed in the dissolved halite or anhydrite/gypsum formations. Previous studies based on field investigations and data evaluation, e.g. Ludwig et al. (2001), have shown the importance of hydrological heterogeneities at various scales on density-driven transport. Luo et al. (2012) presented a 2D and 3D modeling study to describe the impact of different engineering solutions and appropriate remedial strategies for an abandoned, flooded deep salt mine in Stassfurt, Germany. Luo et al. (2012) found that the hydrogeological structure in the study area played a significant role in development of the subsurface concentration distribution. Due to the typical lack of knowledge about the hydrogeological structure and properties in field studies, different approaches to study the effect of heterogeneity within the simulations were used. Particularly,

more concern is given to the geometry of normal faults and their effect on the subrosion process. To our knowledge, very few studies have investigated the hydraulic role of sub vertical fault zones on the subrosion process. Magri et al. (2011) studied possible explanations for seawater intrusion in the Seferihisar-Balcova Geothermal system in Turkey. They found, based on data acquisitions and numerical simulations, that groundwater flow and coupled hydrochemical and hydrothermal patterns are strongly controlled by fault tectonics. Therefore, specific concern in the presented study is given to the structure of the normal fault zone and its role for the dissolution of evaporites. In particular two approaches are studied, the variable width of the fault and the heterogeneity. In the first approach the effect of different fault widths on the dissolution process is studied, whereas in the second approach the single fault is replaced by several thin faults separated by impermeable areas.

2. Model concept

The study site for the 2D simulations is located in northwestern Switzerland to the east of the southeastern border of the Upper Rhine Graben and is part of the Tabular Jura (Fig. 1). Land subsidence has been observed at six different locations, and monitored subsidence rates reached more than 100 mm/year, affecting area ranges from 100 to 1500 m. The study area is underlain by Triassic and Jurassic strata, which slightly dip to the southeast. The subsidence is mainly caused by subsurface dissolution of halite (rock salt), and partly by dissolution of overlaying anhydrite/gypsum formations of the Middle Muschelkalk. Fracture zones causing increased permeability within the Jurassic and Triassic formations are supposed to favor vertical exchange of groundwater also across aquitards. A 3D geological model consistent with the kinematic evolution of the southeastern border of the Rhinegraben (Spottke et al. 2005) is used to map an approximately 1,000-m-long and 150-m-deep 2D cross section. Regional hydrogeological boundary conditions for the 2D density-coupled solute-transport simulations are derived from a 3D regional groundwater flow model with constant density (Fig. 1, 2). The simulated piezometric head distribution within the Upper Muschelkalk Aquifer shows the effect of the large-scale industrial pumping in the central part of the model (up to 1.5 m^3/s), where the piezometric head is lowered up to 5 m (Fig. 1).

In this study, the geometry and the boundary conditions for the 2D density-coupled models were considered variable parameters. The initial geometry, boundary conditions and physical parameters are similar to the previous models (Zechner et al. 2011), and were subsequently

varied according to the scenarios (Table 1-6). Depending on the simulated scenario, the numerical model contains 29,000 to 35,000 non-regular triangular finite elements. Large elements (5-10 m) are mainly located at the upper aquifer, and their size decreases within the fault zones and the lower aquifer to reach less than 20 cm in some parts. According to the 3D groundwater model, a constant head of 254.5m was initially imposed on the ESE boundary, but it was modified in scenarios (S_Head_2-6) to test its effect on the salt dissolution process. A pumping well located at the WNW end of the 2D cross section was simulated with different lengths and with equally distributed flux on the vertical filter and fitted. The imposed pumping rate of 0.15 m^3/s corresponds to a simulated head of 251.0 m in the well as observed in 3D simulation of regional groundwater hydraulics (Fig. 1). Similarly to the Hydrocoin test case (OECD 1988), an impermeable boundary condition was applied at the lower part of the lower aquifer, with a constant concentration and a density of 1200 kg/m^3. As a consequence, salt can enter the domain only via diffusion effects according to the approximation that salt dissolution is instantaneous compared to the simulated time which is 30 years in all the simulated scenarios (e.g. Alkattan et al. 1997). In all the simulations, the aquifer was initially filled with freshwater (NaCl concentration equals 0) and initial piezometric head was set to 0.
The discrete fracture approach (Gureghian 1975, Huyakorn et al. 1983) is used to simulate density-driven flow within the vertical cross section. Therefore, no additional exchange term between matrix and fractures has to be taken into account in order to couple the matrix and porous flow. Referring to (Ackerer and Younes 2008, Younes et al. 2009) the flow equation in a porous media is given in the following form:

$$\rho S \frac{\partial h}{\partial t} + \varepsilon \frac{\partial \rho}{\partial C} \frac{\partial C}{\partial t} + \rho \nabla \cdot (\boldsymbol{q}) = 0 \qquad (1)$$

where ρ is the fluid density [ML^{-3}], S the specific mass storativity related to head changes [L^{-1}], h the equivalent freshwater head [L], t the time [T], ε the porosity [-], C the solute mass fraction [M. salt/M. fluid], $\boldsymbol{q}$ the Darcy's velocity [LT^{-1}].

3. Effects of varying subsurface parameters

Modeling density driven flow problems requires a nonlinear coupling between flow and transport equations. This nonlinearity is due to the density-viscosity linking between Darcy's flow and the advection dispersion transport equation. The strong nonlinearity between flow and transport can typically lead to long CPU times. A spatial and temporal discretization with efficient advanced

approximations is developed to reduce the high computational need while maintaining accuracy at the same time. The locally conservative method mixed finite element (MFE) is used to discretize the flow, whereas the discontinuous Galerkin (DG) method is used to discretize the advection combined with the multipoint flux approximation (MPFA) for the discretization of the dispersion (Younes et al. 2009, Younes et al. 2011). The (MFE_DG_MPFA) has proven to be an accurate and robust discretization when compared to experimental flow tank benchmark data in Konz et al (2009a).

Firstly, the effect of a dynamic hydraulic conductivity of the lower aquifer were studied, and, consequently, a dynamic porosity that is related proportionally to the variation of the conductivity. Secondly, the effect of the different geometries of the 2D cross sections on the dissolution process was investigated such as geometry and width of fault zones and thickness of the lower aquifer). And finally, the effect of the boundary and initial conditions (value of the hydraulic head, depth of the pumping well) were studied to test their effects on the salt dissolution.

3.1. Hydraulic conductivity

Groundwater flow in karst aquifers is controlled by several processes. A crucial one is the dissolution kinetics that results in karst void, or rapid fracture enlargement within an aquifer and depends on the saturation level of NaCl. A large number of numerical experiments have been conducted to study the evolution of karst aquifer. The studies start with one dimensional models for single fracture enlargement (Dreybrodt 1990, Palmer 1991, Groves and Howard 1994a), and continue to the evolution of two dimensional fracture networks with simple boundary conditions (Groves and Howard 1994b, Howard and Groves 1995, Siemers and Dreybrodt 1998). All of the above mentioned models, and also models that study the flow in a complex porous network (Clemens et al. 1996, Kaufmann and Braun 1999, 2000), did not consider the effect of the increasing conductivity of the fractures. A systematic parameter study for a karst aquifer has been conducted by (Kaufmann 2002). The latter studied the effect of a time dependent conductivity that takes the following form

$$K(t)=\frac{g}{32v}\frac{[d(t)]^3}{\delta} \qquad (2)$$

where g is the acceleration of the gravity, and v is the kinematic viscosity of water. The term $d(t)$

is the time dependent fracture diameter, since the size of the fractures increases with the dissolution process, and δ corresponds to the average fracture spacing. Following Kaufmann (2002), modifications to the equation were introduced (2) in order to include the numerical requirement that accounts for the amount of dissolved salt in the simulated scenarios. The MPFA method allows us to calculate the mass of salt (in kg) that enters the domain through diffusion. The amount of the dissolved mass is time dependent, since it depends on the flow velocity and the saturation level of water. The density definition of the dissolved solid is:

$$\rho_s = \frac{m(t)}{V} \tag{3}$$

where ρ_s [kg/m^3] is the salt density, *m(t)*[kg] is the mass of the dissolved salt block, and *V* [m^3] is the volume of the dissolved salt block. The latter could be expressed in function of the thickness, width and length of the dissolved salt block (Fig. 3).

$$V=L.W.d(t) \tag{4}$$

L, W and *d(t)*[m] are the length, width and thickness (or diameter), respectively, of the dissolved salt. In a 2D model, the width term *W* is set to (*W* =1) in equation (4). Hence, replacing (3) and (4) into equation (2) results in:

$$\begin{cases} K(t) = K(t_0) = 7.4E-4, & if\ t = 0 \\ K(t) = \dfrac{g}{32\upsilon} \dfrac{\left[\dfrac{m(t)}{\rho_s L}\right]^3}{\delta}, & if\ t > 0 \end{cases} \tag{5}$$

In the simulated scenarios δ is considered a constant that is updated iteratively at each time step, and its initial value is simply deduced from the initial value of the conductivity for the lower aquifer which is $K(t_0)=7.4E-4$ (Table 1). At the first time step ($t=t_1$), the amount of the dissolved salt is calculated. Using equation (5), the first value of δ noted δ_0 is then deduced as follows:

$$\delta_0 = \frac{g}{32\upsilon} \frac{\left[\dfrac{m(t_1)}{\rho_s L}\right]^3}{K(t_0)} \tag{6}$$

The updated value of *K* at the time step *n* is then deduced from both the dissolved mass at this time step and the calculated value of δ at *n-1*. As a consequence, two simulations were ran

simultaneously: in the first one the value of the conductivity was kept constant with respect to the dissolved salt, while in the second the hydraulic conductivity increases with respect to the amount of dissolved salt as shown in equation (5). As expected, increasing the conductivity will increase the dissolution rate. Since more freshwater can enter the lower aquifer, the concentration level will be decrease within the lower aquifer, while the concentration gradient will increase. A remarkable increment of the mass input is observed within the first variation of the conductivity value. After this leap, the mass difference between the dynamic and the constant conductivity tends to be constant, especially after $t = 0.2$ years. The steady state of both simulations is reached in 0.5 years (Fig.4).

3.2. Aquifer geometry

The amount of salt that enters the system is controlled by the solute concentration gradient between (saturated) boundary condition and the groundwater in the adjacent lower aquifer. Therefore, the access of freshwater to the lower boundary is also affected by the geometry, or thickness of the lower aquifer and the fault zones, which form a hydraulic connection to the freshwater in the upper aquifer. Zechner et al. (2011) have assumed a uniform lower aquifer and fault zone thickness of 10m. Due the uncertainty related to the thickness of the geometries, different thicknesses ranging from 1 to 10m for the lower aquifer and 0.5 to 40 m for the fault zones were tested to simulate the resulting amount of dissolved salt.

As expected, the x-axis flow velocity component increased when the thickness of the lower aquifer decreased (Fig.5, Scenario S_Lower_1; Table 2). Observed velocities of 5 m/d show that the convective part of the transport equation appears to have an important effect for dispersion of the dissolved salt over the upper aquifer, especially in areas near the two fault zones (Fig.6, Scenario S_Lower_1). The thinner lower aquifer forces the groundwater to flow faster, and therefore accelerates the dissolution process (Fig.7). A considerable decrease of the mass input is noticed when the lower aquifer thickness increases. Hence, an important variation of the mass input is seen when the lower aquifer thickness goes from 8 to 10 m compared to recent variation from 5 to 8m, and to old variation from 1 to 3m as shown in (Fig.7). The thickness of the lower aquifer and the amount of dissolved salt has proved to be inversely correlated, which is due to the velocity effect.

3.3. Faults geometry

It was expected that the thickness of the fault zones will have a similar influence on the salt dissolution, because the fault width influences both flow rate and velocity. The following simulations revealed a completely different effect for the different fault zones thicknesses. In fact, different values for the fault zones thicknesses were simulated, going from 0.5 m, to 40 m width (Table 3). The fault thickness could be related to flow velocity in the fault zones, where large faults induce small velocities (Fig. 8, Scenario S_Fault_7) and, thus, less dissolution compared to the other simulations (variable permeability, lower aquifer thickness, etc..). But if the fault zones get wider, a large amount of freshwater will invade the lower aquifer and the concentration of groundwater in the lower aquifer will be reduced. Hence, the concentration gradient between the salt layer and the water within the lower aquifer increases, and, therefore, the dissolution process with larger faults will increase (Figs. 9, 10). The results show (Fig. 10) that the mass input tends to reach a steady state when the fault reaches the 40m thickness, since the last variation of the mass input over the thickness variation from 25 to 40 m induces the smallest mass increase among the different scenarios. Unfortunately, numerical limitations prevented us from simulating values with fault thickness above 40m to find the fault thickness at which the steady state of mass input is reached. The limitations are mainly due to the lack of memory when increasing the fault thickness and maintaining the required mesh resolution in order to avoid numerical instability. The velocity difference between the fault zone at the WNW boundary and the drawdown of the pumping well induces turbulences within the faultzone which is basically due to the density contrast between the upper and the lower aquifers (Fig. 8).

In the previous sections the effect of the faults thicknesses on the dissolution process was demonstrated. With a 40 m thickness of fault, the dissolution rate has increased with about 125% with respect to the original model (10 m of thickness). Another factor that could affect the salt dissolution is the number of faults and their distribution. To study the impact of this factor on the salt dissolution, different scenarios of largest (40 m) fault were applied. Major faults causing significant displacement of sediments typically consist of sets of smaller faults, which can be grouped into a fault zone. Groundwater models often describe fault zones as homogeneous zone with increased hydraulic conductivity (e.g. Magri et al. 2011). In order to account for a more realistic approach of heterogeneity within the fault zone, the 40 m width is decomposed into 2, 3 and 6 faults with different combinations of fault widths (Table 6).

Despite that the actual active width of the fault is reduced when the faults number is increased, a substantial increase of mass input is observed when increasing the fault numbers (Figs. 11, 12). The dissolved mass increased by an amount of 13% when the wide (40 m) fault is replaced by six thin (2.5 m) faults (Fig. 12). This difference in mass input is due to the fact that steady state flow conditions require more time to be established in the case of six thin faults compared to the one single wide fault. To illustrate this difference, the time required for the lowest layer at the lower aquifer to reach the saturation concentration was investigated. Therefore, average concentrations for all the finite elements bordering the bottom of the lower aquifer were investigated for both cases (one large and six thin faults). Results show that 1.9 years are required in order to reach saturation within the lowest layer (*i.e.* no more dissolution) in the case of one wide fault, whereas up to 2.75 years in the case of six thin faults (Fig. 13). An important variation of the horizontal velocity component is observed in the lower aquifer in the case of 6 thin (2.5 m) faults (Fig. 14) compared to the 1 large (40 m) fault (Fig. 8). The average velocity over the lower aquifer is 3.8 m/day in the case of six thin faults compared to 2.5 m/day in the case of one large fault. The higher velocity in the lower aquifer extends the required time for steady state of flow to be established and therefore increases the amount of dissolved salt.

3.4. Effect of boundary conditions

The simulated varying subsurface parameters proved to have an important effect on salt dissolution. The observed variation reached up 125% (effect of fault thickness). Varying boundary conditions, however, are also influencing flow velocities and have therefore the potential to accelerate salt dissolution. Zechner et al. (2011) showed that the presence or absence of a pumping well did not have a significant effect on the subrosion process in a well-established karst. The authors did not test if the penetration depth of the pumping well would affect the dissolution, neither did they observe how the dissolution could be influenced by a variation of prescribed hydraulic heads at the recharging ESE boundary. In fact, increasing the hydraulic head at the inlet boundary will certainly increase the flow velocity above the fault zone at the ESE boundary. As a first approach, it could be expected that increasing the velocity above the ESE fault zone would create a pressure decrease in the area. Thus, the velocity within the lower aquifer could also be increased due to this decrease and, hence, potentially increase the dissolution process. The results, however, do not confirm any effect on dissolution due to varying hydraulic heads at the ESE boundary. Different values of the prescribed hydraulic boundary

heads were considered, going from 254 m to 300 m (Table 4). The effect of the simulated scenarios for the hydraulic head appears somehow oscillatory (Fig. 16). Hydraulic heads of up to 300m at the ESE boundary lead to a significant increase in horizontal velocity parallel to the x-axis of up to one magnitude in the upper aquifer. Its influence on both the horizontal velocity and the resulting dissolution in lower aquifer, however, is negligible (Fig. 17, Scenario S_Head_6). The difference between the minimum and the maximum values of the dissolved salt within the different scenarios is less than 1 % (Fig. 16). Therefore, the value of the hydraulic head could be considered as a negligible parameter on the dissolution process. The effect of the well depth, however, confirms the results of Zechner et al (2011). Different lengths of the wells were considered, going from 25m to 50 m (Table 5). As expected, the influence of the depth is also negligible on the amount of the dissolved salt (Fig. 18).

4. Conclusions

Observed subsidences in the study area of Northwestern Switzerland were mainly due to subsurface dissolution (subrosion) of evaporites (e.g. halite and gypsum). A set of 2D density driven flow simulations were evaluated along 1,000 m long and 150 m deep 2D cross sections within the study area. The simulations were conducted to study the effect of the different parameters that could affect the dissolution process.

Modeling density effects with high contrasts requires a coupled flow-transport numerical model for efficient computation due to the strong density-viscosity nonlinearity. A robust numerical code with advanced spatial and temporal approximations is used to reduce the excessive computational requirements and maintained the accuracy of the solution at the same time. Numerical difficulties at the presented field scale were encountered with the simulation of comparably thin structures such as fault thicknesses of less than 0.5 m and with lower aquifer thicknesses of less than 1 m.

A reduction of the thickness of the lower aquifer to 1 m increases the dissolution rate by more than 40%. Modeling the problem with a dynamic conductivity (varied relatively to the amount of dissolved salt), proved to have an important effect on the rate of dissolution: a 25% increase of the dissolution rate is observed when simulating the 2D model with a dynamic conductivity. Steady state of flow, however, is reached in both cases (with constant and dynamic conductivity) within 0.5 years. Among the studied parameters, two affecting the velocity field mostly in the upper aquifer had a negligible effect on the dissolution rate: varying the value of the hydraulic

head at the ESE boundary from 254 m to 300 m as well as increasing the penetration depth of the pumping well from 25 m to 50 m changed the amount of dissolved salt by less than 1%.

An increase of the dissolution rate up to 125% is observed when the thicknesses of the fault zones were increased to 40 m width. An additional concern is given to the most effective parameter, which is the structure of the normal fault zone. Therefore, a large (40 m) fault is replaced with two, three and six thin faults on both sides of the aquifer (WNW and ESE). A remarkable increasing in the dissolution is observed (13%) when going from one large fault to six thin faults. The reason why variation of normal fault zone structure leads to the highest variation of dissolution might be partly related to the field-specific setup. But the presence of conductive vertical zones in a variety of geological settings combined with the typical uncertainty related to the hydraulic characteristics of fractured fault zones suggests that faults play an important role in density-driven flow of groundwater and transport of solutes. These settings include also sites where seawater intrusion contaminates drinking water reservoirs, planned sites for disposal of radioactive waste, or sites for use of geothermal energy.

The presented study simulates the halite dissolution process with diffusion at the lower interface (Alkattan et al. 1997). More accurate results could possibly be obtained if the dissolution equation is implemented in the transport part within the numerical code. Moreover, the flow equation in the numerical code is based on the Darcy's equation to model the flow part. Within larger developing voids, fractures, or conduits, however, Darcy's equation is no longer valid. An implementation of Stokes equation for laminar free-flow media could provide more accurate solutions of the flow field and coupled dissolution process within the larger voids.

ACKNOWLEDGMENTS

This study was supported by the SNF (Swiss National Foundation), whose support is gratefully acknowledged.

References

Ackerer P, Younes A, 2008. Efficient approximations for the simulation of density driven flow in porous media. Adv Water Res 31(1):15–27

Alkattan M, Oelkers EH, Dandurand JL, Schott J, 1997. Experimental studies of halite dissolution kinetics: I. the effects of saturation state and the presence of trace metals. Chem Geol 137:201–220

Anderson RY, Kirkland DW, 1980. Dissolution of salt deposits by brine density flow. Geology 8:66–69

Clemens T, Hückinghaus D, Sauter M, Liedl R, Teutsch G ,1996. A combined continuum and discrete network reactive transport model for the simulation of karst development, IAHS Publ., 237, 309–318

Cooper AH , 2002. Halite karst geohazards (natural and man-made) in the United Kingdom. Environ Geol 42:505–512

Dreybrodt W , 1990. The role of dissolution kinetics in the development of karst aquifers in limestone: A model simulation of karst evolution, J. Geol., 98, 639– 655

GEODATA , 2010. Digital geological database for the city of Basel and northwestern Switzerland. Geological Survey Basel-Landschaft and Basel-Stadt, University of Basel, Switzerland

Groves CG, Howard AD, 1994a. Minimum hydrochemical conditions allowing limestone cave development, Water Resour. Res., 30, 607– 615

Groves CG., Howard AD, 1994b. Early development of karst systems, 1, Preferential flow path enlargement under laminar flow, Water Resour. Res., 30, 2837– 2846

Gutiérrez F, Desir G, Gutiérrez M, 2003. Causes of the catastrophic failure of an earth dam built on gypsiferous alluvium and dispersive clays (Altorricón, Huesca Province, NE Spain). Environ Geol 43:842–851

Gürler B, Hauber L, Schwander M, 1987. Die Geologie der Umgebung von Basel mit Hinweisen über die Nutzungsmöglichkeiten der Erdwärme [The geology of the Basel region including directions for the possibilities to use geothermal energy]. Beitrag zur Geologischen Karte der Schweiz. Stämpfli & Cie, Bern, Switzerland

Guerrero J., Gutie´rrez F, Lucha P, 2003. Paleosubsidence and active subsidence due to evaporite dissolution in the Zaragoza area (Huerva River valley, NE Spain): processes, spatial distribution and protection measures for transport routes. Engineering Geology 72 (2004) 309–329

Hauber L, 1971. Zur Geologie des Salzfeldes von Schweizerhalle-Zinggibrunn (Kt. Baselland)[On the geology of the salt mining field Schweizerhalle-Zinggibrunn (Canton Baselland)]. Eclogae geol Helv 64(1):163–183

Gureghian, A. B., 1975 .A study by the finite element method of the influence of fractures in confined aquifers, Soc. Pet. Eng. J., 15, 181 – 191.

Howard AD, Groves CG, 1995. Early development of karst systems, 2, Turbulent flow, Water Resour. Res., 31, 19–26

Huyakorn, P. S., B. H. Lester, and J. W. Mercer, 1983. Finite element techniques for modeling groundwater flow in fractured aquifers, Water Resour. Res., 19, 1019 – 1035.

James AN, Kirkpatrick IM, 1980. Design of foundations of dams containing soluble rocks and soils. Quart J Eng Geol Hydrogeol 13(3):189–198.

Johnson KS, 1981. Dissolution of salt on the east flank of the Permian Basin in the southwestern USA. J Hydrol 54:75–93

Johnson KS, 2005. Subsidence hazards due to evaporite dissolution in the United States. Environ Geol 48:395–409

Kaufmann G, Braun J, 1999. Karst aquifer evolution in fractured rocks, Water Resour. Res., 35, 3223–3238

Kaufmann G, Braun J, 2000. Karst aquifer evolution in fractured, porous rocks, Water Resour. Res., 36, 1381– 1392

Kaufmann G, 2002. Karst aquifer evolution in a changing water table environment. Water Resour Res,38, NO. 6, 1090, 10.1029/2001WR000256

Konz M, Ackerer P, Meier E, Huggenberger P, Zechner E, Gechter D, 2008. On the measurement of solute concentrations in 2-D flow tank experiments. Hydrol Earth Syst Sci 12:727–738

Konz M, Ackerer P, Younes A, Huggenberger P, Zechner E, 2009a. Two-dimensional stable-layered laboratory-scale experiments for testing density-coupled flow models. Water Resour Res 45: W02404. doi:10.1029/2008WR007118

Konz M, Younes A, Ackerer P, Fahs M, Huggenberger P, Zechner E, 2009b. Variable-density flow in heterogeneous porous media: laboratory experiments and numerical simulations. J Cont Hydrol 108:168–175. doi:10.1016/j.jconhyd.2009.07.005

Lucha P, Cardona F, Gutierrez F, Guerrero J, 2007. Natural and human-induced dissolution and subsidence processes in the salt outcrop of the Cardona Diapir (NE Spain). Environ Geol. doi:10.1007/s00254-007-0729-3.

Ludwig R, Schelkes K, Vogel P, Wollrath J, 2001. Implications of large-scale heterogeneities for hydraulic model studies at the potential site of a radioactive waste repository at Gorleben, Germany. Eng Geol,61(2-3):119–30.

Luo J, Dierch H-JG, Monninkhoff L.M.M, 2012. 3D Modeling of saline groundwater flow and transport in a flooded salt mine is Stassfurt, Germnay, Mine Water Environ 31:104-111, DOI 10.1007/s10230-012-0181-9.

Magri F, Akar T, Gemici U, Pekdeger A, 2011. Numerical investigations of fault-induced seawater circulation in the Seferihisar-Balcova Geothermal system, western Turkey, Hydrogeology journal DOI 10.1007/s10040-011-0797-z.

Martinez JD, Johnson KS, Neal JT, 1998. Sinkholes in evaporite rocks. Am Sci 86:38–51

OECD (ed), 1988. Hydrocoin Project. The International Hydrocoin Project, level 1: code verification. OECD, Paris

Oude Essink GHP, 2001a. Improving fresh groundwater supply-problems and solutions. Ocean Coastal Manage 44(5-6):429–49.

Oude Essink GHP, 2001b. Salt water intrusion in a three-dimensional groundwater system in The Netherlands: a numerical study. Transport Porous Med 2001;43:137–58.

Palmer A. N, 1991. Origin and morphology of limestone caves, Geol. Soc. Am.Bull., 103, 1– 21

Paniconi C, Khlaifi I, Lecca G, Giacomelli A, Tarhouni J, 2001. A modeling study of seawater intrusion in the korba coastal plain, Tunisia, Phys Chem Earth (B) 26(4):345–51.

Saladin M, 2004. Hydrogeologischer Zusammenhang von Tektonik und Grundwasserzirkulation im Gebiet Muttenz-Pratteln [Hydrogeologic relationship between tectonics and groundwater circulation in the Muttenz-Pratteln area]. Diplomarbeit, Universität Basel, Switzerland

Siemers J, Dreybrodt W, 1998. Early development of karst aquifers on percolation networks of fractures in limestone, Water Resour. Res., 34, 409– 419.

Spottke I, Zechner E, Huggenberger P, 2005. The southeast border of the Upper Rhine graben: a 3D structural model of geology and its importance for groundwater flow. Int J Earth Sci 94:580–593

Sroka A, Schober F, 1982. Die Berechnung der maximalen Bodenbewegungen über kavernenartigen Hohlräumen unter Berücksichtigung der Hohlraumgeometrie [Calculation of the maximum ground deformation considering the geometry of cavities]. Kali & Steinsalz, Berlin, pp 273–277

Wassmann TH, 1979. Mining subsidence in the East Netherlands. Proc Fifth Int Symp on Salt 1:463–475

Watson SJ, Barry DA, Scotting RJ, Hassanizadeh SM, 2002. Validation of classical density-dependent theory for stable, high-concentration gradient brine displacements in coarse and medium sand. Adv Water Resour 25:611–635

Xue Y, Xie C, Wu J, Lie P, Wang J, Jiang Q, 1995. A three-dimensional miscible transport model for seawater intrusion in China. Water Resour Res 31(4):903–12.

Younes A, Fahs M, Ahmed S, 2009. Solving density driven flow problems with efficient spatial discretizations and higher-order time integration methods. Adv Water Resour. doi:10.1016/j. advwatres.2008.11.003

Younes A, Konz M, Fahs M, Zidane A, Huggenberger P, 2011. Modelling variable density flow problems in heterogeneous porous media using the method of lines and advanced spatial discretization methods. Mathematics and Computers in Simulation (81) 2346–2355

Zechner E, Konz M, Younes A, Huggenberger P, 2011. Effects of tectonic structures, salt solution mining, and density-driven groundwater hydraulics on evaporite dissolution (Switzerland). Hydrogeology journal DOI 10.1007/s10040-011-0759-5.

Zidane A, Younes A, Huggenberger P, Zechner E, 2012. The Henry semi-analytical solution for saltwater intrusion with reduced dispersion, Water Resou Res, VOL. 48, W06533, doi:10.1029/2011WR011157.

List of Figures

List of tables

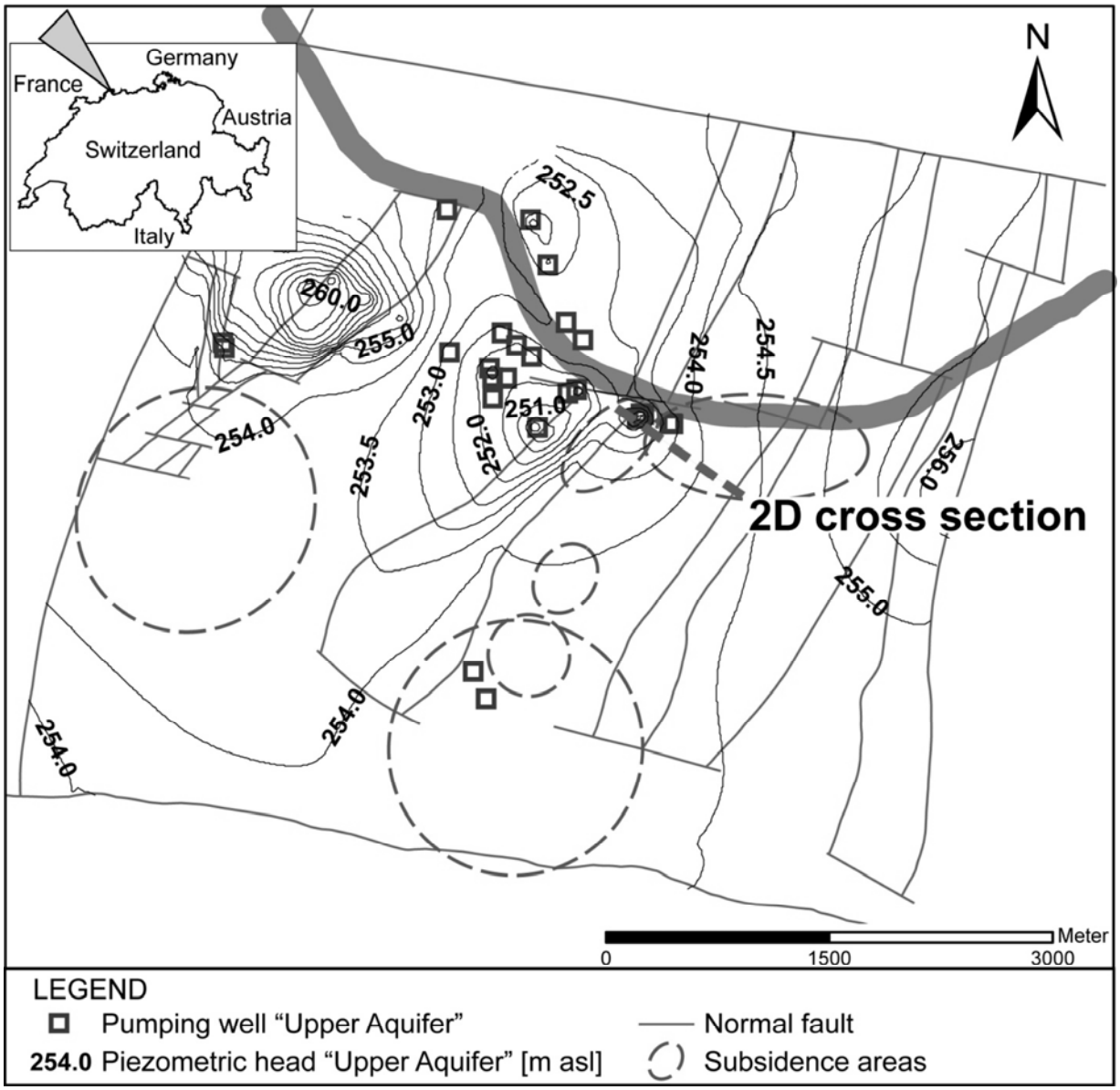

Fig. 1: Study area map in Northwestern Switzerland, showing: location of subsidence areas, normal faults, simulated piezometric head within the upper aquifer, and location of 2D cross section for density-coupled transport model (modified after Zechner et al 2011).

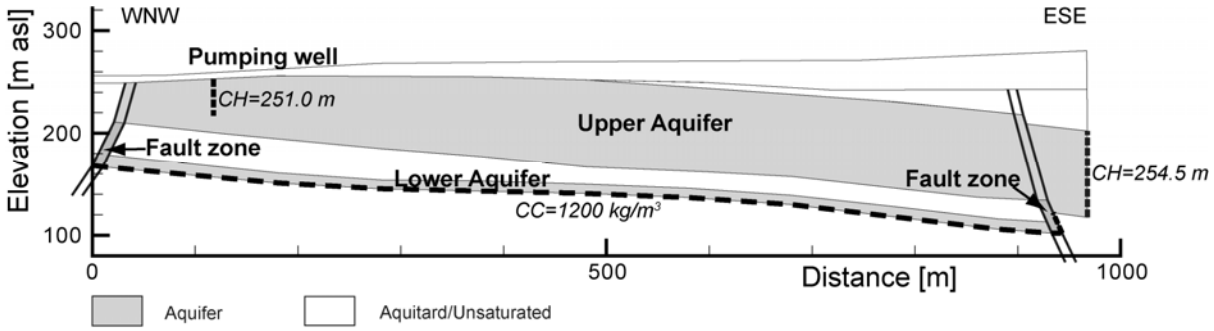

Fig. 2: 2D cross-section with hydrostratigraphic model for the simulation of density-coupled flow and transport. Used boundary conditions are "constant head" (CH; narrow dashed line) to simulate pumping at the well, inflow from the ESE, and outflow at the bottom towards the ESE. Boundary conditions of "constant concentration" (CC; wide dashed line) simulate solute flux into the bottom of the lower aquifer

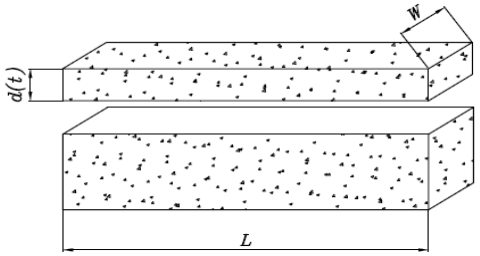

Fig. 3: Volume of the removed salt block

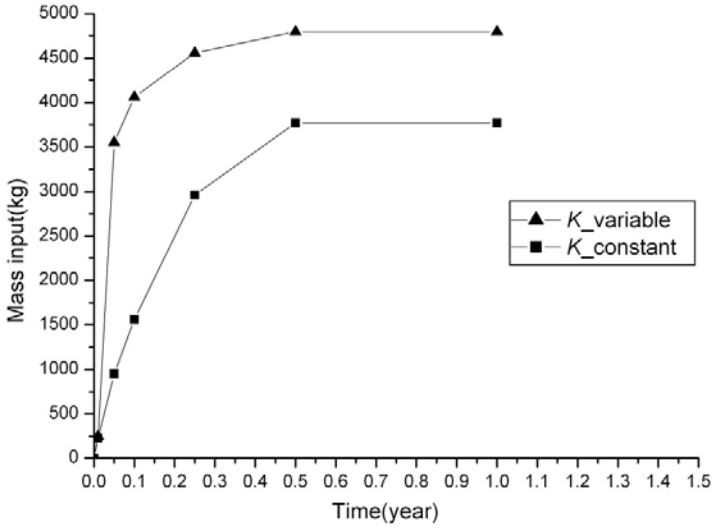

Fig. 4: Effect of variable conductivity on the amount of dissolved salt, K is the hydraulic conductivity

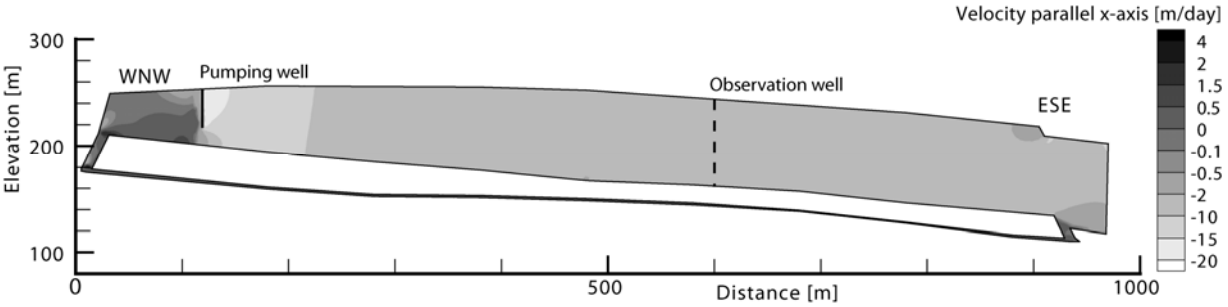

Fig. 5: Simulated x-component of velocity with 1m thickness of the lower aquifer after 30 years Scenario (S_Lower_1)

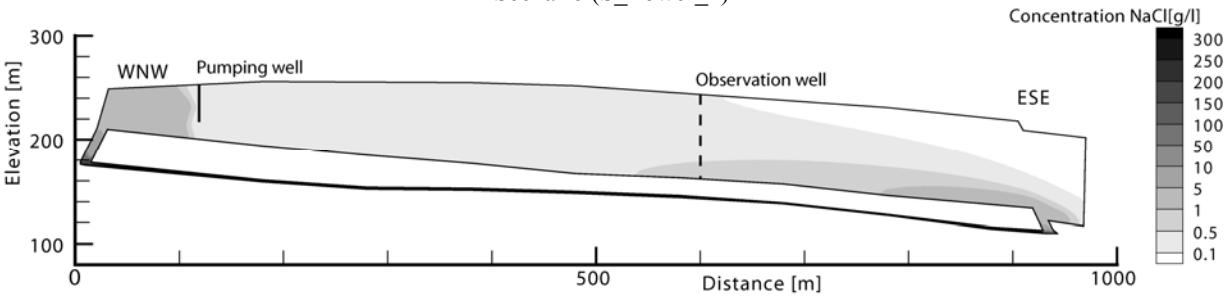

Fig. 6: Simulated NaCl Concentration with 1m thickness of the lower aquifer after 30 years Scenario (S_Lower_1)

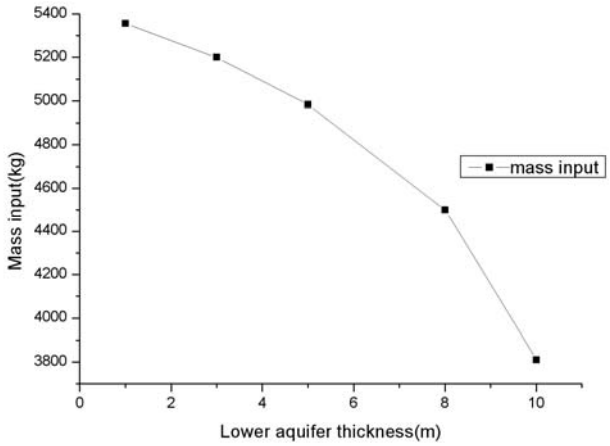

Fig. 7: Effect of lower aquifer thickness on the amount of dissolved salt (each point is a 30 years independent simulation).

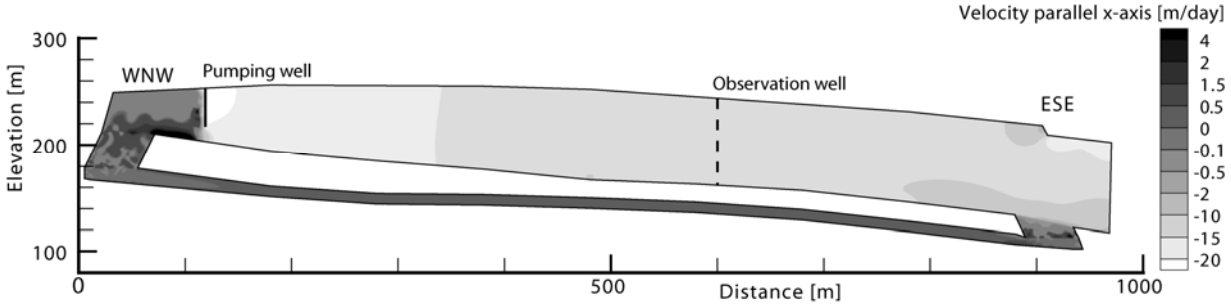

Fig. 8: Simulated x-component of velocity with 40m thickness of the fault zones after 30 years Scenario (S_Fault_7)

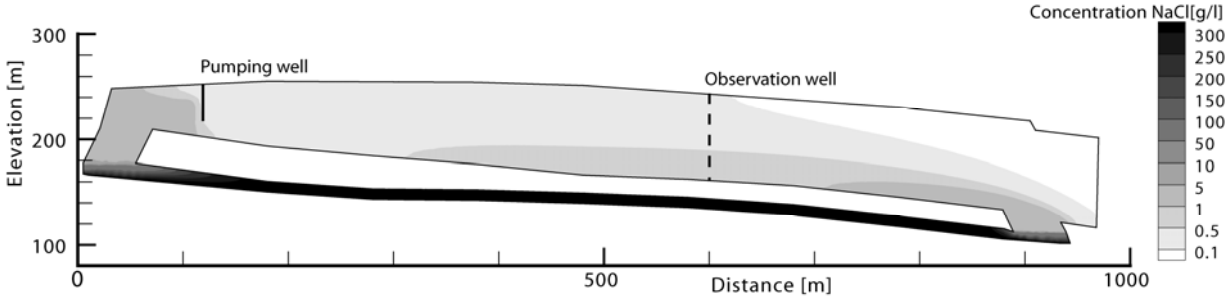

Fig. 9: Simulated NaCl Concentration with 40m thickness of the fault zones after 30 years Scenario (S_Fault_7)

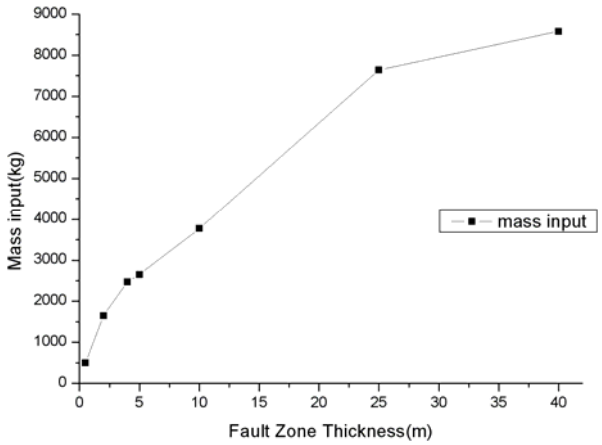

Fig. 10: Effect of fault zone thickness on the amount of dissolved salt (each point is a 30 years independent simulation).

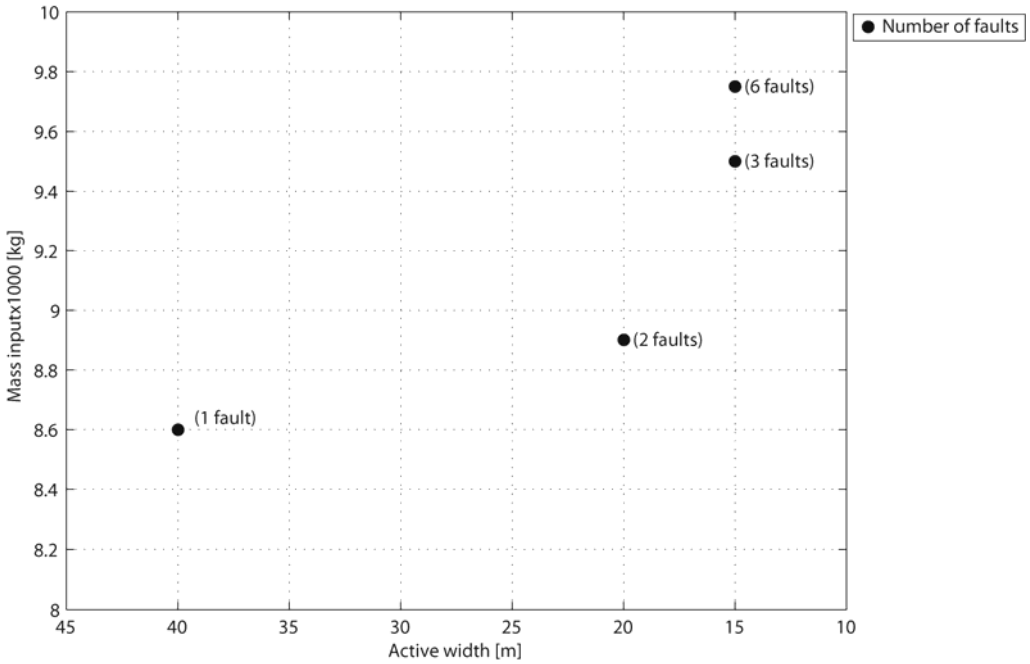

Fig. 11: Mass input with respect to the active width for the different fault number scenarios.

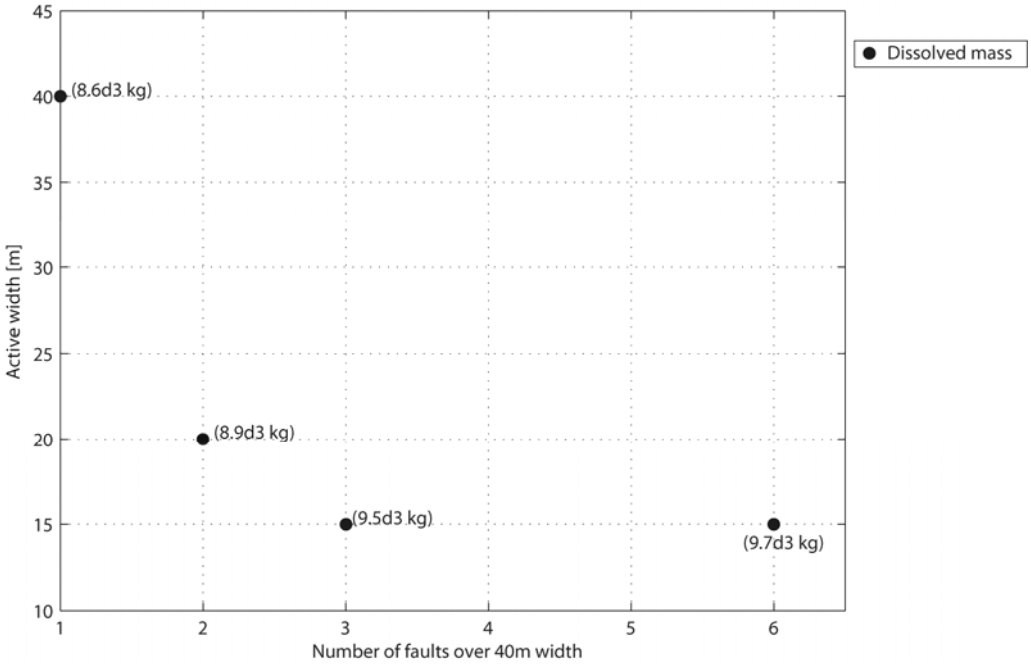

Fig. 12: Active width for the different fault number scenarios.

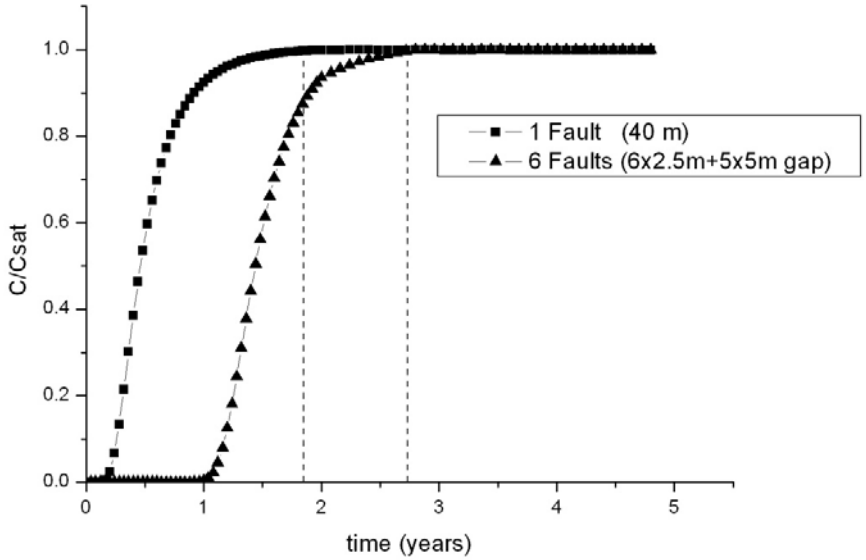

Fig. 13: Required time to reach the saturation in the lower aquifer.

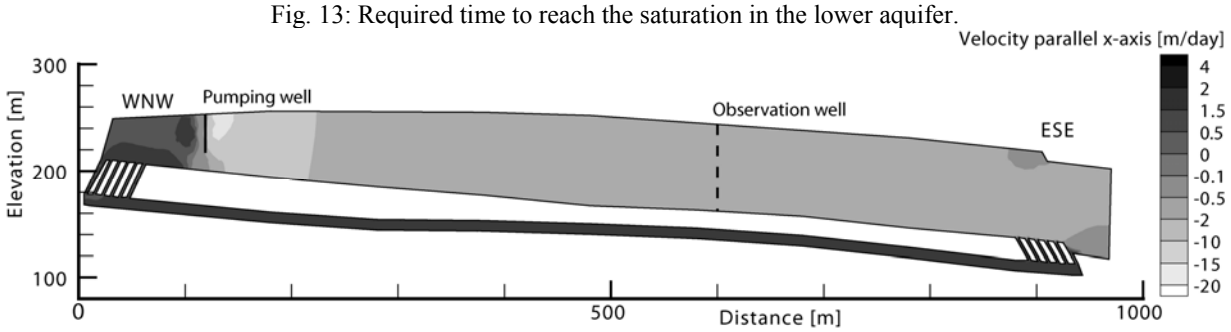

Fig. 14: Simulated x-component of velocity (with 6 thin faults) after 30 years.

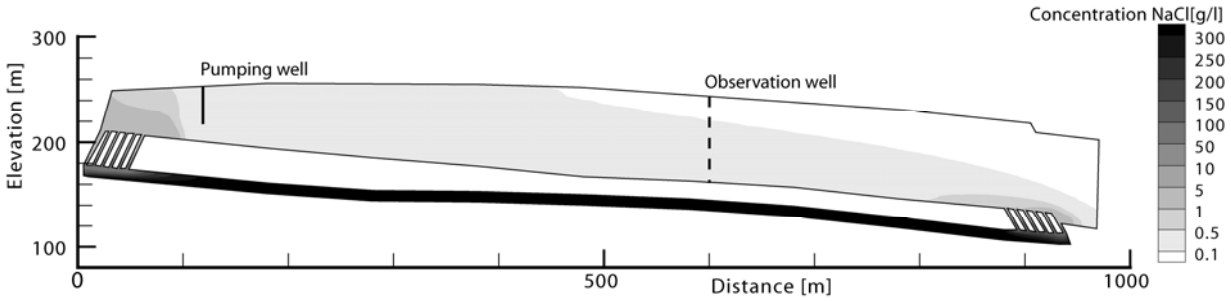

Fig. 15: Simulated NaCl Concentration (with 6 thin faults) after 30 years.

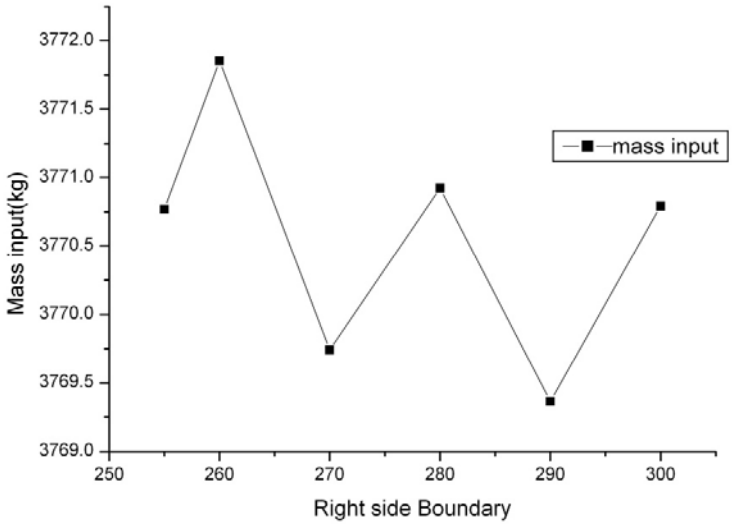

Fig. 16: Effect of the hydraulic head on the amount of dissolved salt (each point is a 30 years independent simulation).

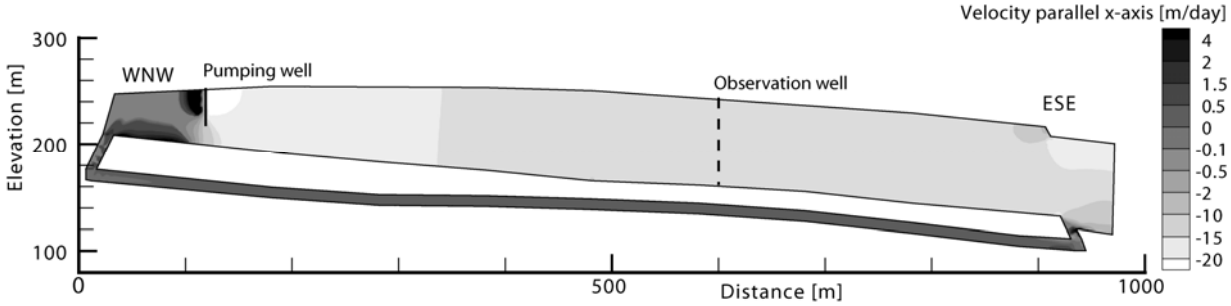

Fig. 17: Simulated x-component of velocity for the (300m) hydraulic head after 30 years Scenario (S_Head_6)

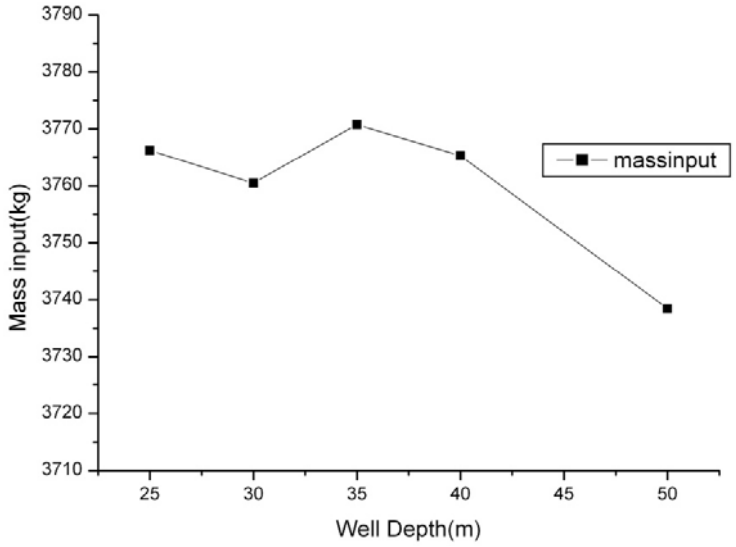

Fig. 18: Effect of the well depth on the amount of dissolved salt (each point is a 30 years independent simulation)

Scenarios / Parameters	S_*K*_1	S_*K*_2
K Upper Aq. [m/s]	7.4E-4	7.4E-4
ε Upper Aq. [-]	3%	3%
K Lower Aq.[m/s]	7.4E-4	Dynamic
ε Lower Aq. [-]	1%	Dynamic
K Fault zones[m/s]	7.4E-4	7.4E-4
ε Fault Zones [-]	1%	1%
Well depth [m]	25	25
Fault thickness[m]	10	10
Right side head[m]	254.5	254.5
Lower Aq. Slope[-]	6%	6%
Lower Aq. Thickness [m]	10	10

Table 1: Values of physical and geometrical parameters for the set of scenarios concerning the variation of the lower aquifer thicknesses. ε is the porosity and *K* is the hydraulic conductivity.

Scenarios / Parameters	S_Lower_1	S_Lower_2	S_Lower_3	S_Lower_4	S_Lower_5
K Upper Aq. [m/s]	7.4E-4	7.4E-4	7.4E-4	7.4E-4	7.4E-4
ε Upper Aq. [-]	3%	3%	3%	3%	3%
K Lower Aq.[m/s]	7.4E-4	7.4E-4	7.4E-4	7.4E-4	7.4E-4
ε Lower Aq. [-]	1%	1%	1%	1%	1%
K Fault zones[m/s]	7.4E-4	7.4E-4	7.4E-4	7.4E-4	7.4E-4
ε Fault Zones [-]	1%	1%	1%	1%	1%
Well depth [m]	25	25	25	25	25
Fault thickness[m]	10	10	10	10	10
Right side head[m]	254.5	254.5	254.5	254.5	254.5
Lower Aq. Slope[-]	6%	6%	6%	6%	6%
Lower Aq. Thickness [m]	1	3	5	8	10

Table 2: Values of physical and geometrical parameters for the set of scenarios concerning the variation of the lower aquifer thicknesses. ε is the porosity and *K* is the hydraulic conductivity.

Scenarios / Parameters	S_Fault_1	S_ Fault _2	S_ Fault _3	S_ Fault _4	S_ Fault _5	S_ Fault _6	S_ Fault _7
K Upper Aq. [m/s]	7.4E-4	7.4E-4	7.4E-4	7.4E-4	7.4E-4	7.4E-4	7.4E-4
ε Upper Aq. [-]	3%	3%	3%	3%	3%	3%	3%
K Lower Aq. [m/s]	7.4E-4	7.4E-4	7.4E-4	7.4E-4	7.4E-4	7.4E-4	7.4E-4
ε Lower Aq. [-]	1%	1%	1%	1%	1%	1%	1%
K Fault zones [m/s]	7.4E-4	7.4E-4	7.4E-4	7.4E-4	7.4E-4	7.4E-4	7.4E-4

ε Fault Zones [-]	1%	1%	1%	1%	1%	1%	1%
Well depth [m]	25	25	25	25	25	25	25
Fault thickness[m]	0.5	2	4	5	10	25	40
Right side head[m]	254.5	254.5	254.5	254.5	254.5	254.5	254.5
Lower Aq. Slope[-]	6%	6%	6%	6%	6%	6%	6%
Lower Aq. Thickness [m]	10	10	10	10	10	10	10

Table 3: Values of physical and geometrical parameters for the set of scenarios concerning the variation of the Fault zones thicknesses. ε is the porosity and *K* is the hydraulic conductivity.

Scenarios / Parameters	S_Head_1	S_Head_2	S_Head_3	S_Head_4	S_Head_5	S_Head_6
K Upper Aq. [m/s]	7.4E-4	7.4E-4	7.4E-4	7.4E-4	7.4E-4	7.4E-4
ε Upper Aq. [-]	3%	3%	3%	3%	3%	3%
K Lower Aq.[m/s]	7.4E-4	7.4E-4	7.4E-4	7.4E-4	7.4E-4	7.4E-4
ε Lower Aq. [-]	1%	1%	1%	1%	1%	1%
K Fault zones[m/s]	7.4E-4	7.4E-4	7.4E-4	7.4E-4	7.4E-4	7.4E-4
ε Fault Zones [-]	1%	1%	1%	1%	1%	1%
Well depth [m]	25	25	25	25	25	25
Fault thickness[m]	10	10	10	1	10	10
Right side head[m]	254.5	260	270	280	290	300
Lower Aq. Slope[-]	6%	6%	6%	6%	6%	6%
Lower Aq. Thickness [m]	10	10	10	10	10	10

Table 4: Values of physical and geometrical parameters for the set of scenarios concerning the variation of the right side hydraulic head. ε is the porosity and *K* is the hydraulic conductivity.

Scenarios / Parameters	S_well_1	S_well_2	S_well_3	S_well_4	S_well_5
K Upper Aq. [m/s]	7.4E-4	7.4E-4	7.4E-4	7.4E-4	7.4E-4
ε Upper Aq. [-]	3%	3%	3%	3%	3%
K Lower Aq.[m/s]	7.4E-4	7.4E-4	7.4E-4	7.4E-4	7.4E-4
ε Lower Aq. [-]	1%	1%	1%	1%	1%
K Fault zones[m/s]	7.4E-4	7.4E-4	7.4E-4	7.4E-4	7.4E-4
ε Fault Zones [-]	1%	1%	1%	1%	1%
Well depth [m]	25	30	35	40	50
Fault thickness[m]	10	10	10	10	10
Right side head[m]	254.5	254.5	254.5	254.5	254.5
Lower Aq. Slope[-]	6%	6%	6%	6%	6%
Lower Aq. Thickness [m]	10	10	10	10	10

Table 5: Values of physical and geometrical parameters for the set of scenarios concerning the variation of the well depth. ε is the porosity and *K* is the hydraulic conductivity.

Scenarios / Parameters	S_FN_1	S_FN_2	S_FN_3	S_FN_4
K Upper Aq. [m/s]	7.4E-4	7.4E-4	7.4E-4	7.4E-4
ε Upper Aq. [-]	3%	3%	3%	3%
K Lower Aq.[m/s]	7.4E-4	7.4E-4	7.4E-4	7.4E-4
ε Lower Aq. [-]	1%	1%	1%	1%
K Fault zones[m/s]	7.4E-4	7.4E-4	7.4E-4	7.4E-4
ε Fault Zones [-]	1%	1%	1%	1%
Well depth [m]	25	25	25	25
Overall Fault thickness[m]	40	40	40	40
Right side head[m]	254.5	254.5	254.5	254.5
Lower Aq. Slope[-]	6%	6%	6%	6%
Lower Aq. Thickness [m]	10	10	10	10
Faults number [-]	1	2	3	6
Active width [m]	40	2x10	3x5	6x2.5
Gap [m]	0	1x20	2x12.5	5x5

Table 6: Values of physical and geometrical parameters for the set of scenarios concerning the variation of faults number (FN). ε is the porosity and *K* is the hydraulic conductivity.

General conclusions and perspectives

The work presented in this thesis is divided into three main parts. Previous to the main parts, general mathematical and numerical methods that could be used to solve the flow and the transport problem in porous media and in free flow domains are introduced. Compared to different solution methods (FD, FV, FE, TH), and taking into account that the flow equations (Darcy and Stokes) should be coupled with density effects, the MFE method was used to solve the flow in porous media and the CR finite element method was used to solve the flow in free flow domains. Moreover, since the standards numerical methods (FV, FE) generate solution with numerical diffusion and/or non-physical oscillations, the DG-MPFA method was used to solve the advection-diffusion transport equation.

In the first part of this thesis, the developed MFE_DG_MPFA model was compared against a well-developed semi-analytical solution. The semi-analytical method was already developed by Henry [Henry 1964] in the saltwater intrusion problem. However, this solution can only simulate saltwater intrusion with unrealistic large amount of dispersion. The solution procedure developed by Henry is based on two steps: (i) an approximation of the solution by using a Fourier series representation with a certain truncation order of the coefficients and (ii) resolution of a strongly non-linear algebraic system to calculate these coefficients. This iterative technique is based on a sequential resolution of nonlinear systems of flow and mass transport. With this technique, convergence problems are encountered when decreasing the value of the molecular diffusion. To overcome these difficulties, a new procedure to calculate the semi-analytical solution was developed in this thesis. This procedure consists of solving simultaneously the flow and transport algebraic equations by using the Levenberg-Marquardt algorithm [Levenberg 1944, Marquardt 1963]. The use of this technique allowed developing, for the first time, semi-analytical solutions of saltwater intrusion in the case of small diffusion and in the case of a large density contrast.

A new semi-analytical solution was developed in the second part of this thesis. The semi-analytical solution for density driven free flows was developed by following the steps of Henry [Henry 1964], by using the Fourier-Galerkin method. Similar to the semi-analytical solution algorithm adopted for density driven flow in porous media, the Levenberg-Marquadt algorithm [Levenberg 1944, Marquardt 1963] was used to solve the nonlinear algebraic equations in free flow domains. In order to validate the CR_DG_MPFA numerical model, the latter was compared

against the developed semi-analytical solution in a synthetic saltwater intrusion problem through a fracture, where a good agreement was reproduced.

In the last part of this manuscript the focus was on the dissolution phenomenon. Within the framework of the project, the study of salt dissolution in fractures was recently studied by conducting a set of laboratory experiments for a salt block with cylindrical hole [Gechter et al. 2008]. As a continuation of this study, a numerical model was developed in this thesis to simulate the salt dissolution within fractures. To simulate the salt dissolution process, a dynamic mesh routine was also developed and coupled to the CR_DG_MPFA numerical model. This numerical model with dynamic mesh adaptation was used to simulate a simple dissolution experiment for a vertical fracture that has been recently conducted at Nancy University. The obtained numerical dissolution profiles were in good agreement with the experimental result.

Finally, the density driven flow code in porous media was used to run a set of numerical simulations on a 2D regional cross section from the Muttenz-Pratteln area. The aim of this study was to reveal the most important parameters that have an influence on the salt dissolution process that leads to the observed land subsidence within this area. The tectonic elements of faults were found to be the most important parameters that affect the salt dissolution. By varying the thickness and the repartition of faults the amount of the dissolved salt increased by more than one magnitude. The thickness and the permeability variation within the lower aquifer were found to have important effects on the salt dissolution. Effects of other parameters like the well depth and the hydraulic head at the boundary were found to be negligible.

Among the mentioned points, we could summarize the following conclusions:

- ✓ This deficiency encountered when solving the Henry problem was avoided by using the Levenberg-Marquardt algorithm to calculate the coefficients of the Fourier series. The adopted solution algorithm improve the applicability of the semianalytical solution of the Henry problem to saltwater intrusion problems with reduced diffusion and with high density contrast, and are therefore more suitable to benchmark density-driven flow codes.
- ✓ The new developed semi-analytical solution for density drive flow in a free flow media is considered as a useful tool to validate density driven Stokes flow codes.

- ✓ The developed procedure by combining the numerical resolution of density driven free flows with mesh adaptation is suitable to take into account evolution of fracture geometry due to dissolution.
- ✓ The geometry of the aquifer above the evaporite has a great influence on the subrosion process, especially the fault thickness values. An increase of the dissolution rate up to 125% is observed when the thicknesses of the normal fault zones were increased to 40 m width. A similar effect is observed when reducing the thickness of the aquifer to 1 m, which increases the dissolution rate by more than 40%.

In the framework of this thesis we could point out some ideas for further investigations:

- ✓ The results of this research thesis could be used as a basis for further experimental and conceptual model developments on salt dissolution and solute transport by density-driven groundwater flow. These may ultimately help provide predictions on land subsidence and other risks.
- ✓ The gained knowledge within this thesis could contribute to a 3D simulation of density flow with field data and geological structures. This could help to improve the knowledge on regional flow fields such as at the presented subsidence area in the region of Basel.
- ✓ The reliability of the developed numerical tools has been proven against semi-analytical and experimental results; therefore further numerical studies on field scale subrosion processes could be conducted.
- ✓ The studied dissolution case is of course an oversimplified representation of a natural system; but the developed code with mesh adaptation could be used as a starting point to study the dissolution phenomenon on real field applications, such as the development of karstic voids in evaporites coupled with flow and transport within these voids.

Bibliography

Aavatsmark, I (2002), An introduction to multipoint flux approximations for quadrilateral grids. *Computat. Geoscien.*, 6:404-432.

Aavatsmark I, Barkve T., Bøe Ø., Mannseth T. (1996), Discretization on non-orthogonal, quadrilateral grids for inhomogeneous, anisotropic media. *J Comput Phys*;127:2–14.

Abarca, E., J. Carrera, X. Sanchez-Vila and M. Dentz (2007), Anisotropic dispersive Henry problem, *Adv. Water Resour.*, 30(4),pp.913–926.

Ackerer, P, and A. Younes (2008) Efficient approximations for the simulation of density driven flow in porous media. *Adv Water Res*, 31:15-27.

Aegerter, I. & Bosshardt, A.G. (1999): Technischer Bericht, Setzungsproblematik-Massnahmen gegen Setzungen. Bericht im Auftrag der SBB, unpublished.

Aizinger, V., Dawson, C., Cockburn, B., Castillo, P.: The local discontinuous Galerkin method for contaminant transport. Adv Water Res;24:73-87,(2001).

Alkattan M, Oelkers EH, Dandurand JL, Schott J (1997), Experimental studies of halite dissolution kinetics: I. the effects of saturation state and the presence of trace metals. Chem Geol 137:201–220

Anderson RY, Kirkland DW (1980) Dissolution of salt deposits by brine density flow. Geology 8:66–69

Arbogast T. and Lehr H.L. (2006), Homogenization of a Darcy-Stokes system modeling vuggy porous media. *Comput. Geosci.*, 10:291.

Arnold D.N., On nonconforming linear-constant elements for some variants of the Stokes equations, presenta dal s.c. Franco Brezzi nella seduta del 24-6-93.

Arnold DN, Brezzi F, Cockburn B., Marini LD. (2002), Unified analysis of discontinuous Galerkin methods for elliptic problems. *SIAM J. Numer. Anal.*;5:1749-1779.

Baumann, C.E, Oden JT.: A discontinuous hp finite element method for convection–diffusion problems. Computat Meth Appl Mech Engrg;175:311–341,(1999).

Beavers G. and Joseph D. (1967), Boundary conditions at a naturally permeable wall, *J. Fluid Mech.*, 30:197.

Bear, J.: *Dynamics of Fluids in Porous Media* ~Elsevier, New York, (1972).

Brezzi F., Fortin M., Mixed and hybrid finite element methods, Berlin: Springer (1991).

Boffi D, Brezzi F, Fortin M, Finite Elements for the Stokes problem, *Lecture Notes in Mathematics* 1939, (2008), 45-100

Bruman E., Hansbo P. (2004), A stabilized nonconforming finite element method for incompressible flow, *Comput. Methods App0 Mech. Eng.*, vol. 195, num. 23-24, p. 2881-99.

Bruman E., Hansbo P. (2005), Stabilized Crouzeix-Raviart element for the Darcy-Stokes problem, *Numerical Methods for Partial Differential Equation,* 21(5), 986-997

Bues M., C. Oltean (2000), Numerical simulations for saltwater intrusion by the mixed hybrid finite element method and discontinuous finite element method. *Transport Porous Med* 2000;40(2):171–200

Cardenas M, Slottke D., Ketcham R, Sharp Jr. (2007), Navier-Stokes flow and transport simulations using real fractures shows heavy tailing due to eddies, Geophysical Research Letters, Vol.34, L14404, doi:10.1029/2007GL030545,

Chavent, G., Roberts J.E.: A unified physical presentation of mixed, mixed-hybrid finite elements and standard finite difference approximations for the determination of velocities in waterflow problems. Adv Water Res;14:329-348,(1991).

Clemens T, Hückinghaus D, Sauter M, Liedl R, Teutsch G (1996) A combined continuum and discrete network reactive transport model for the simulation of karst development, IAHS Publ., 237, 309–318

Conca C., Murat F., Pironneau O. (1994), The Stokes and Navier-Stokes equations with boundary conditions involving the pressure. *Jpn J. Math.* 20, 263-318

Conca C., Parés C., Pironneau O., Thiriet M. (1995), Navier-Stokes equations with imposed pressure and velocity fluxes. *Int. J. Numer. Methods Fluids* 20(4), 267-287

Cockburn B., Hou S., Shu CW. (1989), TVB Runge Kutta local projection discontinuous Galerkin finite element method for conservative laws III: One dimensional systems, *J. Compu.t Phys.*;84: 90-113.

Cockburn, B., Shu, CW. (1998): The Runge-Kutta Discontinuous Galerkin Method for conservative laws V: Multidimentional Systems. J Comput Phys;141:199-224.

Cockburn, B., Karniadakis, GE., Shu CW.(Eds.) (2000): Discontinuous Galerkin Methods: Theory, Computation and Applications. Lecture Notes in Computational Science and Engineering;11:Springer-Verlag.

Cooper AH (2002) Halite karst geohazards (natural and man-made) in the United Kingdom. Environ Geol 42:505–512

Crouzeix M., Raviart P. (1973), Conforming and nonconforming finite element methods for solving the stationary Stokes equations. *RAIRO Sér. Rouge*, 7(3), 33-75

Croucher, A.E., and M. J. O'Sullivan (1995), The Henry problem for saltwater intrusion, *Water Resour. Res*., 31(7), 1809 – 1814.

Dalrymple G.B (1991), The importance of small science, EOS transactions AGU, 72(1),pp 1,4.

Diersch H.J. (1988), Finite element modelling of recirculation density driven saltwater intrusion processes in groundwater, *Adv. Water Resour*., , 11, 25–43, doi:10.1016/0309-1708(88)90019-X.

Diersch H.J., Kolditz O. (1998), Coupled groundwater flow and transport: 2. Thermohaline and 3D convection systems, *Adv. Water Resour.*, , 21, 401–425, doi:10.1016/S0309-1708(97)00003-1.

Diersch, H.J. & Kolditz, O. (2002): Variable-density flow and transport in porous media: approaches and challenges. Adv. Water Res., 25, 899–944.

Dreybrodt W (1990) The role of dissolution kinetics in the development of karst aquifers in limestone: A model simulation of karst evolution, J. Geol., 98, 639– 655

Durlofsky, L.: Accuracy of mixed and control volume finite element approximations to Darcy velocity and related quantities. Water Resour Res.;30:965-973, (1994).

Durie, R.W. & Jessen, F.W. (1964): Mechanism of the dissolution of salt in the formation of underground cavities. Soc. Pet. Engn. J., 4, 2, 183-190.

Edwards, M.G., Rogers, C.F.: Finite volume discretization with imposed flux continuity for the general tensor pressure equation. Computat Geoscien,2:259-290, (1998).

Flekkøy E.G., Rage T., Oxaal U., and Feder J. (1996), Hydrodynamic Irreversibility in Creeping Flow, *Phys. Rev*, PACS numbers: 47.15.Gf, 02.70.Bf, 02.70.Lq, 47.60.+I, VOLUME 77, NUMBER 20

Forbes L.K. (1988), Surface waves of large amplitude beneath an elastic sheet. Part 2. Galerkin solution, J. Fluid Mechanics (188) 491-508.

Frind, E.O. (1982), Simulation of long-term transient density-dependent transport in groundwater, *Adv. Water Resour*., 5, 73 – 88.

Frumkin, A. (1994): Morphology and development of salt caves. NSS Bulletin, 56, 82- 95.

Frumkin, A. (1998): Salt cave cross-sections and their paleoenvironmental implications. Geomorphology, 23, 183-191.

Frumkin, A. (2000a): Dissolution of salt. In: Klimchouk, A. B., Ford, D. C., Palmer, A. N. & Dreybrodt, W. (eds): Speleogenesis – evolution of karst aquifers, 169-170. National Speleological Society, Huntsville.

Frumkin, A. (2000b): Speleogenesis in salt – the Mount Sedom area, Israel. In Klimchouk, A. B., Ford, D. C., Palmer, A. N., Dreybrodt, W. (eds): Speloegenesis – evolution of karst aquifers. National Speleological Society, Huntsville, 443-451.

Genuchten M.., (1991), Progress and opportunities o, hydrologic research, U.S. national report 1987-1990, Twentieth general assembly, International union of geodesy and geophysics, Vienna, Austria.

Gechter D, Huggenberger P., Ackerer, P and Waber H.N.,(2008), Genesis and shape of natural solution cavities within salt deposits Water Resou Res, VOL. 44, W11409, doi:10.1029/2007WR006753, 2008

GeoData (2010) Digital geological database for the city of Basel and northwestern Switzerland. Geological Survey Basel-Landschaft and Basel-Stadt, University of Basel, Switzerland

Girault V., Raviart PA., Finite element methods for Navier-Stokes equations, Berlin: Springer 1986

Gresho PM., Sani RL., Incompressible flow and the finite element method, New York: Wiley; 1998

Gresho PM, Sani R.L. (1987), On pressure boundary conditions for the incompressible Navier-Stokes equations. *Int. J. Numer. Methods Fluids* 7, 1111-1145

Groves CG, Howard AD (1994a) Minimum hydrochemical conditions allowing limestone cave development, Water Resour. Res., 30, 607– 615

Groves CG., Howard AD (1994b) Early development of karst systems, 1, Preferential flow path enlargement under laminar flow, Water Resour. Res., 30, 2837– 2846

Gutiérrez F, Desir G, Gutiérrez M (2003) Causes of the catastrophic failure of an earth dam built on gypsiferous alluvium and dispersive clays (Altorricón, Huesca Province, NE Spain). Environ Geol 43:842–851

Gürler B, Hauber L, Schwander M (1987) Die Geologie der Umgebung von Basel mit Hinweisen über die Nutzungsmöglichkeiten der Erdwärme [The geology of the Basel

region including directions for the possibilities to use geothermal energy]. Beitrag zur Geologischen Karte der Schweiz. Stämpfli & Cie, Bern, Switzerland

Guerrero J., Gutie´rrez F, Lucha P (2003) Paleosubsidence and active subsidence due to evaporite dissolution in the Zaragoza area (Huerva River valley, NE Spain): processes, spatial distribution and protection measures for transport routes. Engineering Geology 72 (2004) 309–329

Gureghian, A. B., A study by the finite element method of the influence of fractures in confined aquifers, Soc. Pet. Eng. J., 15, 181 – 191, 1975.

Goswami, R.R., and Clement, T.P., (2007), Laboratory-scale investigation of saltwater intrusion dynamics: *Water Resour. Res*., 43, W04418, doi:10.1029/2006WR005151.

Hansbo P., Larson MG (2003), Discontinuous Galerkin and the Crouzeix-Raviart element: application to elasticity. *ESAIM: Math. Model. Numer. Anal.* 37(1), 63-72

Hansbo P., Larson M.G. (2002), Discontinuous Galerkin methods for incompressible and nearly incompressible elasticity by Nitshe's method. *Comput. Methods Appl. Mech. Engrg*, 191(17-18), 1895-1908

Happel, J., and Brenner,H.,(1965), *Low Reynolds Number Hydrodynamics* (Prentice Hall Inc., Englewood Cliffs, NJ).

Hauber L (1971) Zur Geologie des Salzfeldes von Schweizerhalle-Zinggibrunn (Kt. Baselland)[On the geology of the salt mining field Schweizerhalle-Zinggibrunn (Canton Baselland)]. Eclogae geol Helv 64(1):163–183

Henry, H. R. (1964), Effects of dispersion on salt encroachment in coastal aquifers, in *Sea Water in Coastal Aquifers, U.S. Geol. Surv. Supply Pap.,* 1613-C, 70 – 84.

Herbert AW, Jackson CP, Lever DA. (1988), Coupled groundwater flow and solute transport with fluid density strongly dependent upon concentration. *Water Resour Res*; 24:1781–95.

Howard AD, Groves CG (1995) Early development of karst systems, 2, Turbulent flow, Water Resour. Res., 31, 19–26

Huber, R., Helmig, R. ,(1999): Multiphase flow in heterogeneous porous media: a classical finite element method versus an implicit pressure-explicit saturation-based mixed finite element-finite volume approach. Int J Numer Meth in Fluids;29:899-920.

Hughes, TJR., Masud, A., Wan, J. ,(2006): A stabilized mixed discontinuous Galerkin method for Darcy flow. Computat Meth Appl Mech Engrg;195(25-28):3347- 3381.

Huyakorn, P. S., P. F. Andersen, J. W. Mercer, and H. O. White Jr. (1987), Saltwater intrusion in aquifers: Development and testing of a three-dimensional finite element model, *Water Resour. Res.*, 23, 293 – 312.

Huyakorn, P. S., B. H. Lester, and J. W. Mercer, Finite element techniques for modeling groundwater flow in fractured aquifers, Water Resour. Res., 19, 1019 – 1035, 1983

Jäger W and Mikelić A. (2000), On the interface boundary condition of Beavers, Joseph, and Saffman. *SIAM J. Appl. Math.* 60:1111.

Jäger W. and Mikelić A. (2001a), Asymptotic analysis of the laminar viscous flow over a porous bed. *SIAM J. Sci. Comput.* 22:2006.

Jäger W. and Mikelić A. (2001b), On the roughness-induced effective boundary conditions for an incompressible viscous flow, *J. Differ. Equ*. 170, 96-122

James AN, Kirkpatrick IM (1980) Design of foundations of dams containing soluble rocks and soils. Quart J Eng Geol Hydrogeol 13(3):189–198

James, A. N. (1992): Soluble materials in civil engineering. Ellis Horwood, Chichester.

Johannsen, K., Kinzelbach, W., Oswald, S. & Wittum, G. (2002): The saltpool benchmark problem – numerical simulation of saltwater upconing in a porous medium. Adv. Water Res., 25, 335-348.

Johnson KS (1981) Dissolution of salt on the east flank of the Permian Basin in the southwestern USA. J Hydrol 54:75–93

Johnson, K.S. (1992): Evaporite karst in the Permian Blaine Formation and associated strata in Western Oklahoma, USA. Int. Contributions to Hydrogeology, 13, 405-420.

Johnson KS (2005) Subsidence hazards due to evaporite dissolution in the United States. Environ Geol 48:395–409

Kaufmann G, Braun J (1999) Karst aquifer evolution in fractured rocks, Water Resour. Res., 35, 3223–3238

Kaufmann G, Braun J (2000) Karst aquifer evolution in fractured, porous rocks, Water Resour. Res., 36, 1381– 1392

Kaufmann G (2002) Karst aquifer evolution in a changing water table environment. Water Resour Res,38, NO. 6, 1090, 10.1029/2001WR000256

Kaviany M. (1999), Principles of Heat Transfer in Porous Media, *Mechanical Engineering Series*, Springer-Verlag, New York.

Kavetski D., Binning P., Sloan S.W. (2001), Adaptive time stepping and error control in a mass conservative numerical solution of the mixed form of Richards equation, Adv. Water Resour., ,24(6), 595–605, doi:10.1016/S0309-1708(00)00076-2.

Kirby, R.,(2000): A Posteriori Error Estimates and Local Time-Stepping for Flow and Transport Problems in Porous Media, Ph.D thesis, University of Texas at Austin.

Klausen, R.A, Russell T.F.,(2004): Relationships among some locally conservative discretization methods which handle discontinuous coefficients. Journal Computat Geoscien,8(4):1-37.

Kolditz O, R. Ratke, H.-JG. Diersch, and W. Zielke (1998), Coupled groundwater flow and transport: 1. Verification of variable density flow and transport models, *Adv Water Res*. 21, 27–46.

Konz, M., Ackerer P., Younes A., Huggenberger P., Zechner E. (2009), Two-dimensional stable-layered laboratory-scale experiments for testing density-coupled flow models, *Water Resour. Res.*, 45: W02404, doi:10.1029/2008WR00711

Konz M, Ackerer P, Meier E, Huggenberger P, Zechner E, Gechter D (2008) On the measurement of solute concentrations in 2-D flow tank experiments. Hydrol Earth Syst Sci 12:727–738

Konz M, Younes A, Ackerer P, Fahs M, Huggenberger P, Zechner E(2009b) Variable-density flow in heterogeneous porous media: laboratory experiments and numerical simulations. J Cont Hydrol 108:168–175. doi:10.1016/j.jconhyd.2009.07.005

Kozary, M. T., Dunlap, J. C. and Humphrey, W. E.,(1968): Incidence of saline deposits in geologic time, *Geol. Soc. Am. Spec. Pap.*, *88*, 43−57.

Levenberg, K. (1944), A method for the solution of certain nonlinear problem in least squares, *Quart. Appl. Math.*, 2 , 164-168.

Langtangen H.P., Mardal K., Winther R. (2002), Numerical methods for incompressible viscous flow. *Adv. Water Res*. 25 1125-1146.

Landau L.D. and Lifshitz E.M., *Fluid Mechanics* (Pergamon Press, New York, 1987), 2nd ed.

Laubscher, H.P. (1982): Die Südostecke des Rheingrabens - ein kinematisches und dynamisches Problem. Eclogae geol. Helv., 75, 1, 101-116.

Lucha P, Cardona F, Gutierrez F, Guerrero J (2007) Natural and human-induced dissolution and subsidence processes in the salt outcrop of the Cardona Diapir (NE Spain). Environ Geol. doi:10.1007/s00254-007-0729-3

Ludwig R, Schelkes K, Vogel P, Wollrath J (2001) Implications of large-scale heterogeneities for hydraulic model studies at the potential site of a radioactive waste repository at Gorleben, Germany. Eng Geol,61(2-3):119–30.

Lukaszewicz G. (1997), On the Navier-Stokes equations in time dependent domains with boundary conditions involving the pressure. *J. Math. Sci*. Univ. Tokyo 4, 529-550

Li J., Chen Z. (2008), A new local stabilized nonconforming finite element method for the Stokes equations, *Computing*, 82:157-170, doi 10.1007/s00607-008-0001-z

Marquardt, D. W. (1963), An algorithm for least-squares estimation of nonlinear inequalities, SIAM *J. Appl. Math*., 11 , 431-441.

Martinez JD, Johnson KS, Neal JT (1998) Sinkholes in evaporite rocks. Am Sci 86:38–51

OECD (ed) (1988) Hydrocoin Project. The International Hydrocoin Project, level 1: code verification. OECD, Paris

Meissner, U. (1973), A mixed finite element model for use in potential flow problem. International Journal for Numerical Methods in Engineering, 6: 467-473.

McManus, K. M., Hanor, J. S.,(1993): Diagenetic evidence for massive evaporite dissolution, fluid flow, and mass transfer in the Louisiana Gulf Coast. Geology, 21, 727?730.

Mosé, R., Siegel, P., Ackerer, P.: Application of the mixed hybrid finite element approximation in a groundwater flow model: luxury or necessity? Water Resour Res; 30:3001-3012,(1994).

Oldenburg CM, Pruess K. (1995), Dispersive transport dynamics in a strongly coupled groundwater-brine flow system. *Water Resour Res* 1995;31:289–302.

Oltean, C., Buès, M.A.,(2001): Coupled groundwater flow and transport in porous media. A conservative or non-conservative form? Transport in Porous Media, 44 (2), 219-246.

Oude Essink GHP (2001a) Improving fresh groundwater supply-problems and solutions. Ocean Coastal Manage 44(5-6):429–49.

Oude Essink GHP (2001b) Salt water intrusion in a three-dimensional groundwater system in The Netherlands: a numerical study. Transport Porous Med 2001;43:137–58.

Oswald, S. & Kinzelbach, W. (2004): Three-dimensional physical benchmark experiments to test variable-density flow models. J. Hydrol. 290, 22–42.

Quinlan, J. F., Smith, R. A. and Johnson, K. S.,(1986): Gypsum karst and salt karst of the United States of America, Le Grotte d'Italia, 4(XIII), 73?92.

Palmer A. N (1991) Origin and morphology of limestone caves, Geol. Soc. Am.Bull., 103, 1–21

Paniconi C, Khlaifi I, Lecca G, Giacomelli A, Tarhouni J (2001) A modeling study of seawater intrusion in the korba coastal plain, Tunisia, Phys Chem Earth (B) 26(4):345–51.

Park, C. H., Aral, M. M. (2008), Saltwater Intrusion Hydrodynamics in a Tidal Aquifer, *Journal of Hydrologic Engineering*, Vol 9, pp. 863-872.

Pinder, G. F., and H. H. Cooper Jr. (1970), A numerical technique for calculating the transient position of the saltwater front, *Water Resour. Res*., 6(3), 875 – 882.

Remson, I., G. M. Hornberger, and F. J. Molz (1971). Numerical methods in subsurface hydrology. Wiley, New-York.

Raviart, P. A., and J. M. Thomas (1977), A mixed hybrid finite element method for the second order elliptic problem. Lectures Notes in Mathematics, 606: 292-315. Springer-Verlag, New York.

Reuter, F., Stoyan, D.,(1993): Sinkholes in carbonate, sulphate, and chloride karst regions: Principles and problems of engineering geological investigations and predictions, with comments for the destruction and mining industries, in Applied karst geology, edited by B. F. Beck, pp. 3?25, A. A. Balkema, Rotterdam, Brookfield,

Ritzel, A. (1911): Die Kristalltracht des Chlornatriums und ihrer Abhängigkeit vom Lösungsmittel. Z. Kristallogr., 49, 152-192.

Saaltink M.W, Carrera J, Olivella S. (2004), Mass balance errors when solving the convective form of the transport equation in transient flow problems, *Water Resour. Res*., , 40, W05107, doi:10.1029/2003WR002866.

Saffman P. (1971), On the boundary condition at the surface of a porous medium, *Studies Appl. Math*. 50:93.

Saladin M (2004) Hydrogeologischer Zusammenhang von Tektonik und Grundwasserzirkulation im Gebiet Muttenz-Pratteln [Hydrogeologic relationship between tectonics and groundwater circulation in the Muttenz-Pratteln area]. Diplomarbeit, Universität Basel, Switzerland

Shuangzhang T., Shahrouz A. (2005), A slope limiting procedure in Discontinuous Galerkin finite element method for gasdynamics applications. *Int. J Numer Analy Modell*;2:163-178.

Segol, G. (1994), *Classic Groundwater Simulations Proving and Improving Numerical Models*, Prentice-Hall, Old Tappan, N. J.

Segol, G., G. F. Pinder, and W. G. Gray (1975), A Galerkin-finite element technique for calculating the transient position of the saltwater front, *Water Resour. Res.*, 11(2), 343 – 347.

Siegel, P., R. Mose, P. Ackerer, and J. Jaffré (1997), Solution of the advection diffusion equation using a combination of discontinuous and mixed finite elements, Int. J. Numer. Methods In Fluids 24, 595–613.

Siemers J, Dreybrodt W (1998) Early development of karst aquifers on percolation networks of fractures in limestone, Water Resour. Res., 34, 409– 419

Simpson, M. J., and T. P. Clement (2003), Theoretical analysis of the worthiness of the Henry and Elder problems as benchmarks of density-dependent groundwater flow models, *Adv. Water Resour.*, 26, 17– 31.

Simpson, M. J., and T. P. Clement (2004), Improving the worthiness of the Henry problem as a benchmark for density-dependent groundwater flow models, *Water Resour. Res.*, 40, W01504, doi:10.1029/2003WR002199.

Sloan S.W, Abbo A.J (1999), Biot consolidation analysis with automatic time stepping and error control. Part 1: Theory and implementation, *Int. J. Numer. Anal. Methods Geomech.*, , 23, 467–492, doi:10.1002/(SICI) 1096-9853(199905)23:6<467::AID-NAG949>3.0.CO;2-R.

Spottke I, Zechner E, Huggenberger P (2005) The southeast border of the Upper Rhine graben: a 3D structural model of geology and its importance for groundwater flow. Int J Earth Sci 94:580–593

Sroka A, Schober F (1982) Die Berechnung der maximalen Bodenbewegungen über kavernenartigen Hohlräumen unter Berücksichtigung der Hohlraumgeometrie [Calculation of the maximum ground deformation considering the geometry of cavities]. Kali & Steinsalz, Berlin, pp 273–277

Thorenz, C., G. Kosakowski, O. Kolditz, and B. Berkowitz (2002), An experimental and numerical investigation of saltwater movement in coupled saturated–partially saturated systems, *Water Resour. Res.*, 38(6), 1069, doi:10.1029/2001WR000364.

Tocci M.D., Kelley C.T., Miller C.T. (1997), Accurate and economical solution of the pressure-head form of Richards' equation by the method of lines, Adv. Water Resour., ,20(1), 1–14, doi:10.1016/S0309-1708(96)00008-5

Trefzger, E. (1925): Die Tektonik des westl. Dinkelbergs und des nördl. Tafeljuras bei Basel. Ber. natf. Ges. Freiburg i.Br., 24, 1-63.

Trefzger, E. (1950): Die Steinsalzlagerstätte von Rheinfelden (Baden). Stratigraphie, Solung und Senkung. Jber.u.Mitt.oberrh.geol.Ver., N.F. 32.

Turek S. (1996), A comparative study of some time-stepping techniques for the incompressible Navier-Stokes equations: From fully implicit nonlinear schemes to semi-implicit projection methods, Int. J. Numer. Methods Fluids, , 22(10), 987–1011, doi:10.1002/(SICI)1097-0363 (19960530) 22:10<987::AID-FLD394>3.0.CO;2-7.

Voss, C. I., and W. R. Souza (1987), Variably density flow and solute transport simulation of regional aquifers containing a narrow freshwater-saltwater transition zone, *Water Resour. Res.*, 23(10), 1851–1866.

Wagner, C. (1949): The dissolution rate of sodium chloride with diffusion and natural convection as rate-determining factors. J. Phys. Colloid Chem., 53, 1030-1033.

Wang, J. F., and M. P. Anderson (1982). Introduction to groundwater modelling. Freeman, San Francisco

Wassmann TH (1979) Mining subsidence in the East Netherlands. Proc Fifth Int Symp on Salt 1:463–475

Watson SJ, Barry DA, Scotting RJ, Hassanizadeh SM (2002) Validation of classical density-dependent theory for stable, high-concentration gradient brine displacements in coarse and medium sand. Adv Water Resour 25:611–635

Wheeler MF, Yotov I.,(2006): A multipoint flux mixed finite element method. SIAM44;5:2082-2106.

Williams G.A., Miller C.T. (1999), An evaluation of temporally adaptive transformation approaches for solving Richards' equation, Adv. Water Resour., , 22(8), 831–840, doi:10.1016/S0309-1708(98)00048-7

Whitehead, A.N. (1889), "On the Motion of Viscous Incompressible Fluids: A method of Approximation", Quart. J. of Pure and Appl. Math., 23, pp. 78-93; "Second Approximation to Viscous Fluid Motion: A Sphere Moving Steadily in a Straight Line", Ibid., pp. 143-152.

Xue Y, Xie C, Wu J, Lie P, Wang J, Jiang Q (1995) A three-dimensional miscible transport model for seawater intrusion in China. Water Resour Res 31(4):903–12.

Yamashita, N., and M. Fukushima (2001), On the rate of convergence of the Levenberg-Marquardt method. Computing 15, 239-249.

Younes, A., P. Ackerer, and F. Lehmann (2006), A new mass lumping scheme for the mixed hybrid finite element method, International Journal for Numerical Methods in Engineering, 67: 89–107.

Younes A, P. Ackerer (2008), Solving the advection-dispersion equation with Discontinuous Galerkin and Multipoint Flux Approximation methods on unstructured meshes. Int. J Numer Methods in Fluids, 58 (6), 687-708.

Younes, A., V. Fontaine (2008a), Hybrid and Multi Point Formulations of the Lowest Order Mixed Methods for Darcy's Flow on Triangles, *Int J Numer Meth in Fluids*, 58 1041-1062.

Younes A., V. Fontaine (2008b), Efficiency of Mixed Hybrid Finite Element and Multi Point Flux Approximation methods on quadrangular grids and highly anisotropic media. *Int. J. Numer. Meth. in Eng.*, 76, 3, pp 314-336.

Younes, A., M. Fahs, and S. Ahmed (2009), Solving density flow problems with efficient spatial discretizations and higher-order time integration methods, *Advances in Water Resources,* 32, 340-352.

Younes A., P. Ackerer, and F. Delay (2010), Mixed finite element for solving diffusion-type equations. Rev. *Geophys*., 48, RG1004, doi:10.1029/2008RG000277

Younes A. and Ackerer P. (2010), Empirical versus time stepping with embedded error control for density-driven flow in porous media, *Water Resour. Res*., 46, W01504, doi:10.1029/2009WR008229

Younes A., Fahs M., Ackerer P. *(*2010b), An efficient geometric approach to solve the slope limiting problem with the Discontinuous Galerkin method on unstructured triangles, *Int. J. Numer. Meth. Biomed. Engng.*; **26**:1824–1835.

Younes A, Konz M, Fahs M, Zidane A, Huggenberger P (2011) Modelling variable density flow problems in heterogeneous porous media using the method of lines and advanced spatial discretization methods. Mathematics and Computers in Simulation (81) 2346–2355

Younes, A., Ackerer, P., Chavent, G.: From mixed finite elements to finite volumes for elliptic PDEs in two and three dimensions. Int J Numer Meth in Engin.; 59: 365-388,(2004).

Zechner E., Konz M., Younes A., Huggenberger P. (2011) Effects of tectonic structures, salt solution mining, and density-driven groundwater hydraulics on evaporite dissolution. *Hydrogeology Journal*, pp. 1-12. doi:10.1007/s10040-011-0759-5

Zidane, A., Younes, A., Huggenberger, P., Zechner, E.,(2012): The Henry semi-analytical solution for saltater intrusion with reduced dispersion, Water Resou Res, VOL. 48, W06533, doi:10.1029/2011WR011157.